The Role of Baroclinic Processes in a Tropical Cyclone Motion

by
Maria Flatau

Department of Atmospheric Science
Colorado State University
Fort Collins, Colorado

Colorado State University

Department of Atmospheric Science

Paper No. 488

THE ROLE OF BAROCLINIC PROCESSES IN A TROPICAL CYCLONE MOTION

by
Maria Flatau

Department of Atmospheric Science
Colorado State University
Fort Collins, CO 80523

January 3 , 1992

Atmospheric Science Paper No 488

ABSTRACT

The numerical study presented here has focused on baroclinic processes which contribute to tropical cyclone propagation. Two numerical models were used in this work. A linear one-layer shallow water model was used to analyze the development of instabilities in the hurricane outflow layer. A three-dimensional, semi-spectral, primitive equation model of baroclinic vortex was developed to study TC motion. We have investigated how vortex motion is affected by (1) the interaction between upper and lower potential vorticity anomalies in a tilted vortex, (2) asymmetric distribution of diabatic heating, and (3) the presence of dynamic instabilities in the cyclone outflow layer.

When a vortex is tilted, interaction between upper and lower level vorticity anomalies leads to vortex propagation relative to the steering flow. On a β-plane, with no environmental flow, the vortex is slightly tilted toward the south and the interaction between the layers reduces the westward movement of the vortex. The vortex tilting can also occur due to the vertical shear in the environmental wind. On an f-plane, the interaction between the layers causes the northward movement of the vortex in westerly linear shear, and southward movement in easterly linear shear, with a meridional velocity of about 1 m/s. This velocity increases with increasing vortex intensity and vertical motion. The magnitude of the meridional vortex velocity caused by this effect is comparable with the motion resulting from advection of planetary vorticity.

The response of baroclinic vortex motion to asymmetric heat sources show that asymmetries placed at larger radii create potential vorticity anomalies similar to "beta gyres" . Circulation associated with these anomalies advects the vortex. Diabatic heating anomalies located in the southern and southeastern part of a vortex significantly reduce the motion due to the β effect.

The results of a shallow water, linear model show that dynamically unstable modes can develop in the cyclone outflow layer even in the absence of environmental forcing. Development of both barotropic and inertial instability is possible. In a three-dimensional model, vortices with different intensities respond differently to identical environmental forcing. In strong vortices, slow looping motion with period of few days can be observed. Since the period of this slow oscillation corresponds to the frequency of barotropically unstable modes, we attribute this type of motion to development of barotropic intstability in the outflow layer of a baroclinic vortex.

ACKNOWLEDGEMENTS

I would like to thank my advisors Drs. Wayne Schubert and Duane Stevens for their advice and encouragement throughout this work. I would also like to thank my commitee members Drs. William Gray and Gerald Taylor for their helpful advice. Many experiments in this work were inspired by discussions with Dr. Gray and the members of his research group. I have also benefited from discussions with my colleagues from Dr Stevens and Dr. Schubert projects.

I am grateful to Paul Ciesielski, Christopher Landsea and Annette Claycomb for reading and commenting on the drafts of this paper. I am grateful to Dr. D. Pfenniger for providing a computer program for fitting a circle to the data points used in calculation of the vortex center. I appreciate the help of Judy Sorbie who drafted many of figures in this paper and Gail Cordova who help me in preparation of the manuscript.

Finally, I am deeply indebted to my husband Piotr Flatau. His ardent belief in women's right to professional careers and his constant support in professional as well as domestic matters kept me going during the course of this work.

This work was sponsored by NSF under grants ATM8352205 and ATM8609731 and by the Office of Naval Research under grant N000014-K-0214. The computing support wasd provided by the National Center for Atmospheric Research,

TABLE OF CONTENTS

Chapter 1

INTRODUCTION

The motion of tropical cyclones (TC) is usually described in terms of "steering" and "propagation" . This conceptual model reflects the fact that barotropic vorticity advection is the primary mechanism responsible for tropical storm motion. The idea of steering is in principle quite simple. If one assumes that a tropical cyclone is represented by a symmetric barotropic vortex and the environmental flow is horizontally and vertically uniform, then the motion of the vortex is completely determined by the speed and direction of the environmental flow referred to as the steering current (DeMaria, 1987). Even though neither assumption is satisfied in real tropical cyclones, the motion of a cyclone to a large extent can be explained by steering. The difference between the observed storm motion and the steering flow is called propagation.

In practice, it is difficult to precisely define the steering current. Environmental flows are never uniform, cyclones are not symmetric and, in addition, they interact with each other, such that it is very difficult to distinguish between the environmental flow and the cyclone circulation. The usual procedure is to represent an environmental flow by an azimuthal and vertical average. Composite cyclones are used to establish what radial belts and vertical levels should be used in averaging. Gray (1991) shows that the motion of tropical storms agrees best with the vertically averaged flow very close ($1^o - 3^o$ radial belt) to the storm interior (Fig. 1.1). However, it is impossible to determine the flow at such close radii for a single tropical storm. The most common definition of a steering flow includes the $5^o - 7^o$ radial belt averages, where a sufficient number of observations exist to determine the flow.

Another question which needs to be addressed is what vertical levels or vertical averages give the best agreement between predicted and observed motion. This subject

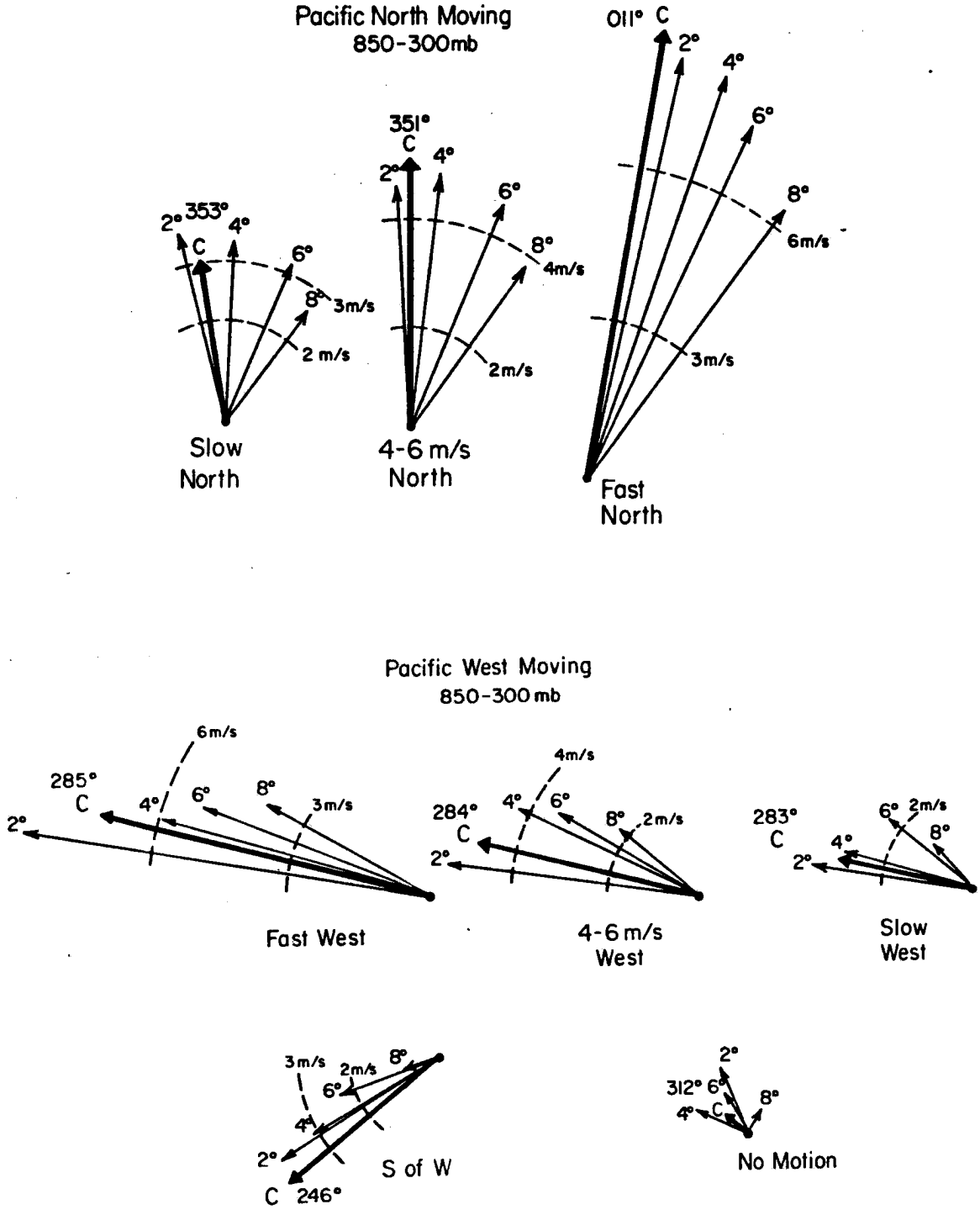

Figure 1.1: Layer average (300mb-850mb) wind vectors, azimuthally averaged over different radial belts relative to the mean cyclone motion, for west-moving and north-moving Pacific storms (From Gray, 1989)

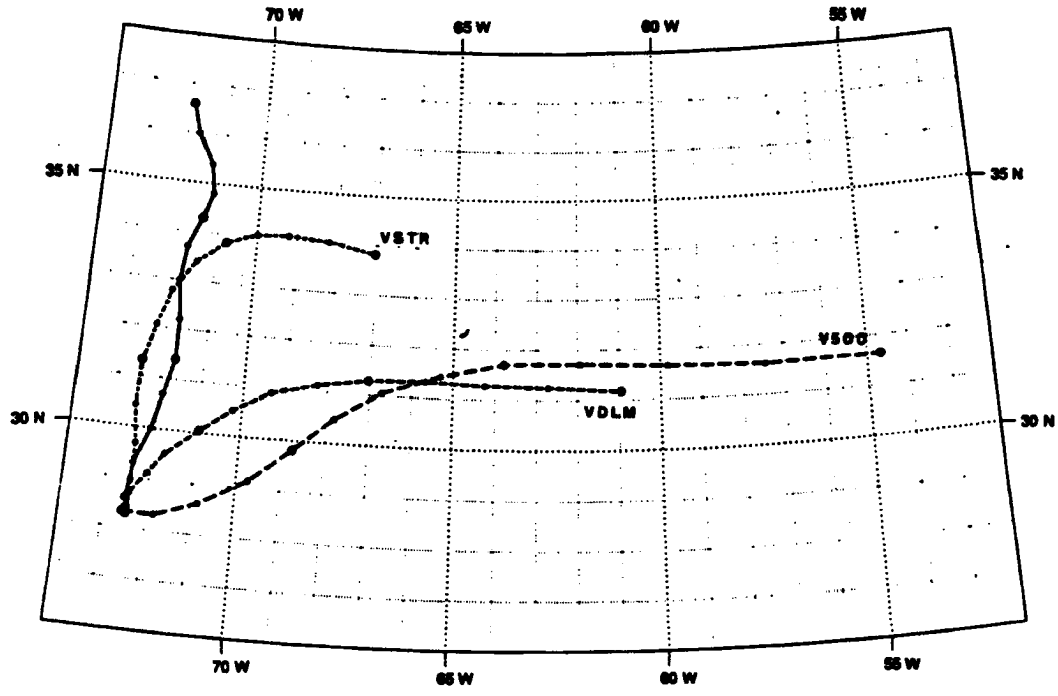

Figure 1.2: Josephine's best track (solid) and VICBAR forecast track run with the deep layer mean flow (VDLM), the 500 mb flow (V500) and the flow at the level which agrees best with the previous track (VSTR). From Franklin, 1990.

has been the focus of many studies in which the relationship between environmental flow features and tropical cyclone motion are analysed (Chan and Gray, 1982; Dong and Neumann, 1986; Franklin, 1990). It is generally agreed that the mid-tropospheric flow (500, 600 or 700mb) or the deep tropospheric average is the best indicator of cyclone movement (Chan and Gray, 1982). However, when we consider a single cyclone which moves in an environment with strong vertical wind shear, the deep layer average wind does not necessarily produce a good motion forecast. For such cases, the choice of the steering level is critical, and using the level which agrees best with past storm motion usually works best (Fig. 1.2). The presence of vertical wind shear also makes the forecast of recurving cyclones quite difficult. As shown by Hodanish (1991), the best indicator of the future motion of these cyclones is the upper and mid-tropospheric flow, not the vertically averaged current.

Propagation, unlike steering, is the result of many different processes. Identifying these processes is an important aspect of tropical cyclone motion studies in which examining observational data and the results of analytical and numerical models play an equally significant role. Observations provide information on the typical values of cyclone propagation depending on synoptic situation, speed and direction of motion and properties of the cyclone circulation (Chan and Gray, 1982; Dong and Neumann, 1986; Chan, 1985; Gray, 1991; Holland, 1983; Holland, 1984).

Understanding of the role different processes play in cyclone motion can be gained from analytical and numerical models. The barotropic processes governing the motion of tropical cyclones are fairly well known. Numerous studies have examined the role of planetary vorticity advection (Adem, 1956; Holland, 1983; Fiorino and Elsberry, 1989a) and environmental wind shear or vorticity gradients (Smith, 1991; DeMaria, 1987; Evans et al., 1991; Smith et al., 1990; Ulrich and Smith, 1991). Unlike motion due to steering, propagation results from interaction between the vortex and environment, and depends on properties of the vortex such as its strength (especially the magnitude of the outer winds), size and total angular momentum (Willoughby, 1988; Shapiro and Ooyama, 1990; Fiorino and Elsberry, 1989b).

The influence of the vertical structure of a cyclone and its environment on cyclone motion has received less attention. Earlier, three-dimensional models (Kitade, 1980; Madala and Piacsek, 1975) supported the results of barotropic models and concluded that baroclinic vortices on the β-plane move toward the northwest. Other 3D models examined the role of development of vortex asymmetries in the absence of environmental flow (Anthes, 1972; Abe, 1987). Only recently has interest in the influence of baroclinic processes on cyclone motion begun to grow. Shapiro (1991) pointed out the impact of potential vorticity (not just absolute vorticity) on cyclone propagation. He has shown that even in the absence of absolute vorticity gradients, cyclones can propagate in the direction perpendicular to the zonal steering current if the temperature gradient associated with the vertical shear causes the potential vorticity to change in the meridional direction. Wu and Emanuel (1991) examined the vertical interaction between potential vorticity anomalies in a quasi-geostrophic model and their influence on vortex movement. Gray (1991)

suggested that the fact that most tropical cyclones move faster than the $5^o - 7^o$ steering current results not from cyclone-environment interaction but from baroclinic properties of the environment itself. According to Gray (1991), these properties are largely independent of the cyclone circulation.

Tropical cyclones have been simulated with sophisticated three dimensional models with parameterizations of physical processes. However, the results of such models are almost as difficult to interpret as observations of real cyclones. The studies involving these models usually concentrate on the model's ability to simulate and forecast real tropical cyclone case studies (e.g., Kurihara et al., 1990).

The goal of the numerical study presented here is to understand baroclinic, dynamical mechanisms governing the motion of tropical cyclones. First, we examine the interaction between the upper and lower layers of a cyclone. Even though in barotropic studies the cyclone can be represented by a cyclonic vortex, in reality an anticyclonic potential vorticity anomaly surmounts the low-level cyclonic anomaly. When the axis of a vortex is strictly vertical, the vertical transport of momentum does not lead to flow asymmetries and the vortex moves with the environmental flow. If, however, the centers of the low-level cyclone and upper level anticyclone are displaced relative to each other, asymmetries in the flow develop and the vortex propagates in a direction perpendicular to the steering flow. The interaction between upper and lower vortex layers and its influence on cylone motion is discussed in Chapter 3.

In Chapter 4 we analyze the impact of convective heating asymmetries on cyclone propagation. Although symmetric convection is favorable for tropical storm development, satellite pictures of hurricanes often reveal asymmetric convection patterns, and a connection between convective asymmetry and the direction of cyclone motion has been observed (Lajoie, 1976; Fett and Brand, 1975). Even though it is possible to build a prediction scheme for short-term hurricane motion based on satellite pictures of cyclone convection, the correlation between TC motion and the convection distribution does not explain the role that the convective heating distribution plays in motion change. The change in the direction of storm motion can result from heating as well as dynamical effects, which only

manifest themselves as changes in cloudiness. In Chapter 5 we examine the vortex motion changes due solely to the distribution of diabatic heating and find that they can be quite significant.

In Chapters 5 and 6 we examine the dynamic processes in a tropical cyclone outflow layer. The anticyclonic outflow layer of a tropical storm is much more dynamically "active" than the lower, inertially stable layers. The low stability in this layer permits environmental influences to reach the cyclone center and affect cyclone development. In addition, even in the absence of environmental forcing, barotropic and inertial instabilities can develop. In Chapter 5, using an eigenvalue analysis, we establish the characteristics of barotropically and inertially unstable modes which develop in a circular flow with mean wind typical of a hurricane outflow layer. In Chapter 6 we examine the development of instabilities in a three-dimensional flow. We study the interaction of upper-layer instabilities with the low-level flow and their influence in vortex motion.

Two numerical models are used in this work. A linear, one-layer, shallow water model is used to analyze the development of instabilities in the hurricane outflow layer. This model, written by D. Stevens, is based on the Stevens and Ciesielski (1986) linear wave model and is described in Chapter 5.

The second model described in Chapter 2 is a three-dimensional, primitive equation model of a baroclinic vortex which was developed to study vortex motion. The equations are formulated on a β-plane in cylindrical coordinates. The σ coordinate is used in the vertical direction. The model is semi-spectral with a Fourier representation in the azimuthal direction. Such a representation allows us to limit the number of tangential modes necessary to describe the three-dimensional features of a moving vortex. The model equations do not include moist processes explicitly and the secondary circulation is forced by a specified diabatic heat source. The model was designed to bridge the gap between full, three dimensional hurricane models with parameterization of all physical processes and simple barotropic models of vortex motion. The model is sophisticated enough to represent the baroclinic aspects of a vortex motion, yet the simple parametrizations of physical processes make the sensitivity studies more strightforward and easier to interpret.

Chapter 2

THREE-DIMENSIONAL MODEL OF A MOVING VORTEX

2.1 Governing equations

The baroclinic vortex model uses the nonlinear, primitive equations formulated with cylindrical coordinates in the horizontal and the σ coordinate in the vertical. The vertical coordinate σ is defined as $\sigma = p/p_s$ where p_s is the surface pressure[1]. In the coordinates (r, λ, σ), the governing equations have the following form:

Pressure tendency equation:

$$\frac{\partial}{\partial t}(p_s r) = -\int_0^1 \frac{\partial}{\partial r}(p_s r u)\, d\sigma - \int_0^1 \frac{\partial}{\partial \lambda}(p_s v)\, d\sigma \tag{2.1}$$

Vertical velocity equation:

$$p_s r \dot{\sigma} = -\left(\sigma \frac{\partial}{\partial t}(p_s r) + \int_0^\sigma \frac{\partial}{\partial r}(p_s r u)\, d\sigma + \int_0^\sigma \frac{\partial}{\partial \lambda}(p_s v)\, d\sigma\right) \tag{2.2}$$

Hydrostatic equation:

$$\frac{\partial \Phi}{\partial \sigma} = -\frac{RT}{\sigma} \tag{2.3}$$

Radial momentum equation:

$$\begin{aligned} \frac{\partial}{\partial t}(p_s r u) = & - \frac{\partial}{\partial r}(p_s r u u) - \frac{\partial}{\partial \lambda}(p_s v u) - \frac{\partial}{\partial \sigma}(p_s r u \dot{\sigma}) \\ & + (f + \frac{v}{r}) p_s r v - p_s r \frac{\partial \Phi}{\partial r} - r R T \frac{\partial p_s}{\partial r} \end{aligned} \tag{2.4}$$

Tangential momentum equation:

$$\begin{aligned} \frac{\partial}{\partial t}(p_s r v) = & -\frac{\partial}{\partial r}(p_s r u v) - \frac{\partial}{\partial \lambda}(p_s v v) - \frac{\partial}{\partial \sigma}(p_s v r \dot{\sigma}) \\ & - (f + \frac{v}{r}) p_s r u - p_s \frac{\partial \Phi}{\partial \lambda} - R T \frac{\partial p_s}{\partial \lambda} \end{aligned} \tag{2.5}$$

---

[1]The coordinate $\sigma = (p - p_T)/(p_s - p_T)$ can also be used in the model.

Potential temperature equation:

$$\frac{\partial}{\partial t}(p_s r\theta) = -\frac{\partial}{\partial r}(p_s ru\theta) - \frac{\partial}{\partial \lambda}(p_s v\theta) - \frac{\partial}{\partial \sigma}(p_s r\dot{\sigma}\theta) + rp_s Q \quad (2.6)$$

where u and v are radial and tangential velocities , $\dot{\sigma}$ is the vertical velocity in σ coordinates, Θ and T are potential temperature and temperature, ϕ is geopotential, R is the gas constant, and Q denotes a diabatic heat source.

The model equations do not include moist processes explicitly and diabatic heat source is specified. Unless stated otherwise, we assume that the heat source is symmetric with respect to the vortex center. Following Hack and Schubert (1986) the heating function approximates the apparent heat source from Yanai (1973) and has the form,

$$Q = a\hat{Q}\sin(\pi\sigma)\exp(-\alpha\sigma)\exp(-r^2/r_0^2), \quad (2.7)$$

where $\hat{Q} = 7.87^oC/\text{day}$, $\alpha = .554$, r_0=150 km. We assume that the magnitude of the heat source does not change with time, and that the distribution is constant relative to the vortex center.

2.2 Numerical scheme

2.2.1 Time integration

The Matsuno (1966) (or Euler backward) scheme is used for time integration. This scheme suppresses high-frequency gravity waves and was used in many other tropical cyclone models (Anthes, 1972; Kitade, 1980; Jones, 1977)

After initialization, equations (2.1)-(2.6) are integrated in the following order:

1. Time derivatives of prognostic variables (X_p=$p_s r$,$up_s r$,$vp_s r$, $\theta p_s r$) and vertical velocity $\dot{\sigma}p_s$ are calculated using the values in $t = t_1$.

2. Time step: $X_p^*(t_1 + \Delta t) = X_p(t_1) + \dot{X}_p(t_1)\Delta t$.

3. Variables p_s, u,v,θ are calculated and temperature is found from the potential temperature definition.

4. Geopotential is calculated.

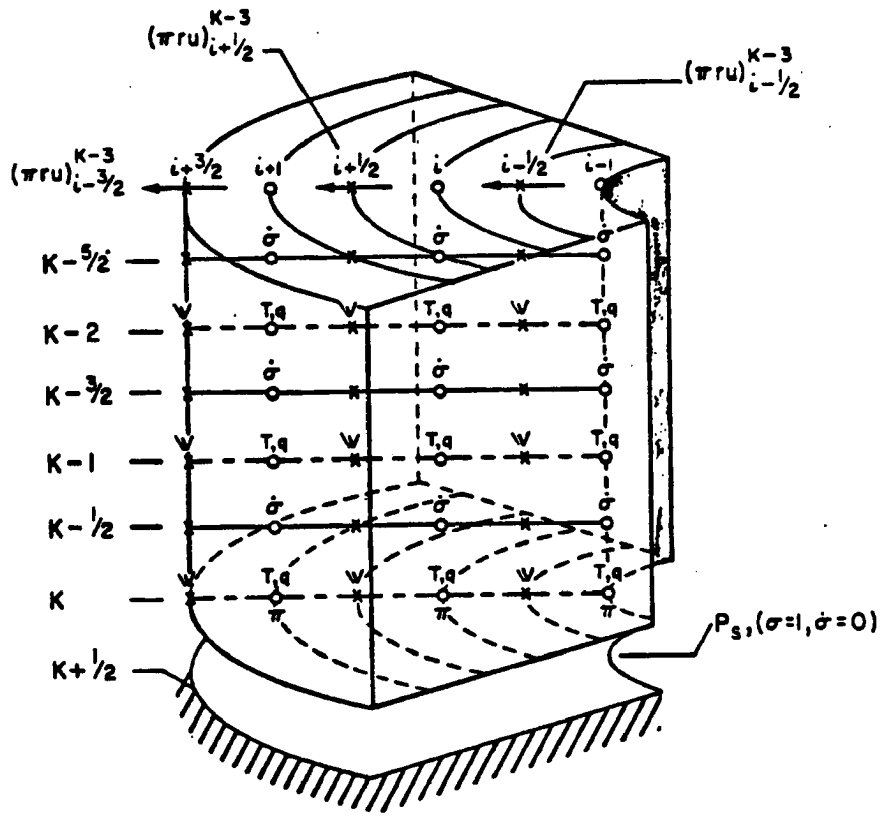

Figure 2.1: Radial and vertical distribution of model variables. From Hack (1980)

5. Time derivatives are calculated again using X_p^*.

6. Time step:$X_p(t_1 + \Delta t) = X_p(t_1) + \dot{X}_p(t_1 + \Delta t)\Delta t$

7. Diagnostic relations are solved again.

2.2.2 Structure of the model and vertical and radial differencing

The model consists of n layers. For most of the computations we use $n = 5$. Horizontal velocities and potential temperature are calculated in the middle of each layer. The vertical velocity $\dot{\sigma}$ is staggered. Following Hack and Schubert (1980) we use the Arakawa vertical differencing scheme. The detailed description of this scheme and the finite difference form of the equations can be found in Hack (1980). The radial differencing is identical to that used in Hack and Schubert (1980). The horizontal velocity (up_sr,vp_sr and u,v) is staggered relative to the $\theta p_s r$ geopotential ϕ, surface pressure p_s, and vertical velocity $\dot{\sigma} p_s$.

Fig. 2.1 shows the radial and vertical distribution of model variables.

2.2.3 Azimuthal structure and differencing

The model is half-spectral with Fourier representation in the azimuthal direction. All the model variables are expressed as

$$X(r,\lambda,\sigma) = \sum_{s=-S}^{S} x_s(r,\sigma)\exp(is\lambda) \tag{2.8}$$

Because all the X variables are real, the coefficients x_{-s} are complex conjugates of x_s, and for every σ and r we need to solve S+1 equations. Such a representation allows us to limit the number of tangential modes necessary to describe three-dimensional features of the moving vortex. In some barotropic models of the moving vortex (Willoughby, 1988; Peng and Williams, 1990), the asymmetries are limited to tangential wavenumber $s = 1$. Indeed, the horizontally uniform wind field and β effect can be described using wavenumbers 0 and 1. If the y axis of the cartesian coordinate system is oriented in the north-south direction with y increasing toward north, the constant zonal wind is $(U_c, 0)$, and the Coriolis parameter on the β plane is $f = f_0 + \beta y$. In cylindrical coordinates the velocity and f become

$$\begin{aligned} u &= U_c\cos\lambda, \\ v &= -U_c\sin\lambda, \\ f &= \beta y = \beta r\cos\lambda. \end{aligned} \tag{2.9}$$

Therefore the spectral coefficients are:

$$\begin{aligned} u(r,0,\sigma) = v(r,0,\sigma) &= 0, \\ f(r,0) &= f_0, \\ u(r,1,\sigma) &= (U_c/2, 0), \\ v(r,1,\sigma) &= i\cdot u(r,1,\sigma,), \\ f(r,1) &= \beta r(0,-0.5), \end{aligned} \tag{2.10}$$

For $s > 1$ $u(r,s,\sigma) = v(r,s,\sigma) = f(r,s) = 0$.

Observations show (William M. Gray - personal communication) that proper representation of the steering current demands that horizontal shear is also included. Therefore,

Table 2.1: The comparison of time needed on Cray-YMP for 1000 multiplications using interaction coefficients and transform method.

S	time (s)	
	interaction coefficients	transform method (with FFT)
2	.046	.109
3	.077	.404
4	.118	.182
5	.169	.606
6	.227	.806
7	.295	.823
8	.376	.364
9	.465	1.534

at least the component with $s = 2$ (linear shear) is needed. The analysis of instabilities in the hurricane outflow layer (Chapter V) shows that the amplitude of dynamic asymmetries which develop in an isolated hurricane decreases with increasing tangential wavenumber, and practically approaches zero for $s > 2$. Therefore, for most of our experiments we consider four (0,1,2,3) tangential wavenumbers. If the problem demands higher azimuthal resolution, more tangential components can be used.

Because of the low number of spectral components all calculations are carried out in spectral space. For nonlinear terms, interaction coefficients are explicitly determined.

$$(uv)_s = \sum_{j=-S}^{S} u_j v_{s-j} \tag{2.11}$$

Generally, for spectral models calculating interaction coefficients is very inefficient, and transform methods utilizing the FFT are used instead. In our case, however, where the spectral representation is used only in one direction and number of spectral coefficients is very small, using the FFT does not have any real advantages. Table 2.1 shows the comparison of time needed to multiply two variables using the interaction coefficients and transform method depending on the number of spectral components. It can be seen that for $S < 8$, especially if S is not the power of 2, calculating interaction coefficients is faster. In the model code, the subroutines which calculate nonlinear terms can be separated and replaced by routines using the FFT if necessary.

Table 2.2: The value of p_s^{-1} where $p_s(r,0,\sigma) = (100000.,0)$, $p_s(r,1,\sigma) = (2000.,0)$, and $p_s(r,2,\sigma) = (400.,0)$. NI is the number of iterations, s the tangential wavenumber

NI	s			
	0	1	2	3
1	9.9999997×10^{-6}	-1.9999999×10^{-7}	$-4.\times10^{-8}$	-3.9999999×10^{-9}
2	1.0008323×10^{-5}	-1.9836799×10^{-7}	-3.5839999×10^{-8}	-2.4000000×10^{-9}
3	1.0008223×10^{-5}	-1.9863224×10^{-7}	-3.5938584×10^{-8}	-2.4930573×10^{-9}
4	1.0008234×10^{-5}	-1.9862679×10^{-7}	-3.5930931×10^{-8}	-2.4899887×10^{-9}
4	1.0008234×10^{-5}	-1.9862721×10^{-7}	-3.5931148×10^{-8}	-2.4901681×10^{-9}
5	1.0008234×10^{-5}	-1.9862721×10^{-7}	-3.5931148×10^{-8}	-2.4901681×10^{-9}
6	1.0008234×10^{-5}	-1.9862719×10^{-7}	-3.5931134×10^{-8}	-2.4901619×10^{-9}
7	1.0008234×10^{-5}	-1.9862719×10^{-7}	-3.5931134×10^{-8}	-2.4901621×10^{-9}
8	1.0008234×10^{-5}	-1.9862719×10^{-7}	-3.5931134×10^{-8}	-2.4901621×10^{-9}

Besides multiplications of two variables, the nonlinear terms in the governing equations include raising p_s to the real power (R/c_p in potential temperature definition and -1 when variables are divided by surface pressure). Since the symmetric part of the surface pressure p_{ss} is much larger than asymmetric part p_{sa} we use the Taylor expansion:

$$p_s^{ww} = p_{ss}^{ww}\left(1 + \frac{p_{sa}}{p_{ss}}ww + \frac{1}{2!}\frac{p_{sa}^2}{p_{ss}^2}ww(ww-1)\ldots\right) \tag{2.12}$$

Because $p_{ss} >> p_{sa}$ and we use only three spectral components the procedure converges really fast and only a few terms in the Taylor expansion are needed (Table 2.2). The time necessary to invert surface presure for $S = 3$ is comparable for transform and interaction coefficient method. 1000 operations using transform method takes 0.41s on the Cray YMP. The same calculation using interaction coefficients takes 0.33 s for NI=4 and 0.56s for NI=7.

2.3 Coordinate stretching

In modeling of vortex-environment interaction, a large domain needs to be used. At the same time the area close to the cyclone center has to be resolved with a relatively fine grid. In balanced models (Schubert and Hack, 1983; Emanuel, 1989), this problem can be avoided by using the potential radius as a radial coordinate. For primitive equation models, coordinate stretching or grid nesting has to be used. Grid nesting is often used in three-dimensional models (Jones, 1977; Kitade, 1980)

In our model, the azimuthal structure is determined by Fourier components, so only the radial coordinate needs to be modified. We decided to use coordinate stretching instead of nesting in order to avoid the interface problems. The new coordinate $\hat{r}$ is defined as:

$$\hat{r}(r) = (r/1000. + r_a)^{1/\gamma} \tag{2.13}$$

so that $r = (\hat{r}^\gamma - r_a)1000$. For γ larger than one, and uniformly spaced $\hat{r}$ the radial resolution increases with decreasing radius. The shifting by r_a was used to avoid infinite derivatives at $r = 0$.

To account for coordinate stretching the numerical scheme has to be modified by expressing the radial derivatives $\partial X/\partial r$ as $\partial X/\partial \hat{r} \times \partial \hat{r}/\partial r$. In addition, the weights have to be included in the averaging of variables in the radial direction, so that

$$x(k+1/2) = x(k)(1. - wwr(k+1/2)) + x(k+1)wwr(k+1/2), \tag{2.14}$$

where $x(k+1/2)$ is the value of the variable x between two grid points. wwr denotes the weighting factor and is calculated using the assumption that between two grid points x changes linearly with radius r (and not with stretched coordinate $\hat{r}$):

$$wwr(k+1/2) = (r(k+1/2) - r(k))/(r(k+1) - r(k)). \tag{2.15}$$

If there is no stretching wwr=0.5. Fig. 2.2 shows the radius, derivative $\partial \hat{r}/\partial r$ and weighting factors as a function of $\hat{r}$ calculated for $\gamma = 1.8$

As can be seen from Fig. 2.2 the weighting factors are very close to 0.5. That could suggest that they should not influence the computations and we could arithmetically average the variables in the stretched coordinates. However, Figs. 2.3- 2.5 show that neglecting weighting factors can cause serious problems near the vortex center.

2.4 Vortex movement

The equations for the moving vortex can be solved in the coordinate system moving with the vortex or the system tied to the earth. The first approach was used in the barotropic models in which the structure of the moving vortex, rather than motion itself,

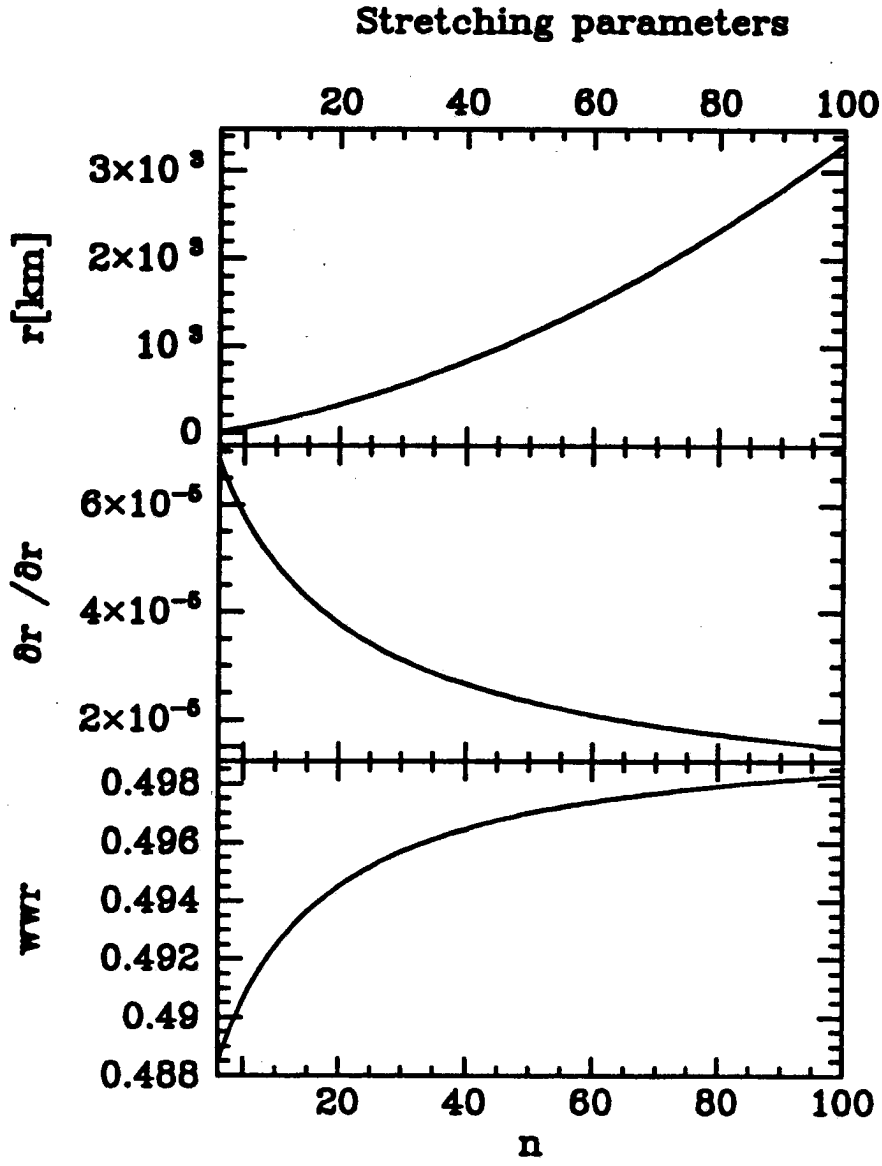

Figure 2.2: a) The radius r , b) derivative $\partial\hat{r}/\partial r$ and c) weighting factor for $\gamma = 1.8$, as a function of radial gridpoint index n

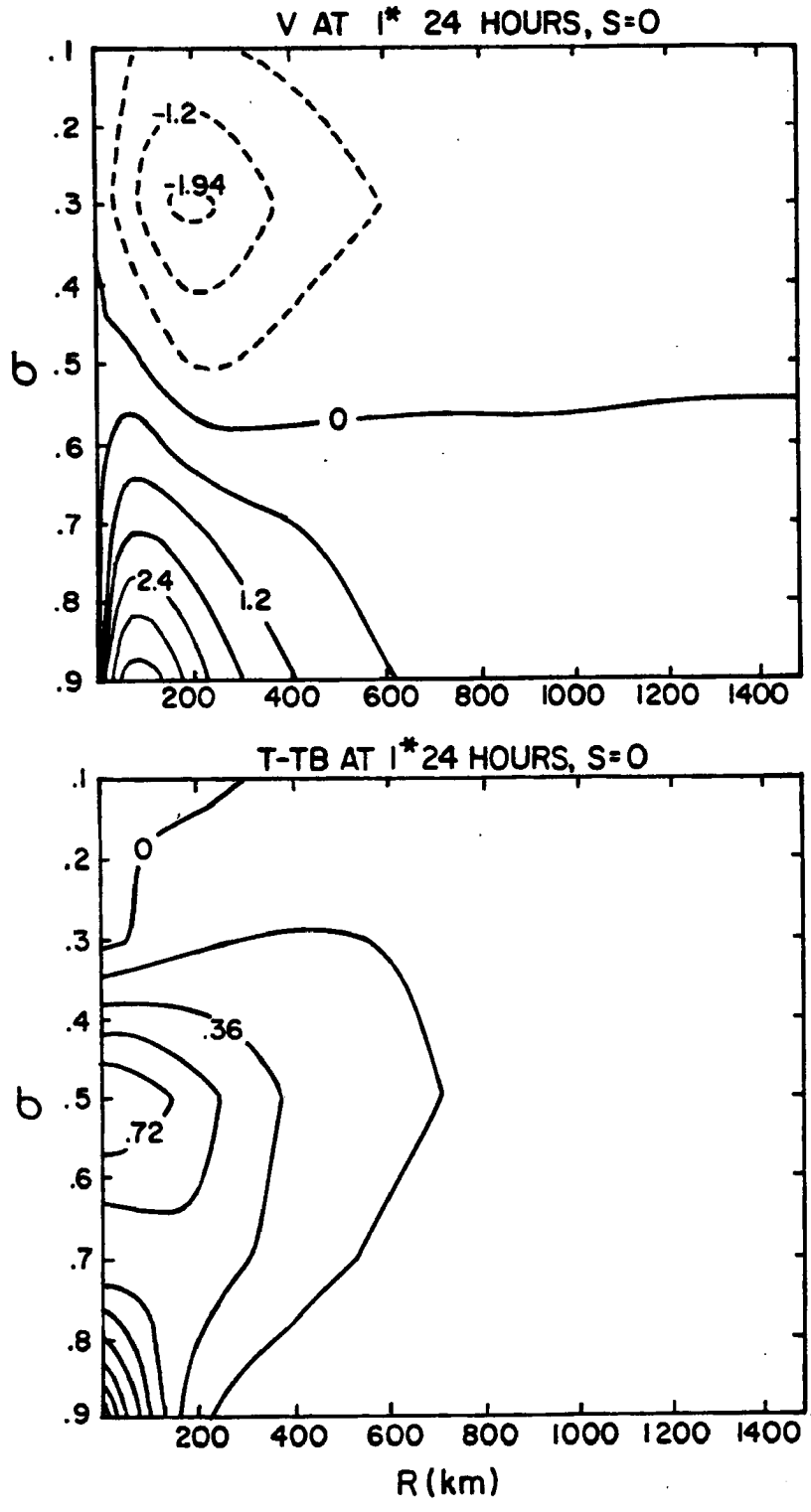

Figure 2.3: The tangential velocity and temperature perturbation after 24 h of calculation for 60 points resolution and no coordinate stretching($\Delta r = 30$km).

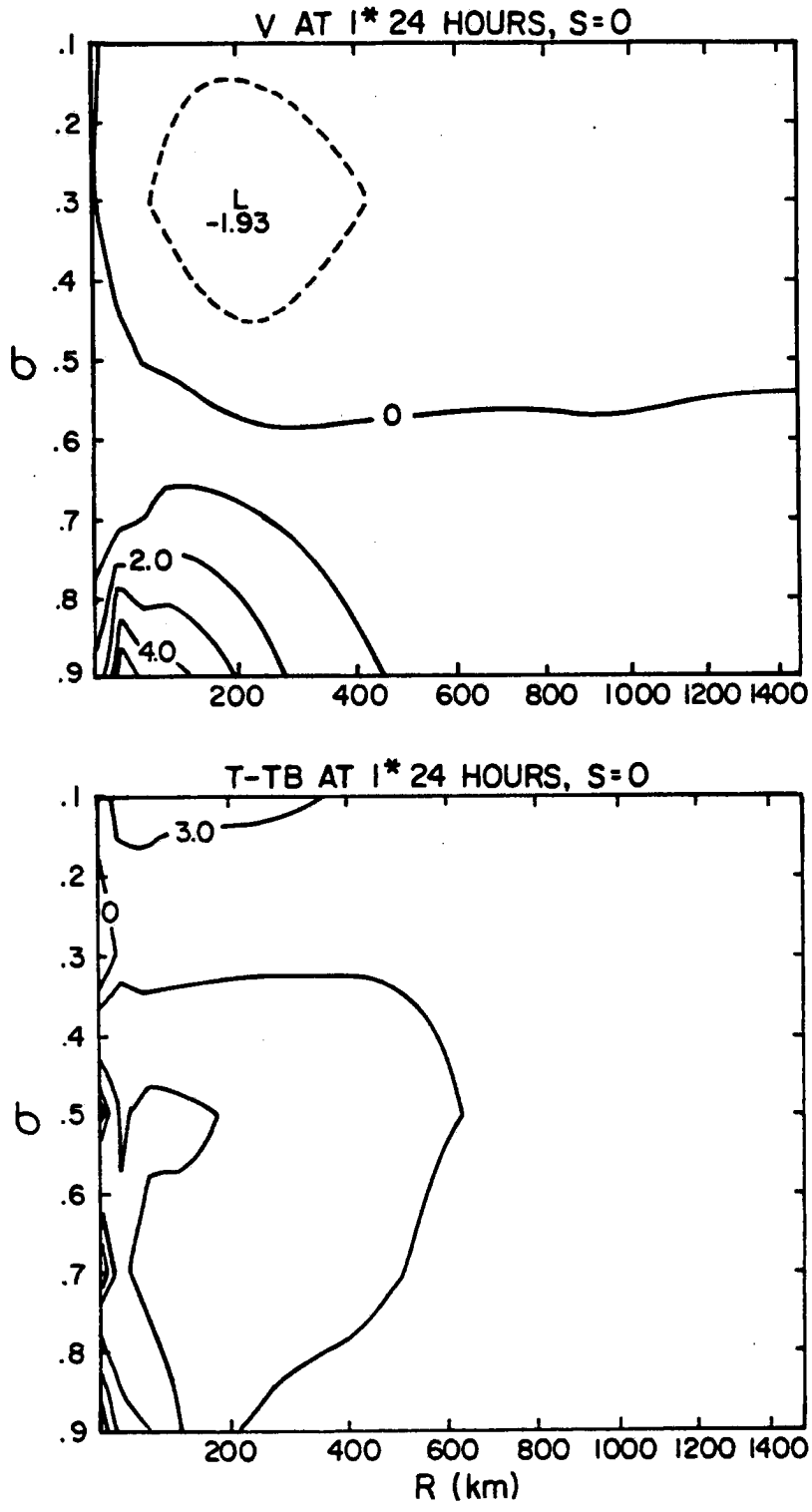

Figure 2.4: The tangential velocity and temperature perturbation after 24 h of calculation for 30 points resolution and stretching ($\gamma = 1.6$) but with no weighting factors.

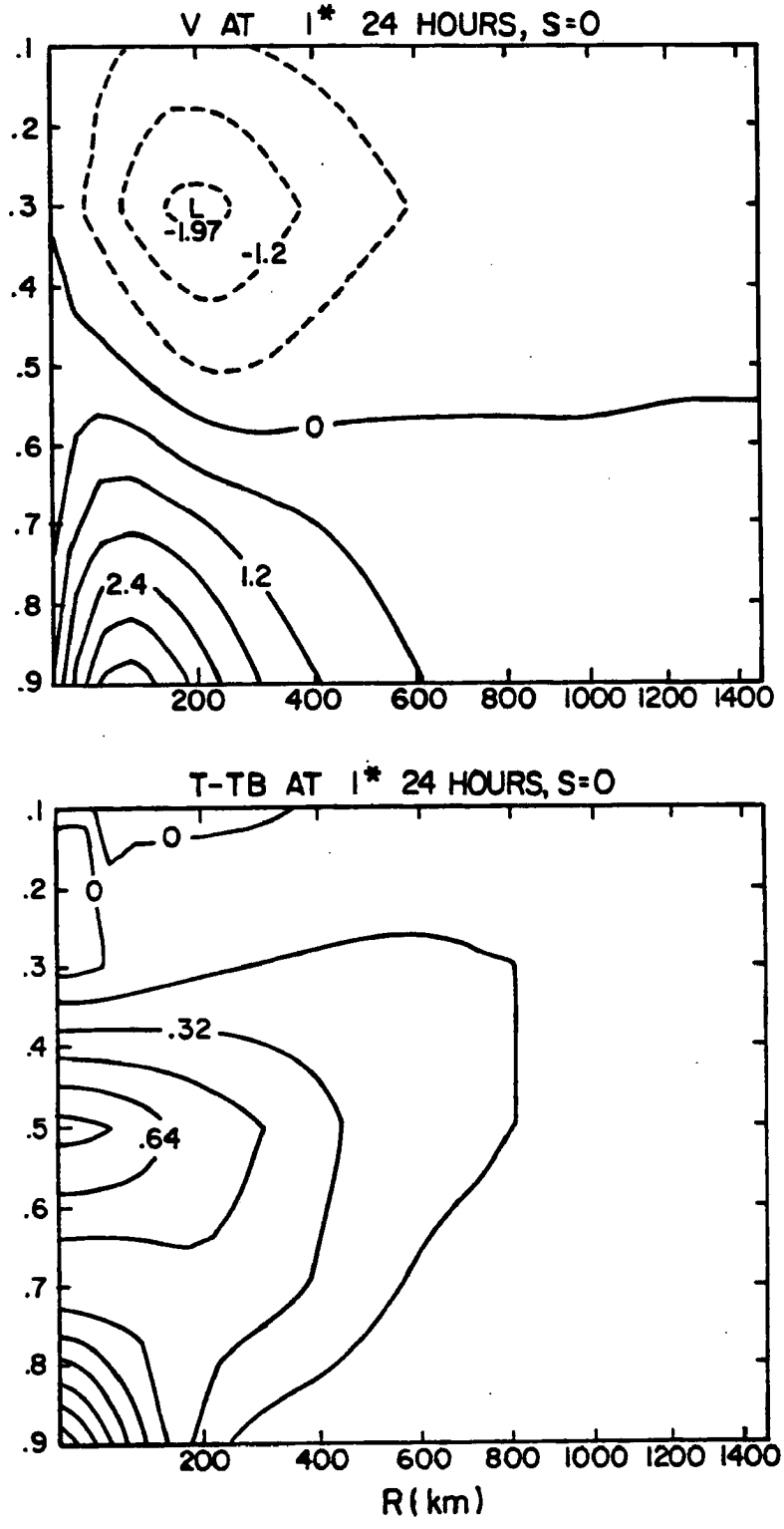

Figure 2.5: The tangential velocity and temperature perturbation after 24 h of calculation with 30 points resolution,stretching ($\gamma = 1.6$) and weighting factors included.

the vortex center and coordinate center exceeds r_d the coordinate system is relocated and all variables are interpolated in the new coordinates. The magnitude of r_d is chosen depending on intensity of the vortex. For large, weak vortices the gradients of variables near the vortex center are not very large and vortex displacement does not create large asymmetries. As the vortex begins to intensify, the tangential wind maximum increases and moves toward the center, and the variables change rapidly at small radii. In this case even small displacement of the vortex creates large asymmetries in surface pressure field. In this case r_d has to be small. In our calculations we use r_d =20 km for experiments with weak vortices (initial maximum wind 10 ms^{-1})and r_d=5 km for intense (initial wind 30 ms^{-1}) vortices.

2.5 Boundary conditions and forcing

Since the governing euations are formulated in the flux form and definition of the vertical coordinate demands that the vertical velocity is zero at the upper and lower boundary, boundary conditions simply state that vertical fluxes vanish at $\sigma = 1$ and $\sigma = 0$. At the vortex center the radial fluxes vanish, because all prognostic variables are multiplied by radius. In some cases (e. g. pressure term in radial momentum equation) we have to calculate the radial derivative of pressure p and geopotential Φ rather that pr and Φr. In such cases the condition that all physical fields have to be continuous at the vortex center can be used.

$$
\begin{aligned}
u(0,0,\sigma) = v(0,0,\sigma) &= 0, \\
\frac{\partial p_s(0,0,\sigma)}{\partial r} &= 0, \\
\frac{\partial \Phi(0,0,\sigma)}{\partial r} &= 0, \\
\frac{\partial \dot{\sigma}(0,0,\sigma)}{\partial r} &= 0, \\
\frac{\partial \theta(0,0,\sigma)}{\partial r} &= 0, \\
\frac{\partial u(0,1,\sigma)}{\partial r} = \frac{\partial v(0,1,\sigma)}{\partial r} &= 0.
\end{aligned}
\tag{2.16}
$$

All other variables vanish for r=0.

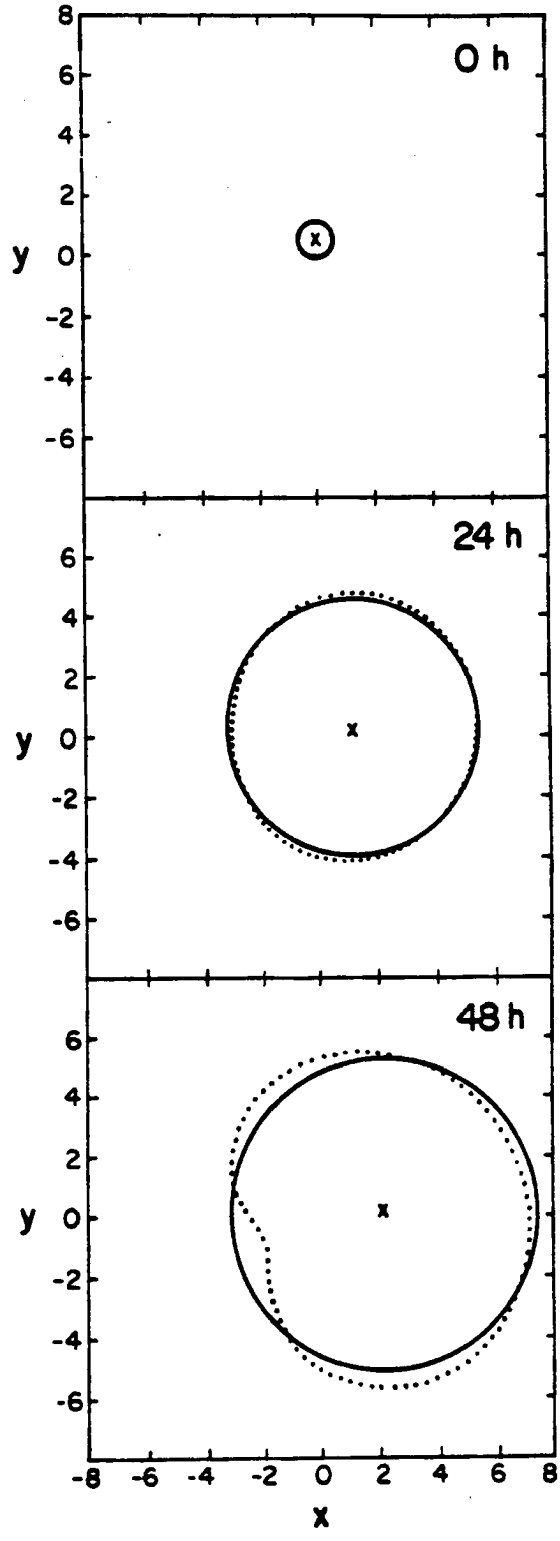

Figure 2.6: Tracking the moving vortex using 1008 mb contour

the vortex center and coordinate center exceeds r_d the coordinate system is relocated and all variables are interpolated in the new coordinates. The magnitude of r_d is chosen depending on intensity of the vortex. For large, weak vortices the gradients of variables near the vortex center are not very large and vortex displacement does not create large asymmetries. As the vortex begins to intensify, the tangential wind maximum increases and moves toward the center, and the variables change rapidly at small radii. In this case even small displacement of the vortex creates large asymmetries in surface pressure field. In this case r_d has to be small. In our calculations we use r_d =20 km for experiments with weak vortices (initial maximum wind 10 ms^{-1})and r_d=5 km for intense (initial wind 30 ms^{-1}) vortices.

2.5 Boundary conditions and forcing

Since the governing euations are formulated in the flux form and definition of the vertical coordinate demands that the vertical velocity is zero at the upper and lower boundary, boundary conditions simply state that vertical fluxes vanish at $\sigma = 1$ and $\sigma = 0$. At the vortex center the radial fluxes vanish, because all prognostic variables are multiplied by radius. In some cases (e. g. pressure term in radial momentum equation) we have to calculate the radial derivative of pressure p and geopotential Φ rather that pr and Φr. In such cases the condition that all physical fields have to be continuous at the vortex center can be used.

$$
\begin{aligned}
u(0,0,\sigma) = v(0,0,\sigma) &= 0, \\
\frac{\partial p_s(0,0,\sigma)}{\partial r} &= 0, \\
\frac{\partial \Phi(0,0,\sigma)}{\partial r} &= 0, \\
\frac{\partial \dot{\sigma}(0,0,\sigma)}{\partial r} &= 0, \\
\frac{\partial \theta(0,0,\sigma)}{\partial r} &= 0, \\
\frac{\partial u(0,1,\sigma)}{\partial r} = \frac{\partial v(0,1,\sigma)}{\partial r} &= 0.
\end{aligned}
\tag{2.16}
$$

All other variables vanish for r=0.

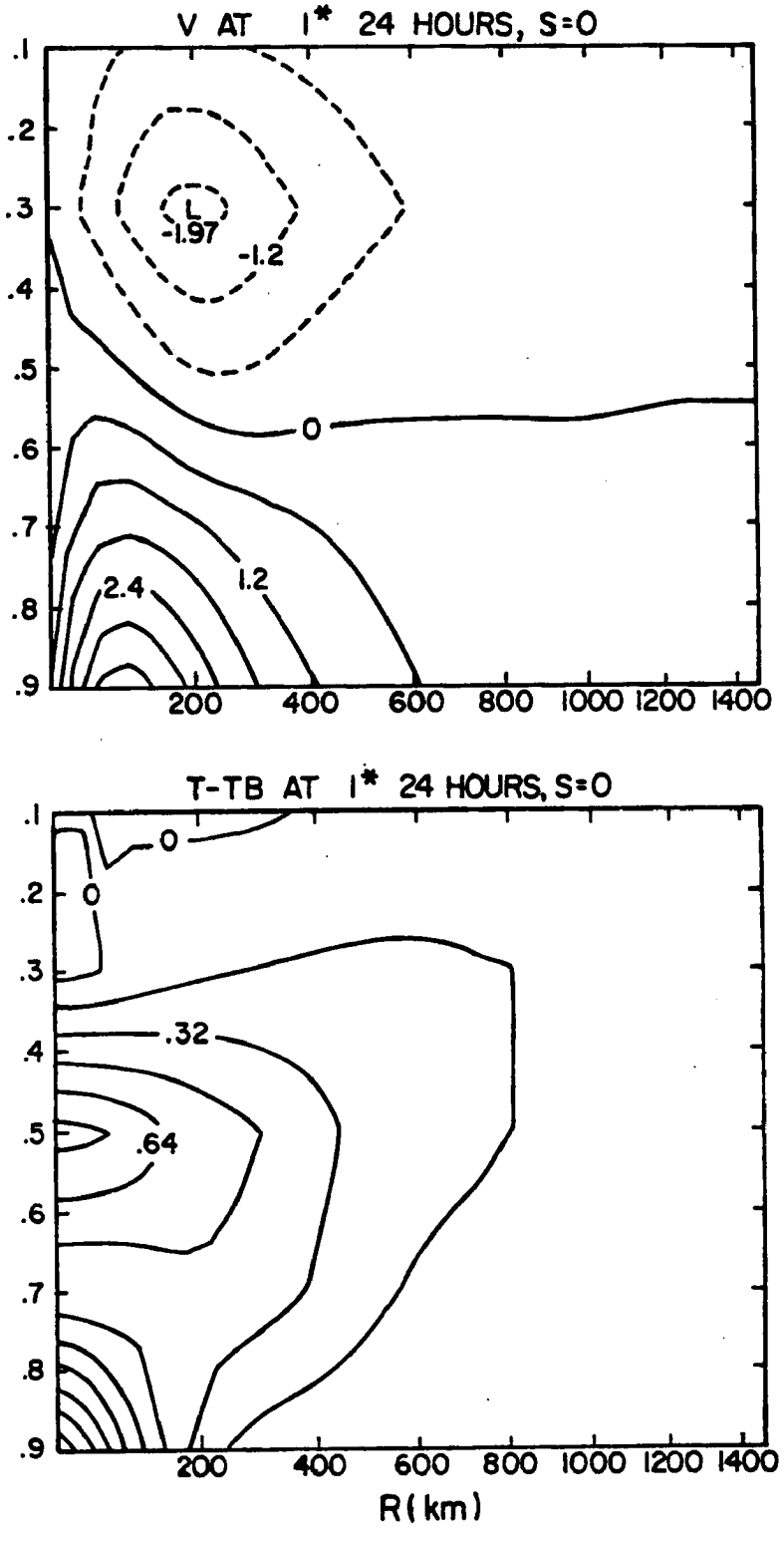

Figure 2.5: The tangential velocity and temperature perturbation after 24 h of calculation with 30 points resolution,stretching ($\gamma = 1.6$) and weighting factors included.

was sought (Willoughby, 1988; Peng and Williams, 1990). In these models the movement of the vortex was known either from the full nonlinear model (Peng and Williams, 1990) or from a variational principle (Willoughby, 1988). In three dimensional models the equations are usually solved in the stationary coordinate system. However, if the variable grid is used in the model, the fine grid (or grids) has to follow the hurricane. That can be done continuously as in Kitade (1980) where the equations for the fine grid have Lagrangian form, or by relocating the coordinate system to the new position after the hurricane moves a certain distance (Jones, 1977; Kurihara and Bender, 1980)

Our model is formulated in the stationary coordinate system. Such formulation creates two problems. One is similar to that encountered in nested grids models — the center of the vortex "escapes" from the area where the coordinate stretching and Fourier expansion provide the finest resolution. Another problem results from the use of spectral representation of the variables. When the vortex center is too far from the coordinate center the asymmetries are mainly the result of this mismatch and not the vortex dynamics. This is an especially undesirable feature in the case of pressure field. Since we use the Taylor expansion to calculate some of the nonlinear terms involving the surface pressure, it is quite important that the surface pressure field is as symmetric as possible.

To deal with these problems we use the procedure similar to that in Jones (1977) and Kurihara and Bender (1980) and relocate the coordinate center to match the vortex center if the distance between them exceeds the prescribed limit r_d. The definition of the vortex center is based on the surface pressure field. In observations, the surface pressure contours close to the cyclone center rather closely approximate the circle. We define the vortex center as a center of such a circle. To calculate it we choose the pressure contour and fit the circle to this contour using the least squares method (Fig. 2.6). That way, the asymmetric component of the pressure field is minimized. Choosing the different pressure contours gives similar results. However, care must be taken to choose the closed contour. The vortex center is calculated every hour. Since the heating function is defined relative to the vortex center and not the coordinate center, the heating distribution has to be calculated to correspond to the new vortex center. After the distance between

The area of integration is divided into two parts. The inner part consists of a circle with radius r_i = 1500km. A ring between r_i = 1500 km and r_a = 3200 km forms the outer part of the domain which acts as a "sponge layer" for the inner part of the domain. At $r = r_a$ radial derivatives of prognostic variables are prescribed. In addition, prognostic variables in the outer region are relaxed toward the prescribed environmental values. The prognostic equations in this area contain the additional term —"environmental forcing" which has the form of Newtonian nudging:

$$F_e = \frac{-(x - x_e)}{T}, \tag{2.17}$$

where the environmental variables x_e are prescribed *a priori* and the time scale T increases exponentially between $r = r_a$ and $r = r_i$.

$$T = A \exp - \left(\frac{(r - r_a)^2}{r_w^2} \right), \tag{2.18}$$

where A = 20000s and r_w = 700km

When the coordinate system is adjusted to match the vortex center, the variables outside the boundary ($r = r_a + r_d$) are extrapolated.

Chapter 3

INTERACTION BETWEEN UPPER AND LOWER LAYERS OF A BAROCLINIC VORTEX

3.1 Movement of the baroclinic vortex on the β-plane

The movement of a barotropic vortex on the β-plane can be easily understood if we consider the vortex as a"packet" of Rossby waves, with the outer circulation projected on the longer waves and inner circulation projected on the shorter waves. Since Rossby waves move west due to the advection of earth's vorticity, the vortex also moves west. However, longer waves move faster, creating a distortion of an initially symmetric vortex and thus asymmetric flow at the vortex center. The direction of this flow depends on whether the vortex is cyclonic or anticyclonic. In the cyclonic vortex, dispersion of Rossby waves causes northward flow at the center and northward movement of the vortex, while the anticyclonic vortex tends to move toward the south. This "linear" picture is modified by nonlinear interactions which hold the vortex together. This qualitative description of the movement of a vortex on the β-plane is consistent with most of the results of barotropic nonlinear models. All numerical models agree in their prediction of north-west movement of cyclonic vortices. As indicated by analogy with Rossby waves, the speed of motion depends on size rather than intensity of the vortex (large vortices move faster). As shown by Fiorino (1989), changes of the larger (λ = 1500km) scales of the vortex circulation influence the vortex motion to a greater degree than smaller scale (like intensity changes) processes. However, there is some indication that more intense vortices move slightly faster to the north.

Some features of a vortex moving on the-β plane cannot be easily explained. The linear models (Willoughby, 1988) suggest that the propagation of the vortex is proportional

to the total relative angular momentum (RAM) of the vortex. In Willougby's (1988) linear, steady state model, the vortex with zero angular momentum does not move. This simple relationship does not hold for the nonlinear calculations. Shapiro and Ooyama (1990) show that although the vortex with zero angular momentum is non-dispersive (and therefore our idealized picture would indicate no meridional motion), it still moves toward the north-west. They indicate that there is no simple way to tie the vortex motion to the total RAM of the vortex.

The situation becomes even more complicated in the case of the baroclinic vortex. Some investigators (Gray, 1991; Wang and Li, 1991) have suggested that the coupling between the lower cyclonic and upper anticyclonic layers, caused by secondary circulation, should reduce the β-induced vortex motion. However, as in barotropic models, three-dimensional hurricane models (Madala and Piacsek, 1975; Kitade, 1980; DeMaria, 1983; Shapiro and Ooyama, 1990) also indicate the north-westward vortex movement on the β plane.

In this section, we test the sensitivity of the β-induced vortex motion to the vertical coupling between the vortex layers. The model is run on the β plane with no environmental flow. All experiments in this section use the same initial vortex (Fig. 3.1) which was obtained in a symmetric version of the model.

Using the same initial conditions, we run three experiments. In the first experiment (βNI) there is no diabatic heating. Therefore the secondary circulation driven by heating does not develop and the upper and lower layers of the vortex move, for the most part, independently of one another. In the second ($\beta D0$) and third ($\beta D20$) experiments symmetric diabatic heating is added. In the third experiment ($\beta D20$), vertical diffusion of momentum is also included. Constant diffusion coefficient $K = 20\mathrm{m}^2\,\mathrm{s}^{-2}$ is used. Momentum mixing is included only in the asymmetric terms. This assumption allows us to include only the terms which directly influence the motion, while leaving the symmetric structure of the vortex unchanged.

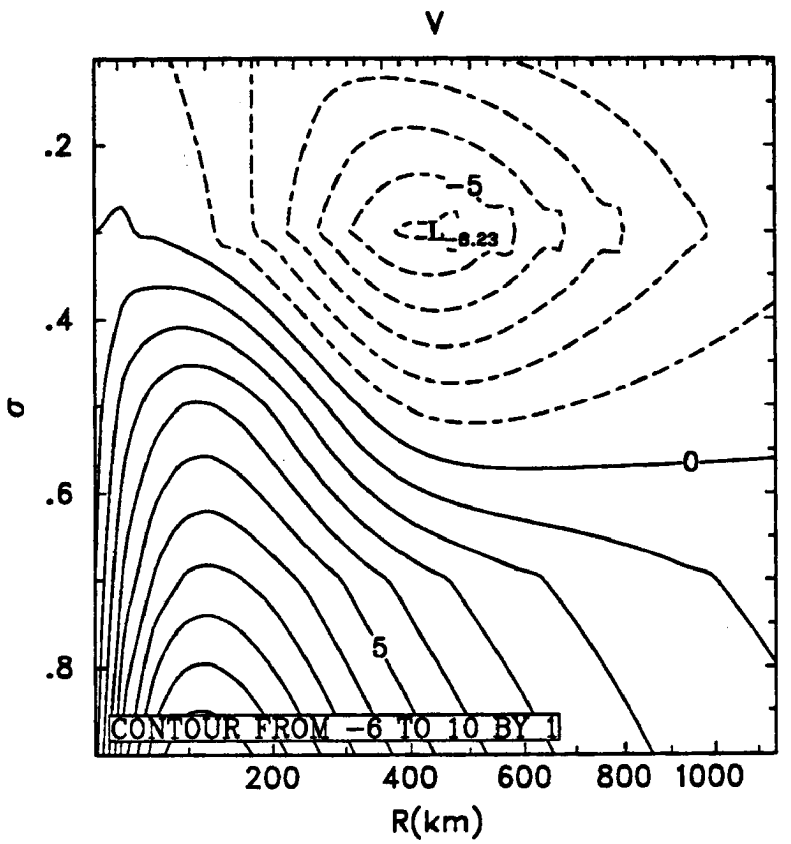

Figure 3.1: Initial symmetric vortex.

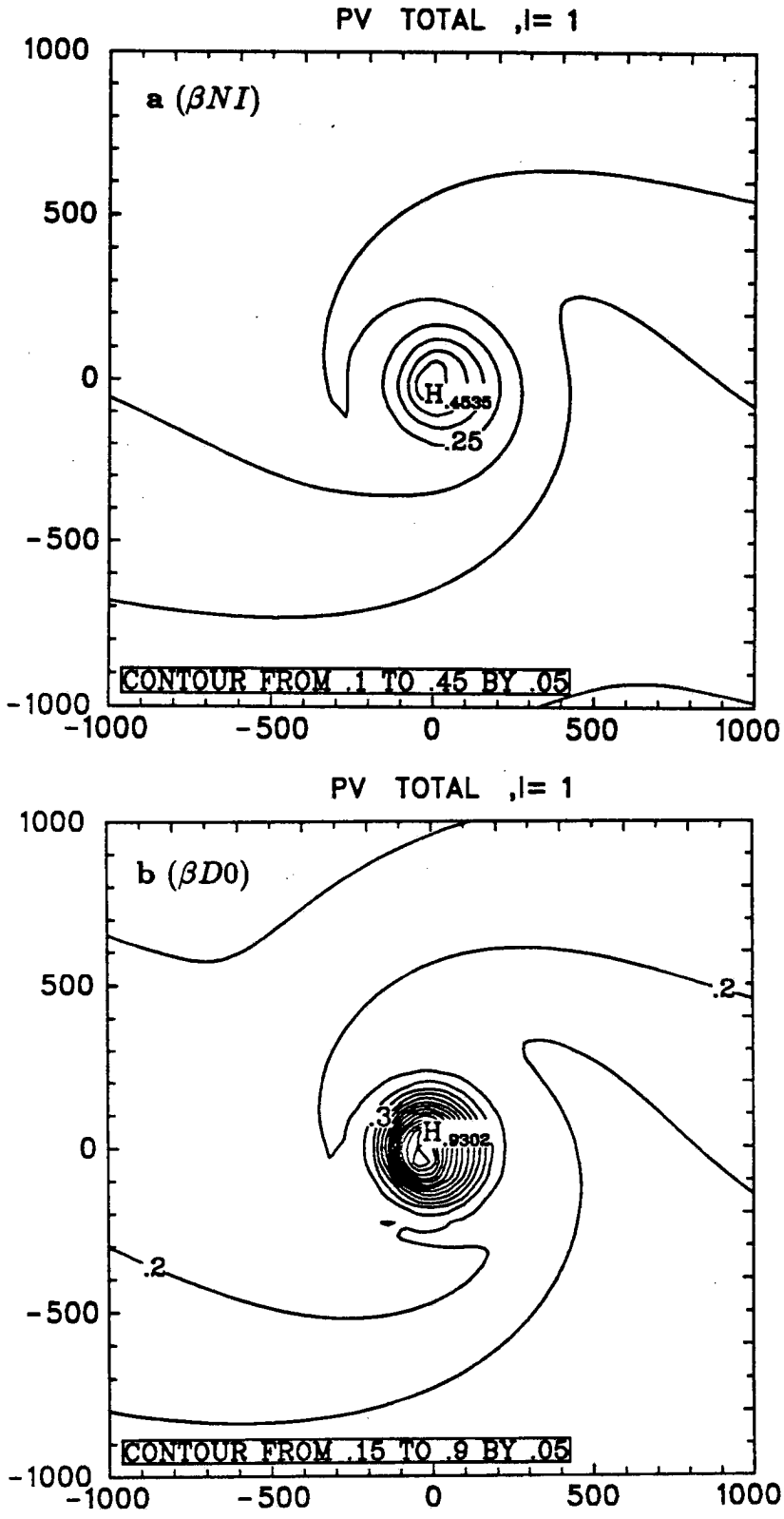

Figure 3.2: Total potential vorticity at 800 mb. a) experiment βNI b) experiment βD0.

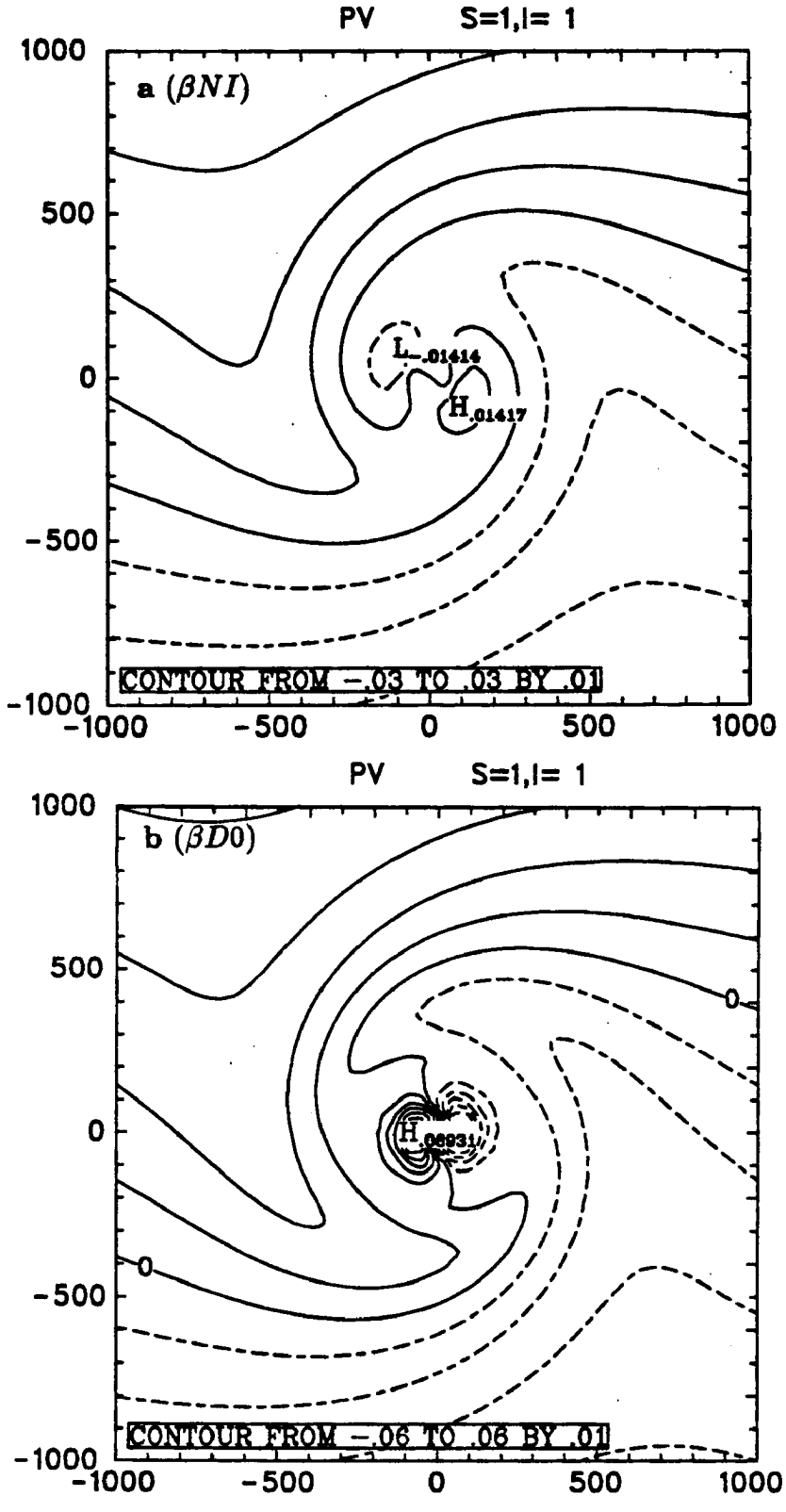

Figure 3.3: Asymmetric ($s = 1$) potential vorticity at 800 mb. a) experiment βNI b) experiment βD0.

Figs. 3.2 and 3.3 show the 800 mb normalized potential vorticity [2] field at 48 hours. The figures show all the "classical" characteristics of a vortex moving on the β-plane. The earth's vorticity is advected by the vortex circulation, creating an increase of potential vorticity west of the vortex and decrease of potential vorticity to the east. The resulting wind asymmetry advects the vortex toward the north-west. The potential vorticity fields in βNI and βD0 at this level are similar, although the vortex in non-interacting case is less intense.

However, at 200 mb, the potential vorticity fields (Fig. 3.4 and 3.5) are quite different. In βNI the upper level negative anomaly is displaced toward the south relative to the low-level vortex, due to the advection of the earth's vorticity by the anticyclonic circulation. In βD0 the 200 mb potential vorticity pattern is much more complicated. The advective effects of the background vorticity by the vortex circulation can still be seen, but in addition the secondary circulation transports high potential vorticity air from below, creating a maximum near the vortex center. This maximum slowly moves toward the south along with the entire upper-level vortex. These features are similar to the characteristics observed in the upper-layer potential vorticity field from Shapiro's (1991) hurricane model, even though our model does not include convective parameterization, but only specified *a priori* diabatic heating.

Vortex tracks for experiments βNI, βD0, and βD20 are shown in Fig. 3.6. Contrary to Wang's (1991) suggestion, the coupling caused by diabatic heating does not reduce the meridional speed of the vortex. In fact, vortices in βD0 and βD20 move toward the north slightly faster than βNI. This may be caused by the fact that the vortex in βNI is less intense. One should note that the effects of momentum exchange between the upper and lower layers by momentum advection and diffusion, reduce the westward, not northward speed of the vortex. Careful examination of the asymmetric $s = 1$ component shows that the east-west vorticity gradient is smaller in βD0 than in βNI. This may be due to the fact that potential vorticity anomalies east and west of vortex center have opposite signs

---

[2]The details of potential vorticity calculation in σ coordinates are contained in Appendix A

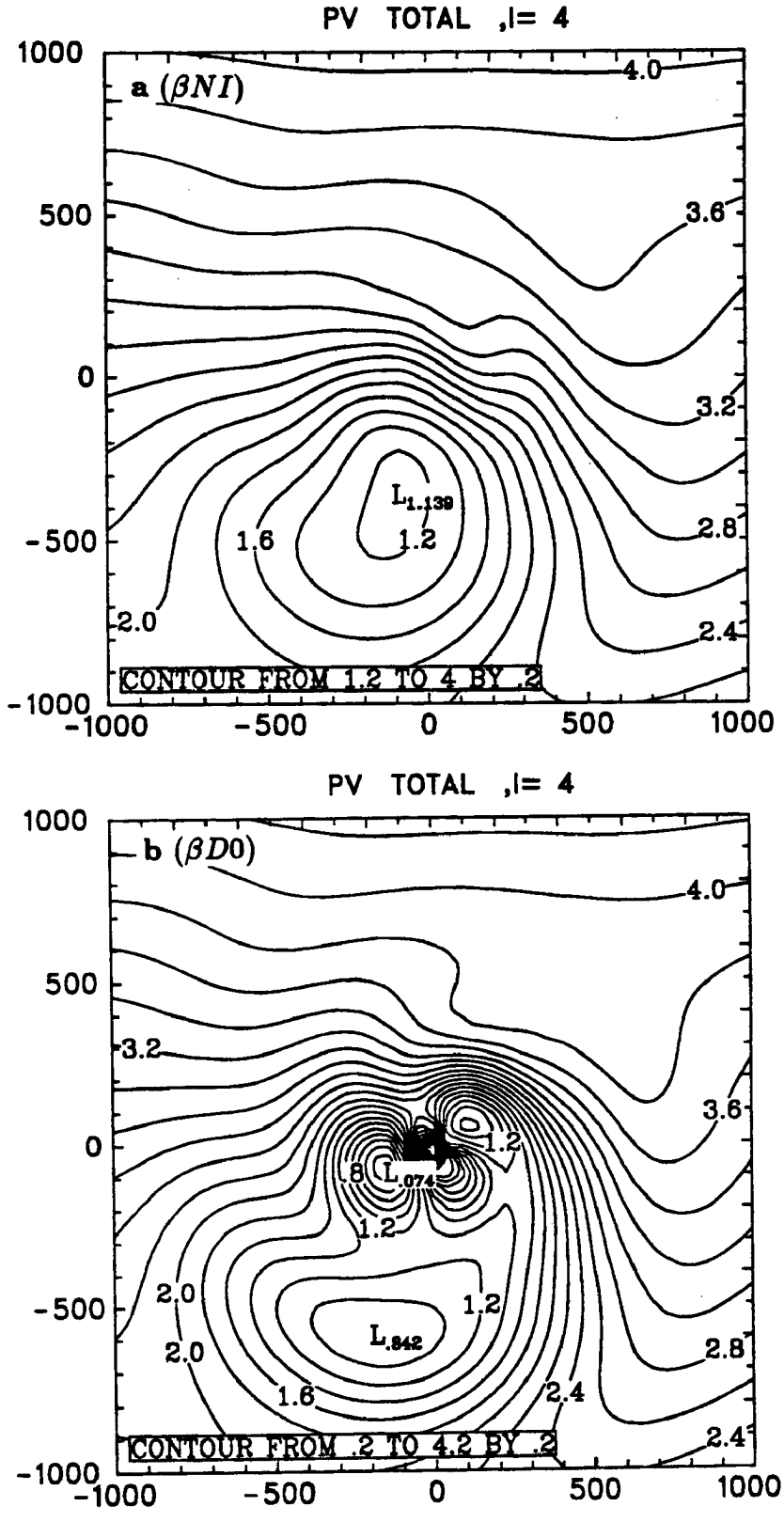

Figure 3.4: Total potential vorticity at 200 mb. a) experiment βNI b) experiment βD0.

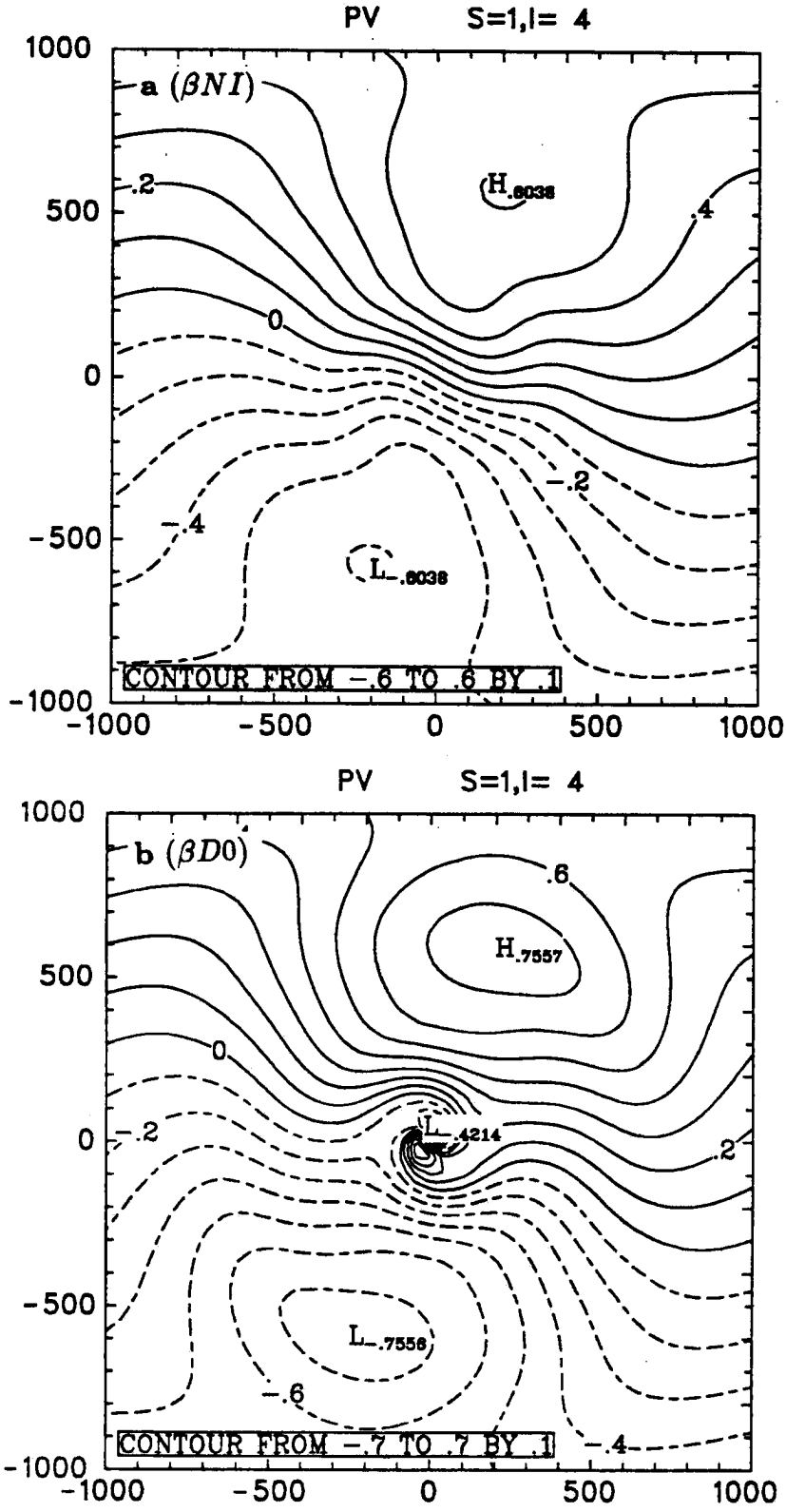

Figure 3.5: Asymmetric ($s = 1$) potential vorticity at 200 mb. a) experiment βNI b) experiment βD0.

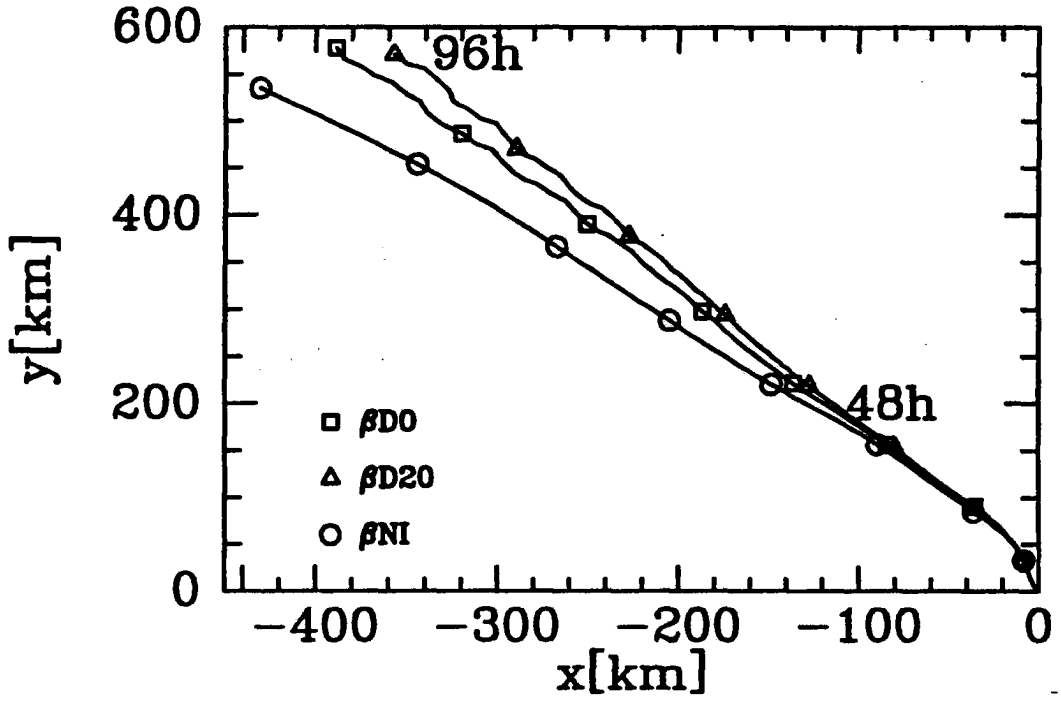

Figure 3.6: Vortex track in experiments βNI, βD0 and βD20.

at upper and lower levels. The vertical mixing between levels can reduce the magnitude of these anomalies and affect the westward speed of the vortex.

Despite the small differences in westward propagation speed, vortices in all three experiments move toward the north-west. As in other nonlinear models they initially move toward the north and then speed up in westward direction. The zonal and meridional velocity for the experiment βD0 is shown in Fig. 3.7. After about three days the vortex moves toward the north-west with the speed of 2.8 m/s.

Determining the role of the β effect in cyclone motion using observational data is rather complicated. The environmental flow is not uniform and has potential vorticity gradients of its own. In addition, the definition of the steering flow and propagation vector is rather ambiguous and depends on the radii at which the steering flow is calculated. Even if we agree on a standard definition of steering flow as the 5-7 degree, 300-850 mb average wind around the storm, there is still a difference of opinion on the cause of observed propagation. For example, Carr and Elsberry (1990), after studying the properties of the propagation vector for composite hurricanes, reached the conclusion that

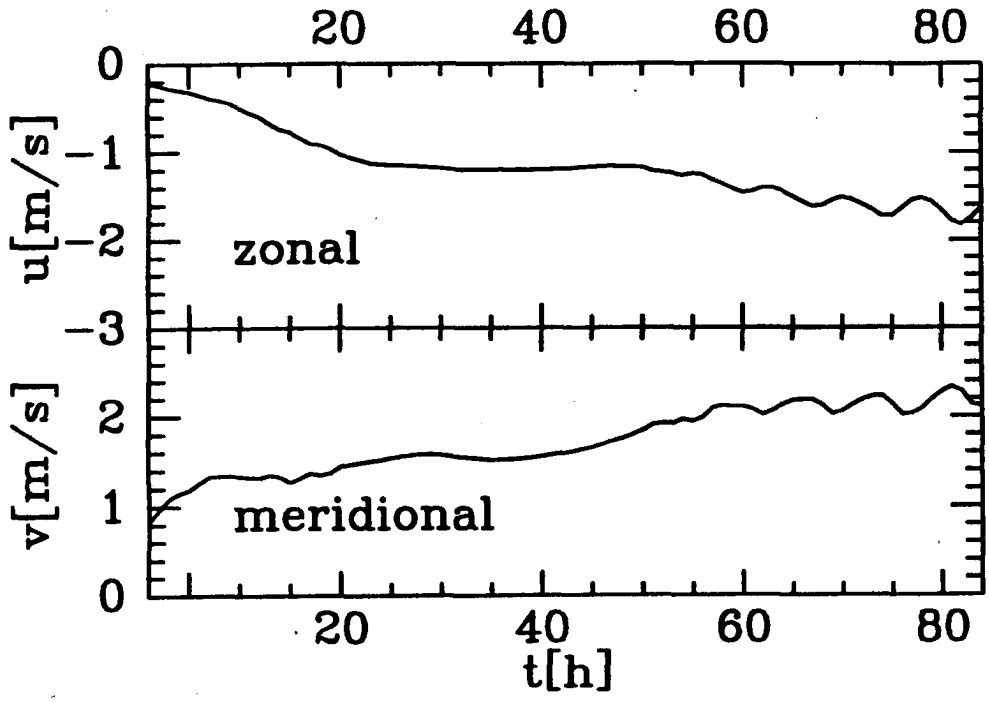

Figure 3.7: Vortex velocity (12 h running average) in experiment βD0.

the β effect is largely responsible for propagation. They based their conclusion on the fact that many characteristics of the observed propagation (e. g. prevailing north-west direction, dependence on intensity of a cyclone, etc.) agree with the behavior of a vortex moving on the β-plane. On the other hand, Gray (1991) interprets the difference between the average steering flow and cyclone movement as an effect of the environmental wind structure which is largely independent of the cyclone circulation. The results of this section indicate that although baroclinic effects modify the motion caused by the earth's vorticity advection, a baroclinic vortex on the β-plane moves toward northwest as predicted by barotropic models. In the next section and following chapters we will examine the effects which depend on the baroclinic structure of the hurricane. We will determine which of these effects can cause the vortex propagation comparable with that induced by the β effect.

3.2 Baroclinic vortex in a vertically sheared flow

The interaction between two vortices on a plane is quite well known (Fujiwhara effect). Multi-level models of point vortices suggest that vortices can also interact in the vertical direction. Such vortices, if placed along a tilted axis, can propagate in the direction perpendicular to the steering flow (Gray, 1991). We hypothesize that a similar mechanism can cause propagation of a tilted baroclinic vortex. Fig. 3.8 presents a conceptual model of such an interaction for a vortex on the f-plane. In this case, the tilting of the vortex is caused by vertically sheared environmental flow. When a vortex moves within a uniform steering flow on an f-plane, the axis of the vortex remains vertical. In this case the momentum transfer between the layers does not introduce asymmetries, and the vortex moves with the environmental flow. In a vertically sheared flow, the center of the upper-level anticyclone becomes displaced relative to the center of the lower-level cyclone. Exchange of momentum between the upper and lower level leads to the development of an asymmetric flow whereby a vortex gains a motion component perpendicular to the steering. The direction of this motion component depends on the direction of the shear. In westerly shear the vortex gains a northward component; in easterly shear, a southward component of vortex motion develops. A similar mechanism was recently used by Wu and Emanuel (1991) to explain the propagation of vortices in a two layer, quasi-geostrophic model.

Even though the development of tropical cyclones is favored by the situation with the minimum vertical shear, the tilting of the cyclones caused by vertically sheared flow has been observed (Huntley and Diercks, 1981). The tilting of tropical cyclones usually occurs in developing and dissipating stages. The tilt in the dissipating stage is often connected with westerly shear as the northward moving cyclone encounters upper-level westerlies.

To study the effect of vertical shear on vortex motion we calculate the movement of the baroclinic vortex in the westerly and easterly sheared flow (experiments WF and EF respectively). The model is initialized with the vortex obtained from the symmetric version of the model (Fig. 3.1) and a horizontally uniform, vertically sheared flow. The vertical shear in the experiment has to satisfy two conditions.

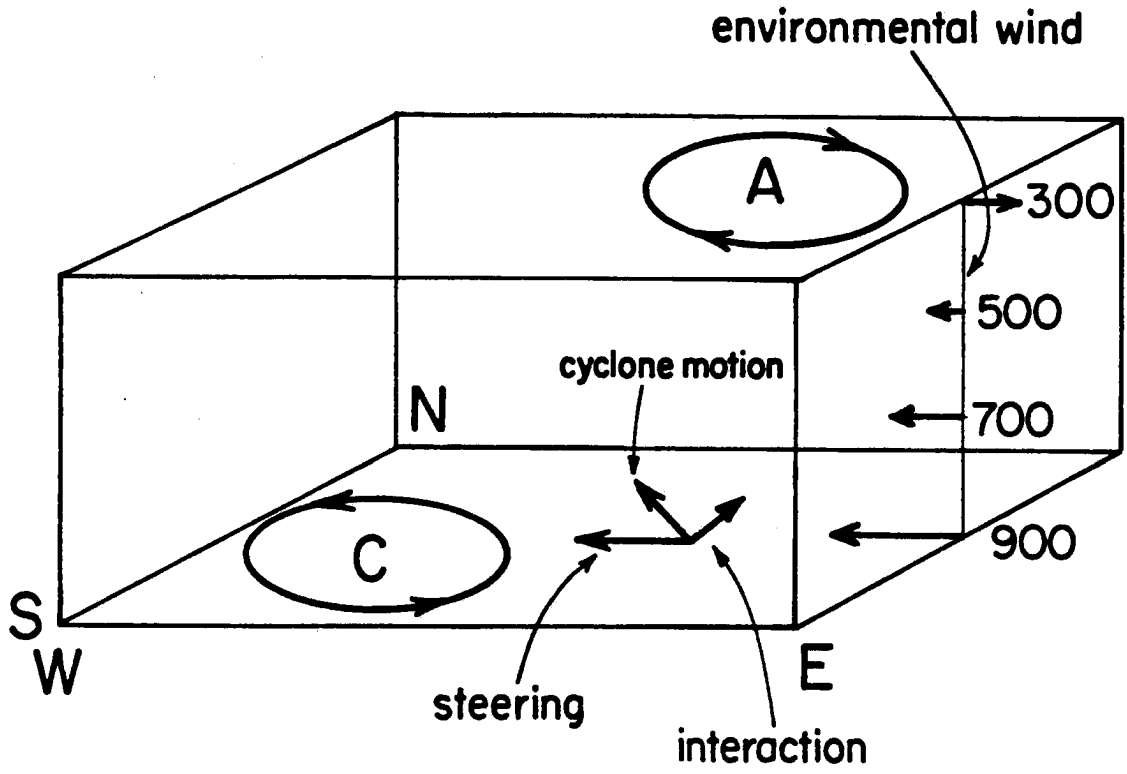

Figure 3.8: Idealized scheme for interaction between upper and lower layers of a tropical cyclone.

- The vertical shear has to be relatively small. It is a well known fact that large vertical shear inhibits the development or even destroys the vortex. The "resistance" of the hurricane to the vertical shear depends on many factors. Observations show that hurricanes developing over warmer water can develop within more strongly sheared flow that those developing over a relatively cooler ocean. The phase speed of propagation of the upper-level disturbance relative to lower-level disturbance is also important (Tuleya and Kurihara, 1981). However, tropical cyclones can usually withstand shears of 20 knots (9 ms^{-1})/600mb (Mark DeMaria - personal communication).

- The gradient of potential vorticity associated with the sheared flow has to be small. Even though there is no absolute vorticity gradient, the horizontal gradient of temperature resulting from thermal wind balance, causes a difference in stability and therefore creates a gradient of potential vorticity. If this gradient is large, the effects observed in a numerical model result not from the interaction between upper and lower levels of the cyclone but from the advection of environmental vorticity, analogous to the β effect (Shapiro, 1991).

The flow used in our experiments satisfies both these conditions. The flow varies linearly with σ. The magnitude of the shear is in both experiments the same and equal to $1.6ms^{-1}$/200mb. The wind at the lowest level is $-1.5ms^{-1}$ for the easterly shear case and $-3ms^{-1}$ for the westerly shear case. The magnitude of the potential vorticity gradient in the environmental flow is an order of magnitude smaller than that associated with the earth's vorticity gradient. The initial meridional potential vorticity gradient for the westerly shear case is equal to $.51 \times 10^{-6}km^{-1}$ for potential vorticity calculated on f-plane and to $.72 \times 10^{-5}km^{-1}$ if calculation of potential vorticity includes planetary vorticity gradient.

Shapiro (1991) has shown that the speed of motion caused by advection of the environmental potential vorticity is roughly proportional to the patential vorticity gradient. Therefore, if an effect on vortex motion observed in expariments of an f-plane is comparable with the β effect, we can expect that it results from the interaction between the hurricane's layers and not environmental potential vorticity advection.

The model was integrated for three days. For the westerly sheared flow (WF), the upper-level potential vorticity minimum after 24 hours moves about 550 km to the east relative to the vortex center (Fig. 3.10). After 72 hours (not shown) potential vorticity minimum weakens and moves slightly farther toward the east. In addition, high potential vorticity air is advected from below, creating a potential vorticity maximum above the low-level vortex center. At the lower levels we can observe the advection of environmental potential vorticity by the vortex circulation. We have to remember, however, that the gradient of environmental potential vorticity in this case is very small (Fig. 3.9). According to Gray (1991), the flow within a small radii (about 200 km) is the best indicator of the vortex movement. Fig. 3.11 shows the $s = 1$ Fourier component of the flow near the vortex center for the westerly shear experiment after 40 hours of integration. Even though initially the asymmetric flow was strictly in the east-west direction, after 40 hours a northward component of the flow is present at all levels. The northward component of the flow averaged over the circle with 200 km radius increases with height from .12ms^{-1} at 900 mb to 1.7ms^{-1} at 300 mb. The vertical (900 mb-300 mb) average is .8ms^{-1}. For the easterly shear (not shown), the situation is similar except that the upper-level potential vorticity minimum moves westward relative to the low-level vortex center. The flow near the vortex center acquires a southward component with a 900mb–300mb average of .7ms^{-1}.

Fig. 3.12 shows the trajectories of the vortices in an easterly and westerly shear during three days of integration. The zonal component of the movement is due to the presence of environmental flow. At the beginning of the integration, the vortices move with the low-level, easterly flow. After some time, we can see the effect of mixing of momentum by the secondary circulation. The zonal velocity of the vortex in easterly shear increases with time, while the vortex moving in westerly shear slows down and eventually recurves. The meridional component of motion is caused by the interaction with the upper layers. As expected from our conceptual model, the vortex in westerly shear moves toward the north and the vortex in easterly shear moves toward south. The speed of the movement (about 1m/s at 48 h) agrees quite well with the asymmetric component of the flow near

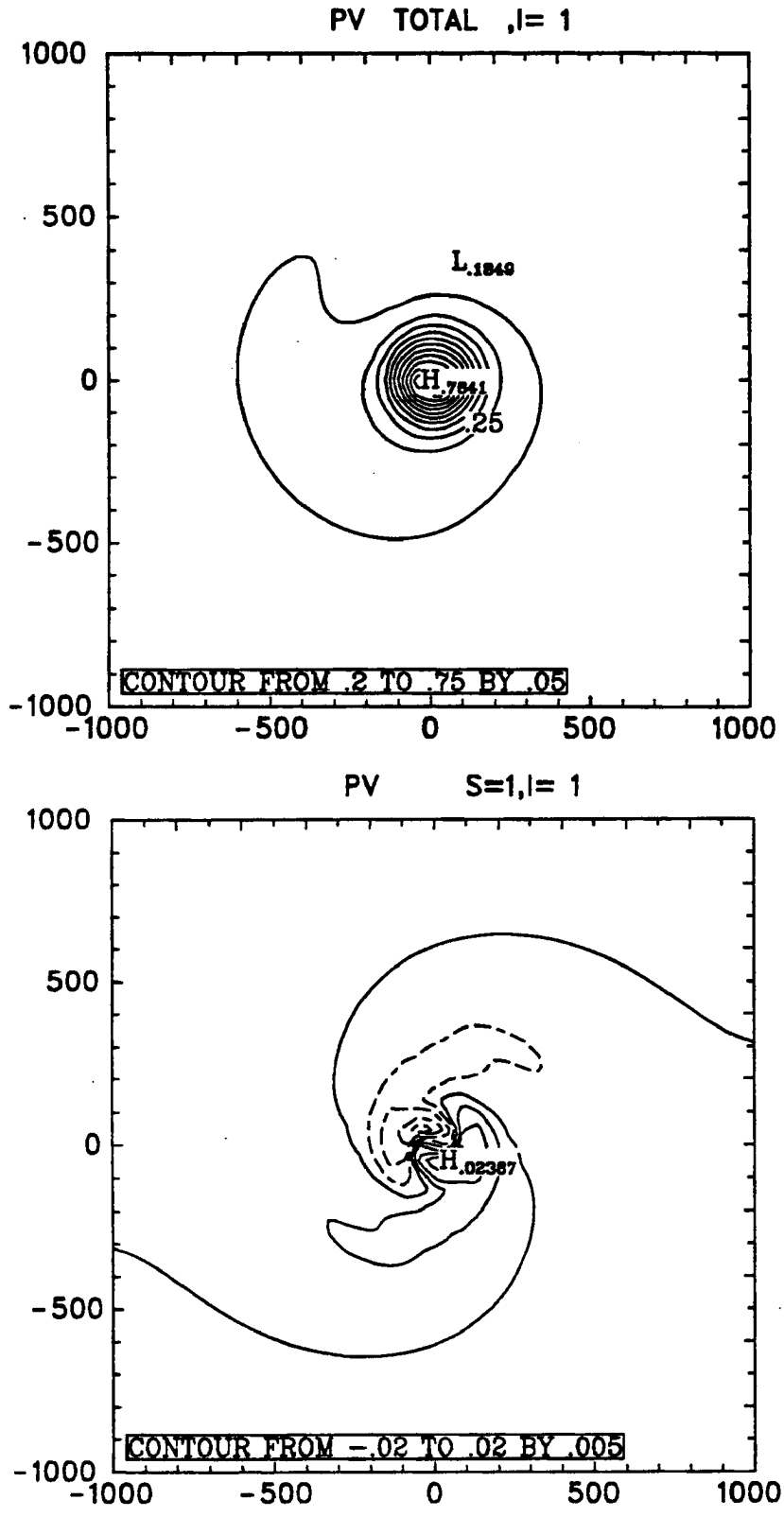

Figure 3.9: Potential vorticity at 800 mb in experiment WF (westerly shear) after 24 hours of integration.

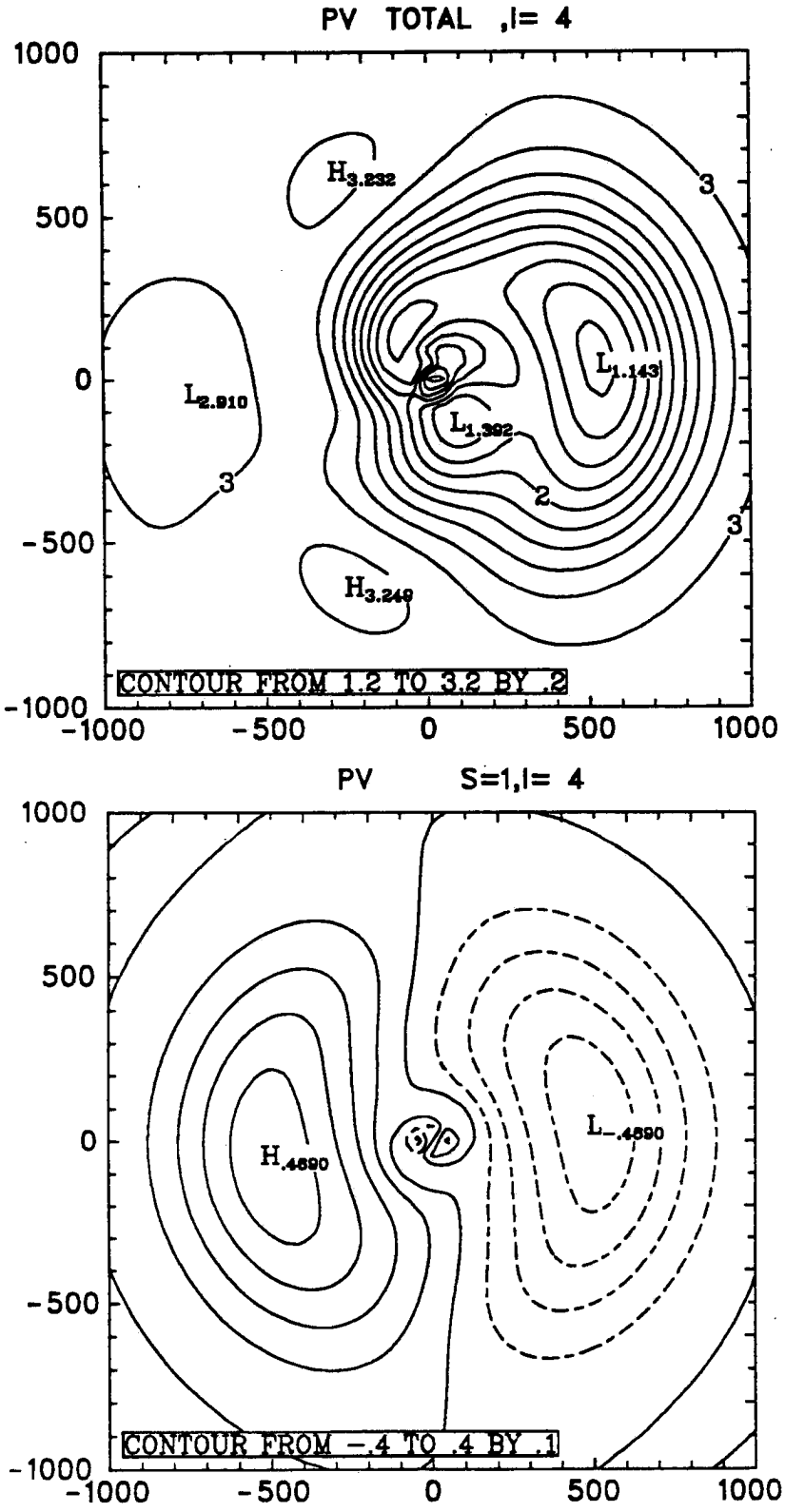

Figure 3.10: Potential vorticity at 200 mb in experiment WF (westerly shear) after 24 hours of integration.

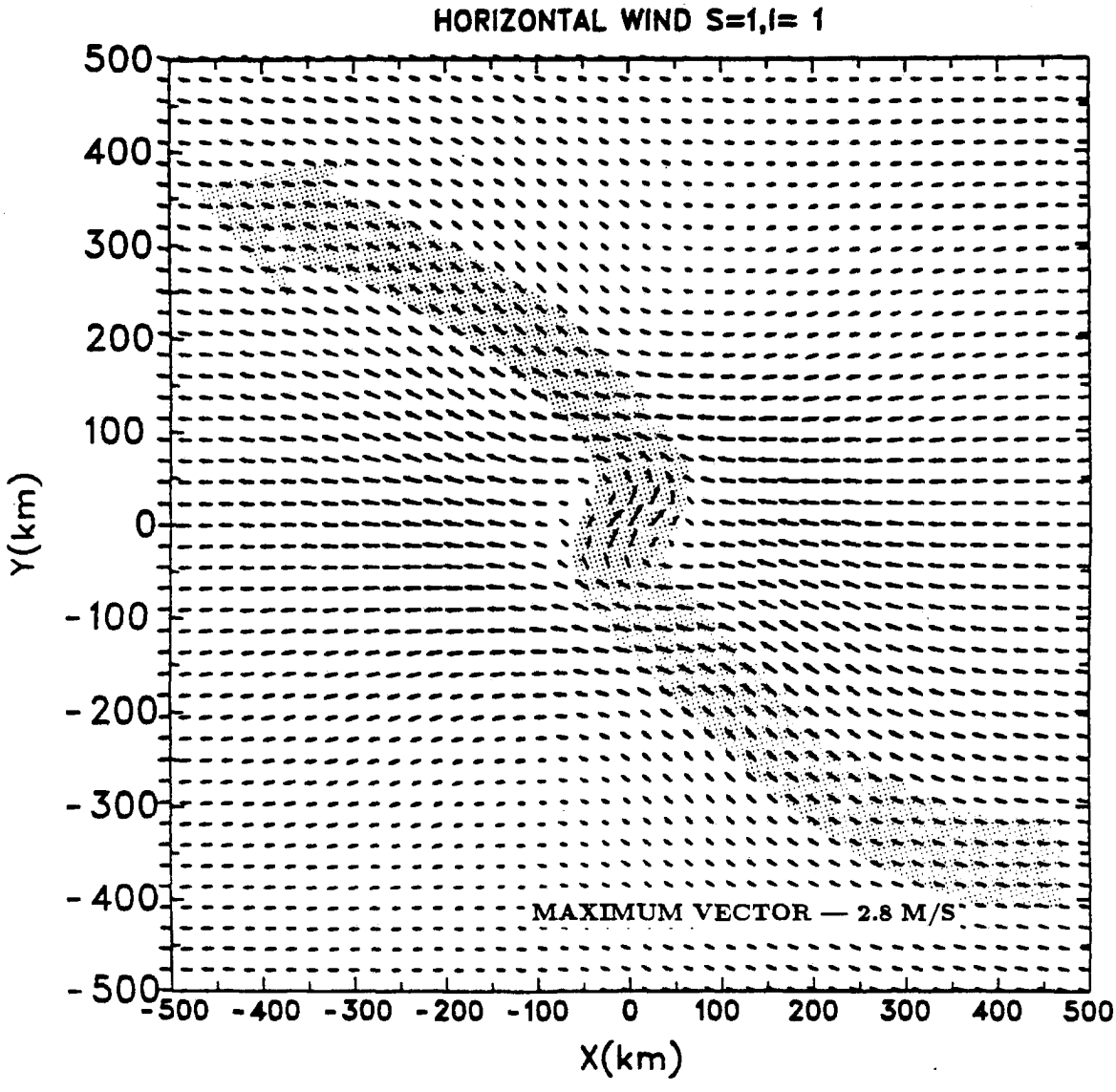

Figure 3.11: a) Asymmetric flow (s=1) at 900 mb in experiment WF after 40 hours of integration.

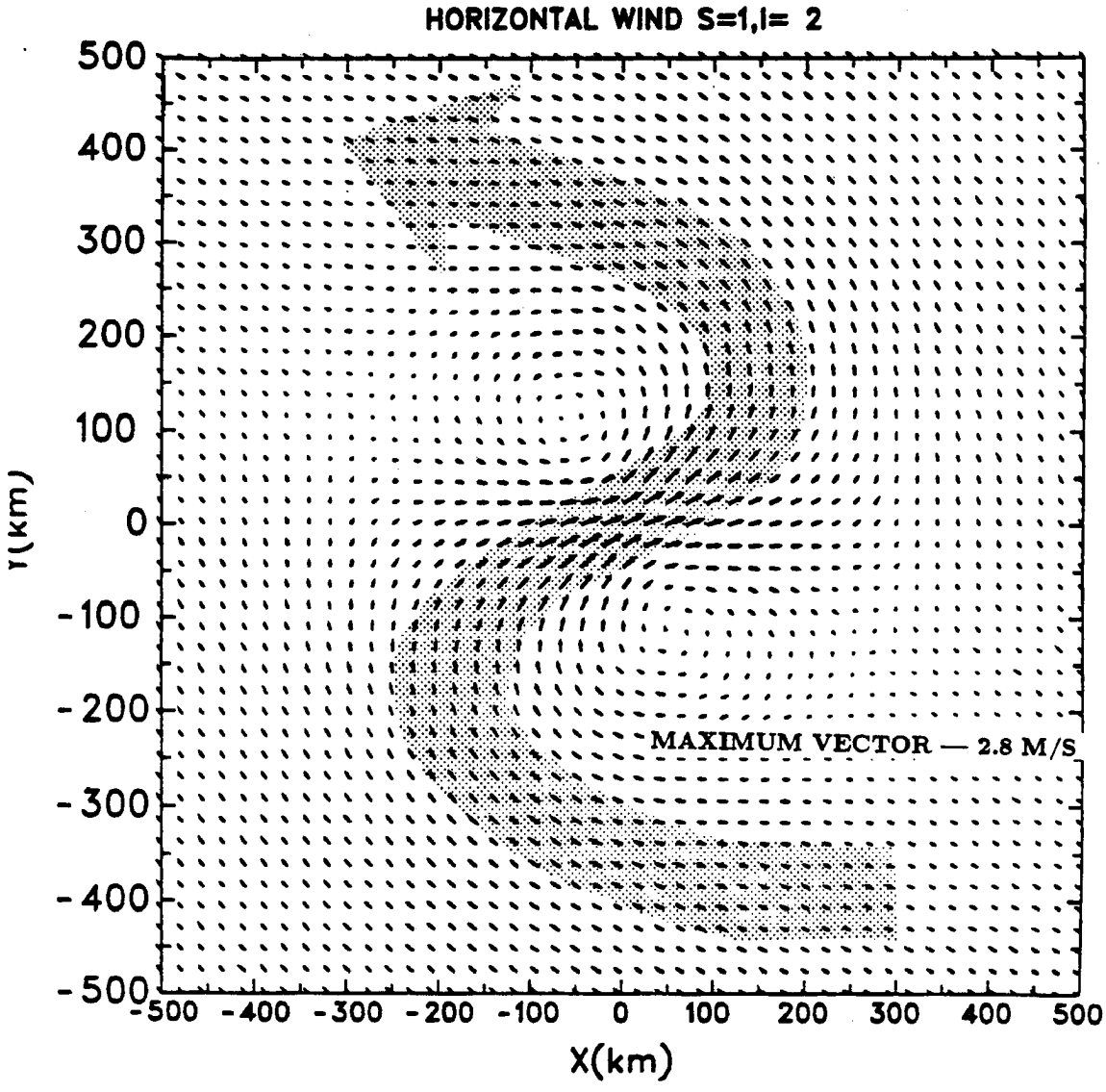

Figure 3.11: b) Asymmetric flow (s=1) at 700 mb in experiment WF after 40 hours of integration.

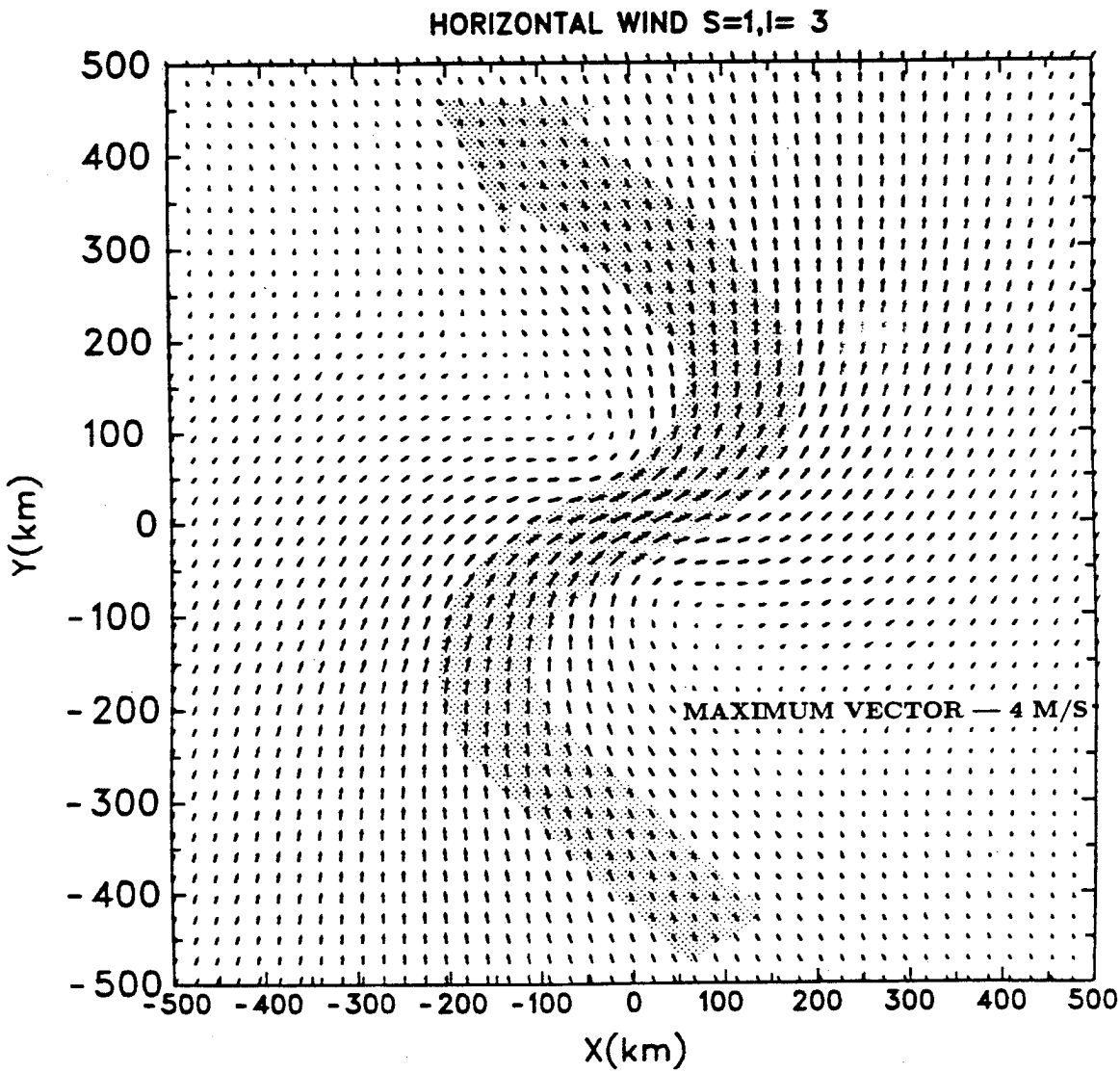

Figure 3.11: c) Asymmetric flow (s=1) at 500 mb in experiment WF after 40 hours of integration.

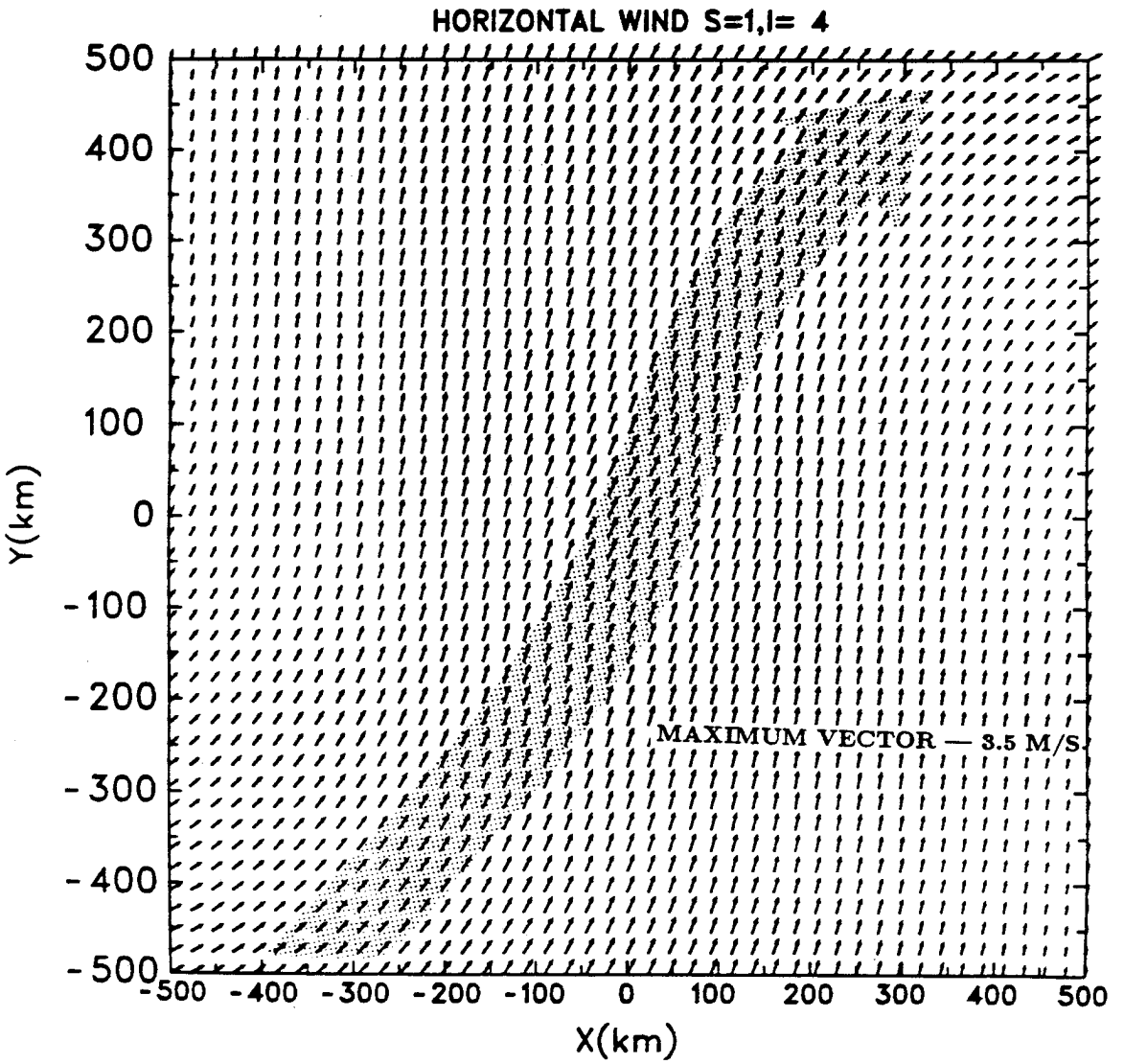

Figure 3.11: d) Asymmetric flow (s=1) at 300 mb in experiment WF after 40 hours of integration.

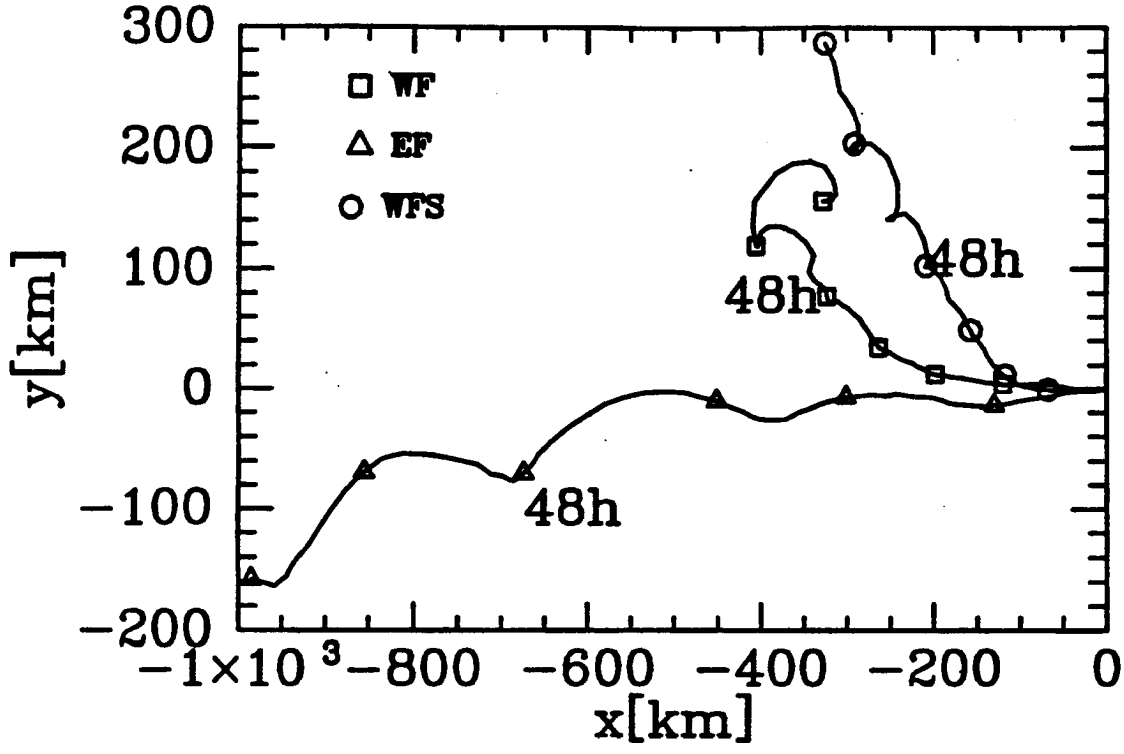

Figure 3.12: Trajectory of the baroclinic vortices on the f-plane in westerly shear (WF and WFS) and easterly shear (EF) during 3 days of model intergration.

the vortex center. The difference in meridional position between the vortex in easterly an westerly shear after 72 hours of integration is about 350 kilometers. The same vortex on a β plane without meridional flow progresses about 450 km toward north. Therefore we can conclude that the displacement due to the interaction on an f-plane is comparable with that caused by the β effect.

We now examine the motion of the vortex stronger than that used in WF and EF. The vortex in this experiment (WFS) has 30ms^{-1} initial tangential wind speed and a diabatic heating is about 1.5 times stronger than that used in WF. The environmental wind field is the same as in EF. As can be seen from Fig. 3.12, the stronger vortex moves slower toward the west due to increased mixing between the layers, but the northward component of the speed is about 1.5 times larger than in EF.

The propagation of vortices in experiments WF and EF is in the opposite direction of that resulting from potential vorticity advection in Shapiro (1991) . Also, for the environmental wind profile used in out experiments, 0 initial potential vorticity for westerly shear increases with latitude while in Shapiro (1991) it decreases with latitude. The opposite is true in the easterly shear case. This situation can be explained by the fact that the potential vorticity gradient depends not only on the direction of the shear but also on the shape of the wind profile. Let's consider the thermal wind equation:

$$\frac{\partial u_g}{\partial p} = \frac{R}{fp}\frac{\partial T}{\partial y} = \frac{R}{fp}\left(\frac{p}{p_0}\right)^{R/cp}\frac{\partial \theta}{\partial y}. \tag{3.1}$$

Since in the absence of absolute vorticity gradient, potential vorticity is approximately proportional to vertical stability, we differentiate 3.1 with respect to p to obtain

$$\frac{\partial}{\partial y}\left(\frac{\partial \theta}{\partial p}\right) = \frac{f}{R}\left(\frac{p_s}{p}\right)^{R/cp}\left[\frac{\partial^2 u}{\partial p^2}p + \frac{\partial u}{\partial p}(1 - R/cp)\right]. \tag{3.2}$$

In the case of linear westerly shear, stability $\partial\theta/\partial z \sim -\partial\theta/\partial p$ increases toward the north. Therefore, if absolute vorticity is constant, potential vorticity increases toward the north. However, when the wind does not change linearly with pressure, the second derivative in (3.2) may become important. When the shear is placed in the upper layers, the temperature gradient in the upper layers becomes larger than in lower layers and for westerly shear

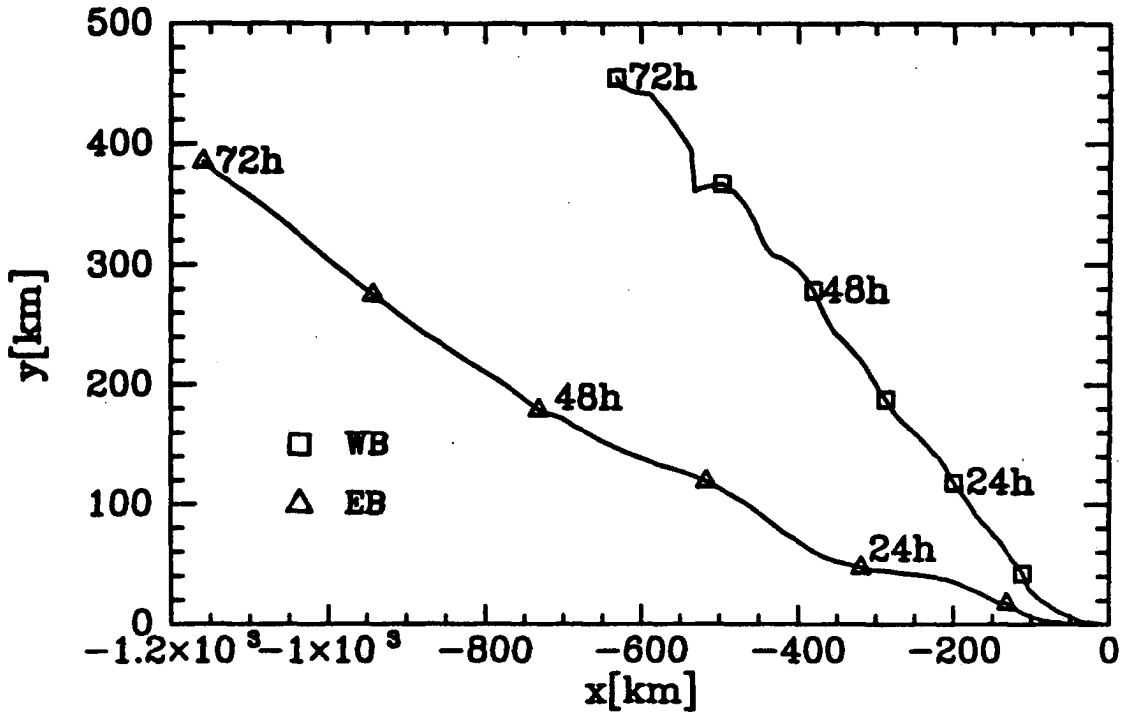

Figure 3.13: Trajectory of the baroclinic vortices on the β-plane, in experiments WB and EB during 3 days of model intergration.

the stability decreases toward the north, as in the case described in Shapiro (1991). As shown by Shapiro, vortex motion caused by the advection of an environmental vorticity gradient is proportional to the magnitude of the gradient. It also depends on the depth of the layer in which the gradient is present. If the shear is confined to a very thin layer, the potential vorticity gradient occurs only in a thin layer and its effect on vortex motion is small. Therefore, without careful analysis of the environmental wind profile and the vortex structure, it is difficult to predict the direction and speed of vortex propagation.

In the next two experiments (WB, EB) we introduce the effect of the earth's vorticity advection. We again use zonal environmental flow with easterly and westerly shear so that earth's vorticity gradient is perpendicular to the flow. The trajectory of vortices during three days of integration is shown in Fig. 3.13. As expected, both vortices now move toward the north, with the vortex in westerly shear moving faster in meridional direction than the one in easterly shear. However, the motion is not just a superposition of movements due to the β-effect with that caused by the shear flow. The meridional difference

between the positions of the vortices is now smaller than on the f-plane (100 km instead of 350 km after 3 days). This effect can be explained by examining the corresponding potential vorticity fields (Fig. 3.14). The upper-level anticyclone is not only advected zonally by the sheared flow, but also moves toward the south due to the the earth's vorticity advection. Therefore, enhancement of the flow resulting from the interaction occurs in the southwestern and southeastern parts of the vortex. The asymmetric flow caused by the interaction induces the westerly component while the meridional components become smaller. This is in contrast to the situation described by Shapiro (1991) where the effects of shear-induced potential vorticity gradient and the β effect were nearly additive. In the case of motion caused by interaction between upper and lower-level vorticity anomalies, the direction of the propagation depends on the position of these anomalies relative to each other which can be affected by the background potential vorticity gradient.

Another factor which can influence vortex movement is the horizontal distribution of diabatic heating. In all the experiments described in this chapter, the diabatic heating is symmetric relative to the vortex center. In reality, introduction of the sheared flow causes an asymmetry in the vertical velocity. Even though the azimuthally averaged vertical motion is similar in both experiments (Fig.3.15) the asymmetric components of vertical velocity are very different.

A vortex moving toward the west, in easterly shear moves faster than the low-level flow, resulting in upward motion ahead of the vortex. The opposite is true for a vortex in westerly shear (Fig. 3.16). The asymmetry of vertical motion can cause asymmetries of convective heating. The effect of the horizontal distribution of convective heating will be examined in the next chapter.

3.3 Summary

In this chapter we investigated the effects of interaction between upper and lower-level potential vorticity anomalies on the motion of a baroclinic vortex. The summary of the numerical experiments included in this chapter is show in Table 3.1.

When the vortex is tilted, interaction between the anomalies leads to propagation relative to the steering flow. On a β-plane, with no environmental flow, the vortex is

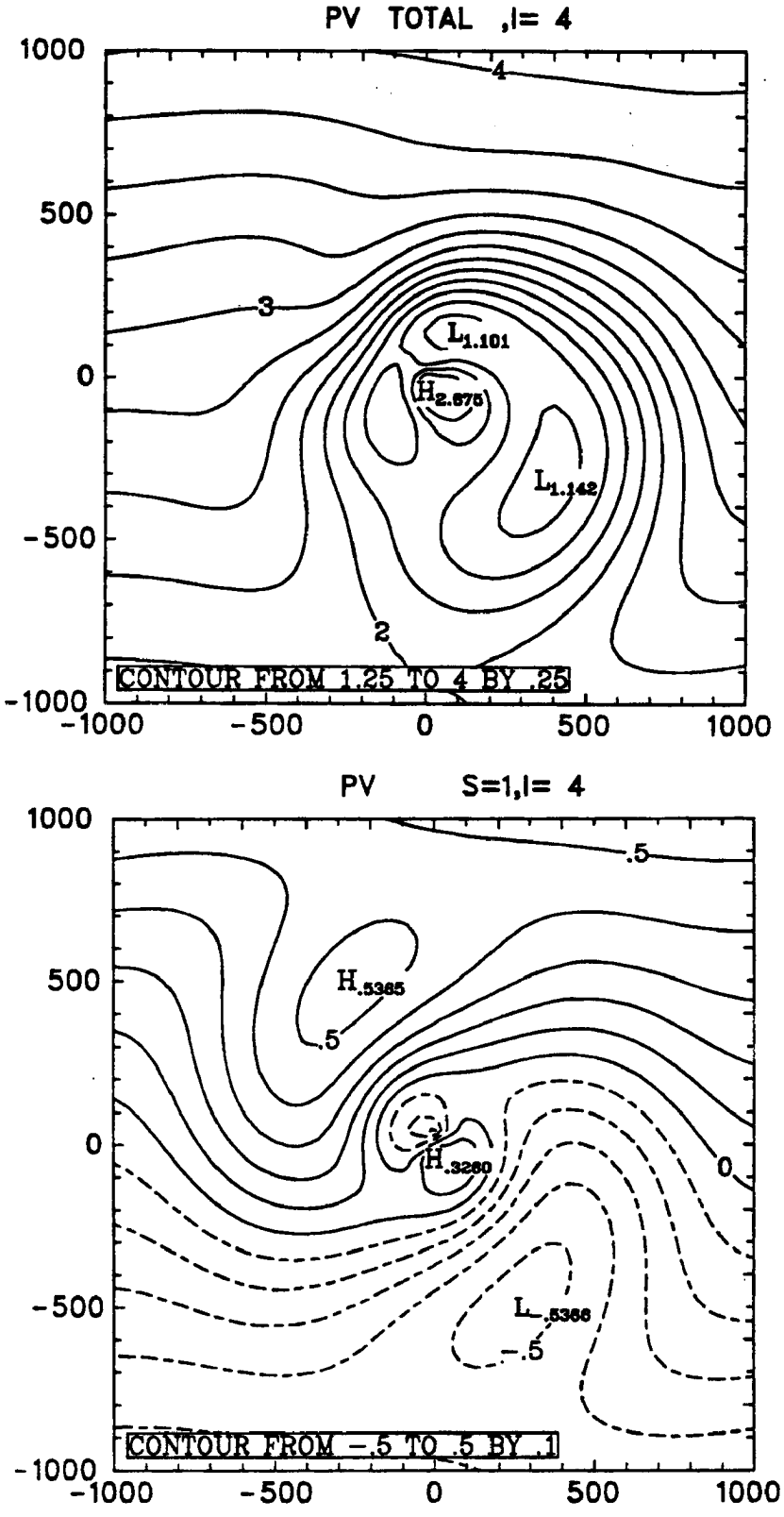

Figure 3.14: Potential vorticity at 200 mb in experiment WB, after 24 hours of integration.

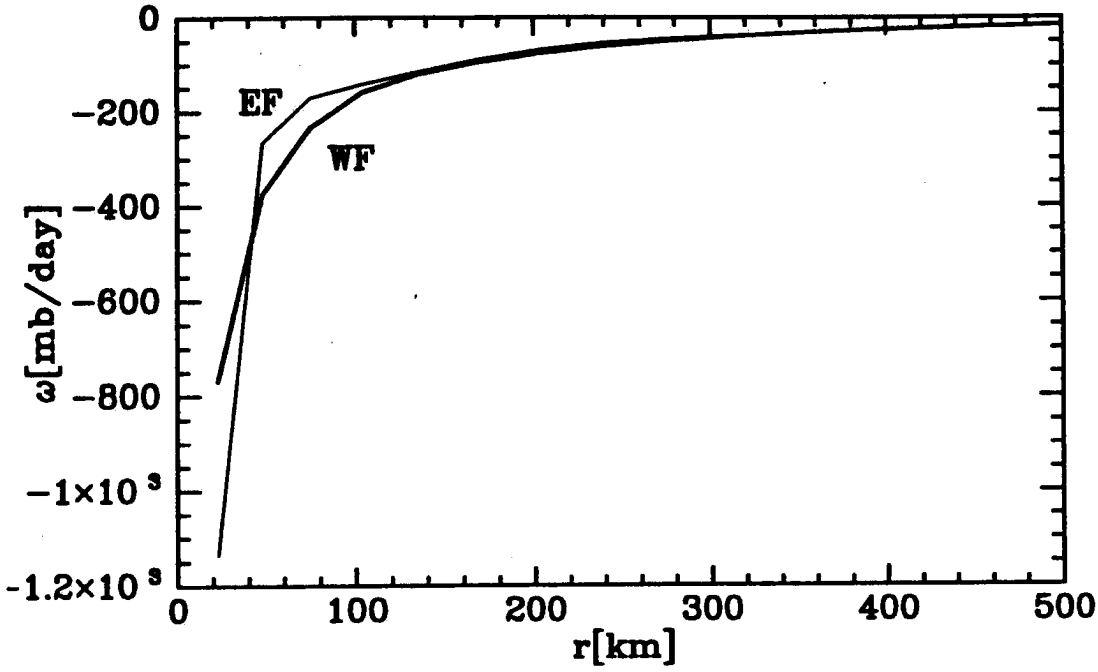

Figure 3.15: The vertical velocity ω (in mb /day) at 700 mb, averaged over the circle with the radius r centered on the vortex center. Thick line — experiment WF, thin line — experiment WE.

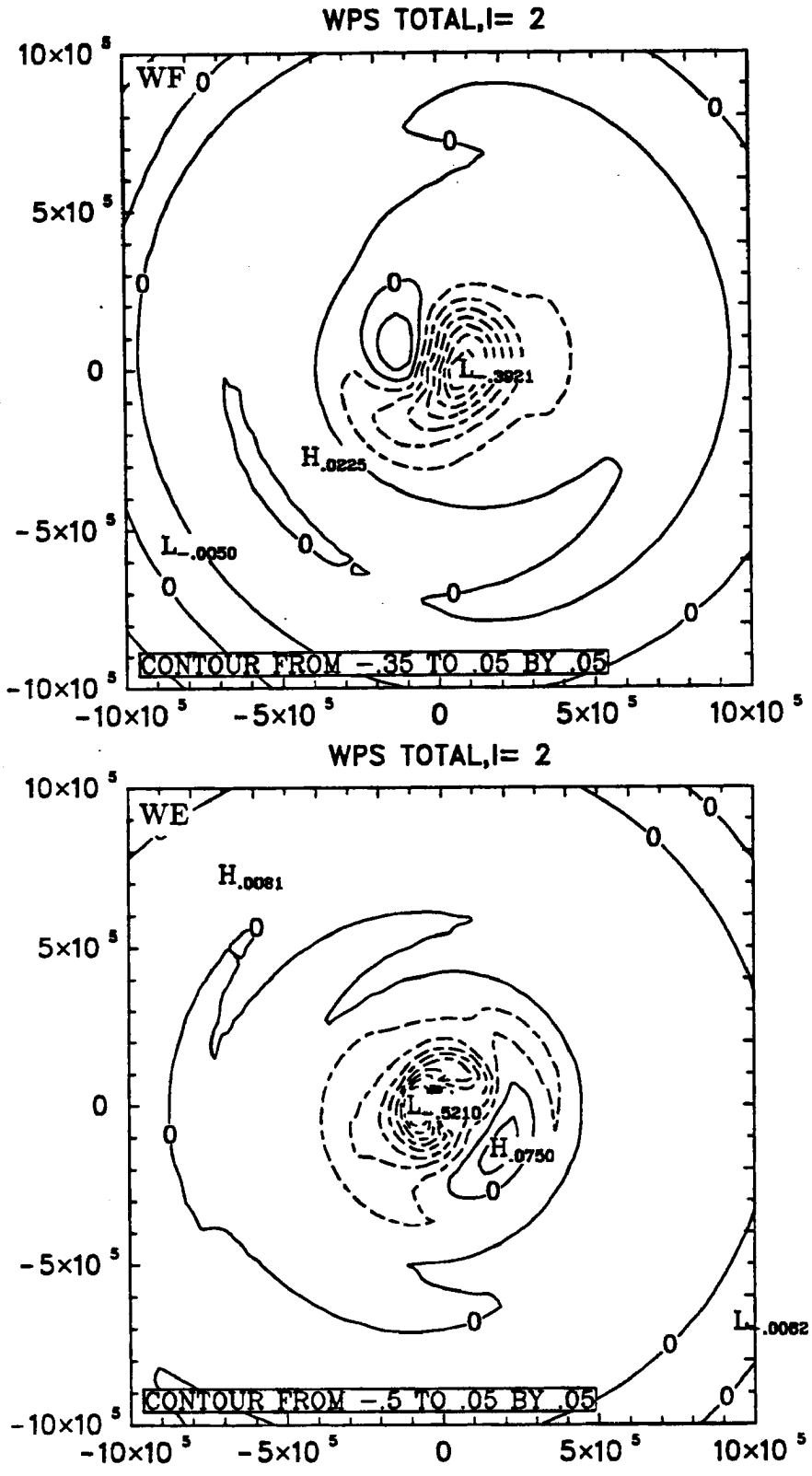

Figure 3.16: Vertical velocity in σ coordinates ($p_s\dot{\sigma}$) at 700 mb in experiments WF and WE. The maximum upward velocity in experiments WF corresponds to ω=-1200 mb/day, the maximum upward velocity in WE corresponds to ω=-2000mb/day.

slightly tilted toward the south and the interaction between the layers reduces the westward movement of the vortex.

The vortex tilting can also occur due to the vertical shear in the environmental wind. On an f-plane, the interaction between the layers causes the northward movement of the vortex in westerly linear shear, and southward movement in easterly linear shear, with a meridional velocity of about 1 m/s. This velocity increases with increasing vortex intensity and vertical motion. The magnitude of the meridional vortex velocity caused by this effect is comparable with the motion resulting from advection of planetary vorticity.

Since direction of motion depends on the relative position of potential vorticity anomalies, the presence of a background potential vorticity gradient changes the direction of motion caused by the interaction between the layers.

Table 3.1: Summary of experiments in Chapter III

Experiment	vertical coupling	environmental flow	vortex velocity [m/s]
$\beta D0$, βplane	diabatic heating	-	$u_v = -0.91$,$v_v = 1.54$
βNI, β-plane	-	-	$u_v = -0.99$,$v_v = 1.38$
$\beta D20$, β-plane	diab. heat. + vert. diff.	-	$u_v = -0.83$,$v_v = 1.49$
WF, f-plane	diab. heat.	westerly shear	$u_v = -1.33$,$v_v = 0.61$
WFS, f-plane	stronger diab. heat.	westerly shear	$u_v = -1.14$,$v_v = 1.14$
EF, f-plane	diab. heat.	easterly shear	$u_v = -3.83$,$v_v = -0.61$
Wβ, β-plane	diab. heat.	westerly shear	$u_v = -2.36$,$v_v = 1.74$
Eβ, β-plane	diab. heat.	easterly shear	$u_v = -4.2$,$v_v = 1.44$

Chapter 4

INFLUENCE OF HORIZONTAL DISTRIBUTION OF CONVECTIVE HEATING ON VORTEX MOTION

Although symmetric convection is favorable for tropical storm development, satellite pictures of hurricanes often reveal asymmetric convection patterns. The connection between convective asymmetry and the direction of cyclone motion has often been observed (Lajoie, 1976; Fett and Brand, 1975). Lajoie (1976) proposed a short-term prediction scheme for tropical cyclone motion based on satellite observations of convective features in tropical cyclones. He determined that tropical cyclones usually turn toward the most developed cumulonimbus cluster and never turn into the cumulonimbus-free sector. Fett and Brand (1975) also noticed that the rotation of asymmetric major cloud features in a tropical cyclone indicates future change in a cyclone's direction of motion.

Even though it is possible to build a prediction scheme for short-term hurricane motion based on satellite pictures of cyclone convection, the correlation between TC motion and the convection distribution does not explain the role of the convective heating distribution in motion change. As suggested by Lajoie (1986), asymmetric distributions of convection can be caused by the interaction between the cyclone circulation and the environmental flow. Therefore, the change in the direction of storm motion can result from heating as well as dynamical effects, which only manifest themselves as changes in cloudiness.

However, in some cases where the convective asymmetries seem to be of thermodynamic (presence of warm, moist air), rather than dynamic (convergence) origin, the connection between convective asymmetry and TC motion has been found. The studies of climatology of convective asymmetries in tropical cyclones (Shoemaker, 1989; Hallin,

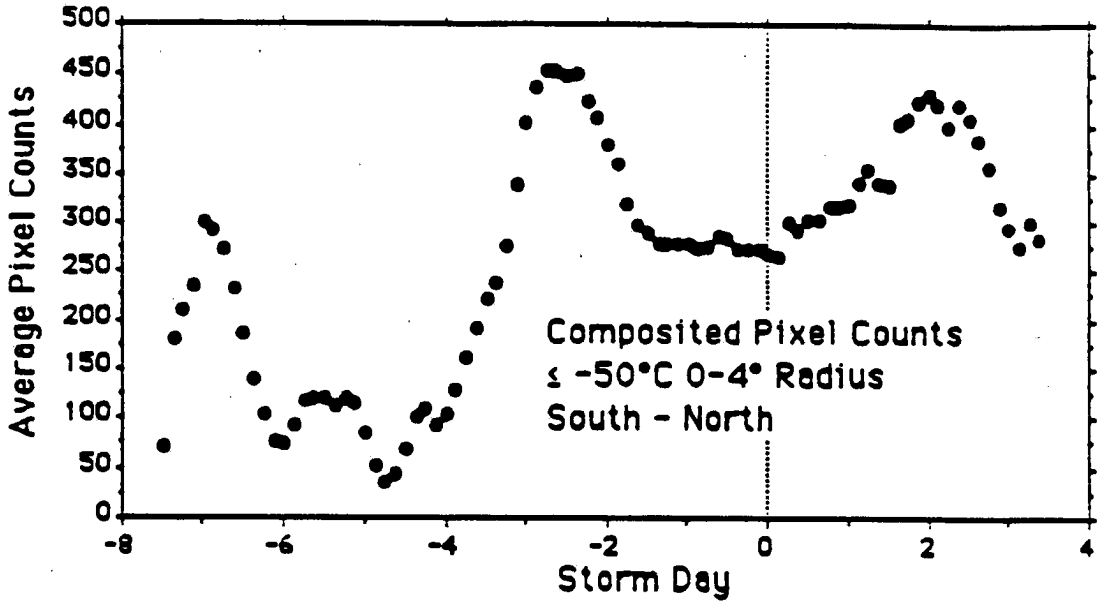

Figure 4.1: The composite south–north asymmetry of deep convection (From Shoemaker, 1989)

1991) indicate that even though for a single tropical cyclone the distribution of asymmetric convection varies, the composite cyclones show more convective activity in the southern quadrant (Fig. 4.1). Shoemaker also argued that the eastern quadrant has more convection due to advection of equatorial air by the cyclone circulation. However, the east-west asymmetry is much less obvious than the south-north asymmetry, and Hallin (1991), using slightly different methodology, found more convective activity in the western sector. Hallin also studied the connection between convective asymmetries and TC motion and found that greater asymmetries correspond to faster eastward motion (Fig. 4.2).

The studies of the sea surface temperatures' (SST) influence on tropical cyclone motion provide additional insight into how convective heating affects cyclone motion, since in these studies the convective asymmetries are caused by asymmetry in surface fluxes, not by dynamic processes. The numerical model of Chang and Madala (1980) shows that when the SST gradient is perpendicular to the mean environmental flow, tropical cyclones tend to move into the region of warmer SSTs. Ginis' (1991) coupled model of the

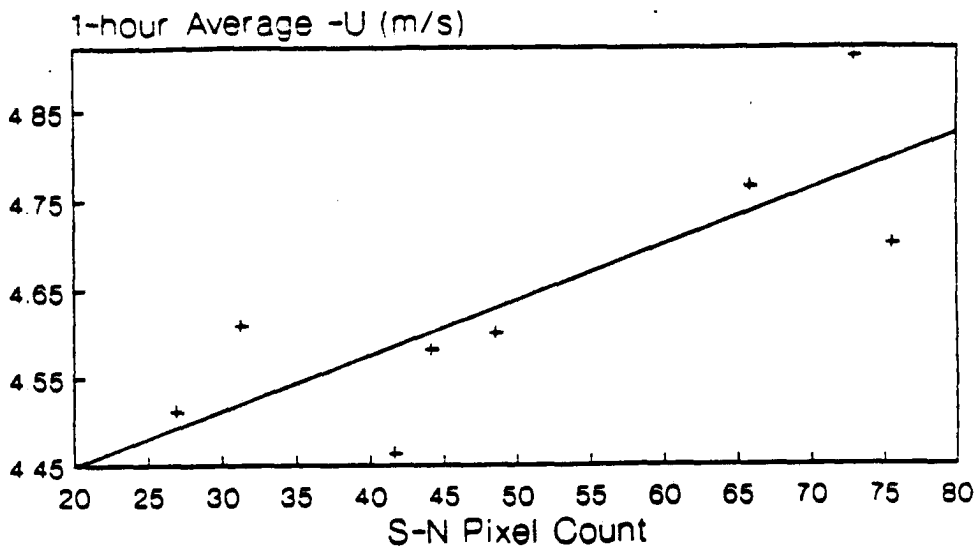

Figure 4.2: The correlation between the north–south asymmetry of deep convection and the zonal speed of cyclones' motion (From Hallin, 1991).

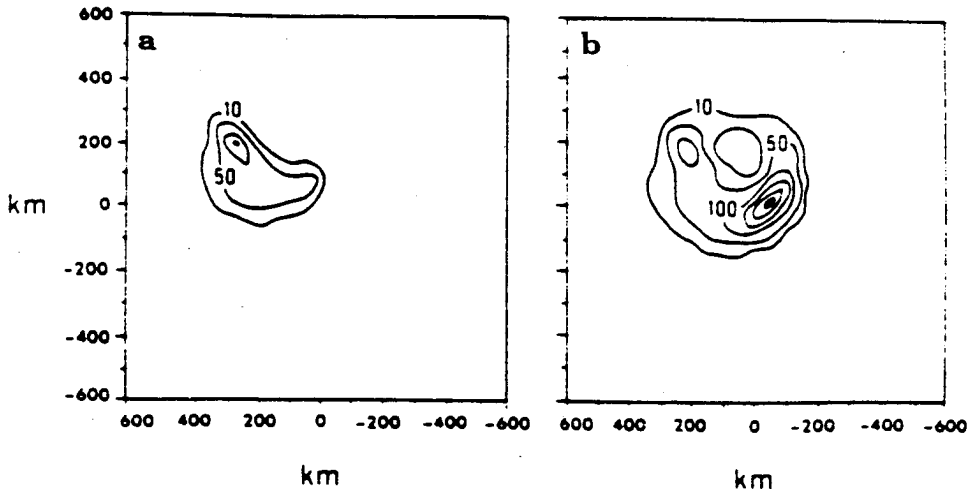

Figure 4.3: Precipitation pattern (mm/day) in the coupled (a) and atmosphere-only (b) model (From Ginis, 1991).

atmosphere-ocean system shows that tropical cyclones move differently in the coupled and atmosphere-only model. In the coupled model, the upwelling caused by a cyclone circulation reduces SST behind and to the right of a cyclone track. The decrease of SST causes a change in the precipitation pattern. Fig. 4.3 shows the precipitation for the coupled and atmosphere-only model for a cyclone moving in westerlies. The interaction with the ocean not only causes a decrease in precipitation and therefore in the intensity of the cyclone, but also the displacement of the precipitation maximum from the south-eastern quadrant into the north-western quadrant. As a result, the cyclone in the coupled model moves toward the north faster than the cyclone in the atmosphere-only model, even though the cyclone in the coupled model is less intense.

In this chapter we investigate the response of baroclinic vortex motion to asymmetries in convective heating. In all experiments described in this chapter, no environmental flow is present, so motion changes are caused solely by the presence of asymmetric heating. As in Chapter 3 the heating distribution is assumed *a priori*. The symmetric part of the convective heating is the same as in the experiments described in the previous chapter. The asymmetric part has $s = 1$ structure in azimuthal direction. The radial distribution

Table 4.1: List of experiments in Chapter IV

Experiment	A	RH[km]	RW[km]	α	
ACF1 (f-plane)	.2	100	30	45	steady heating
ACF2 (f-plane)	.8	100	30	45	steady heating
ACF3 (f-plane)	.2	400	30	45	steady heating
ACB1 (β-plane)	.2	500	150	90	steady heating
ACB2 (β-plane)	.2	500	150	77	steady heating
AOB1 (β-plane)	.2	500	150	77	oscillating heating ($T_O = 24$h)
ARF1 (f-plane)	.2	100	30	–	rotating heating ($T_R = 17$h)

is given by:

$$D_R = A \exp\left[-\left(\frac{r - R_H}{R_W}\right)^2\right], \tag{4.1}$$

where R_H is the radius of maximum heating, R_W (half-width of the Gaussian curve) is a measure of radial extent of a heated region, and A gives the value of maximum heating which is expressed as a fraction of the symmetric maximum heating. The orientation of maximum heating is measured by the angle α:

$$D_H = D_R \cos(\theta - \alpha). \tag{4.2}$$

where $\alpha = 0$ denotes the north. In addition, we consider two types of time dependency, either oscillation with the period T_O

$$D_H(t) = D_H(B + C \sin(2\pi t/T_O), \tag{4.3}$$

or rotation

$$D_H(t) = D_H \exp(i2\pi t/T_R), \tag{4.4}$$

where T_O and T_R are the periods of oscillation and rotation respectively, and the constants B and C determine what fraction of asymmetric heating oscillates in time. The vertical distribution of asymmetric heating is the same as the vertical distribution of symmetric heating. The summary of experiments described in this chapter is shown in Table 4.1. In all experiments we use the same initial vortex as in Chapter 3.

4.1 Steady asymmetries

In the experiments described in this section we study the effect of stationary convective asymmetries (with no change in amplitude or position relative to the moving cyclone) on the cyclone motion. First, we consider the asymmetry which could result from the movement of a vortex in vertically sheared flow. As shown in Chapter 3, for a vortex in westerly shear (experiment WF in the previous chapter) the vertical velocity field becomes asymmetric with upward motion east of the cyclone center (Fig.3.16), and the maximum at about 100 km from the center. Therefore we assume a similar horizontal distribution for the asymmetric diabatic heating. The heating maximum is centered at RH=100 km east of the vortex center ($\alpha = 45$). It is concentrated in a fairly narrow band with RW=30 km. As in experiment WF, the model is run on an f-plane. Since no environmental flow and no potential vorticity gradient are present, the vortex motion is caused only by the presence of the heating asymmetry. In the first experiment (ACF1) the amplitude of asymmetric diabatic heating is fairly small (A=0.2) and the vortex shows little movement. When the maximum of asymmetric heating is increased by a factor of four (experiment ACF2), the vortex begins to move toward the northeast (Fig. 4.5). The path is rather erratic and some rapid, small amplitude, cyclonic looping is present. Similar looping is sometimes reported in cyclones with a "double eye" structure (Muramatsu, 1986). As seen in Fig. 4.4, the diabatic heating in this case has two maxima — one at 100 km where the asymmetric heating is largest, and a smaller one at the vortex center.

The maximum displacement of the vortex during 3 days of integration is about 15 km to the east and 18 km to the north. The vortex turns westward after about two days of integration. We therefore conclude that the presence of asymmetric heating should not drastically change our results from those described in Chapter 3. Under the influence of heating asymmetry concentrated near the vortex center, the vortex moved rather slowly, and roughly in the direction of propagation resulting from vertical shear.

In his study of convective asymmetries in tropical cyclones, Hallin (1991) speculates that asymmetric outer convection induces asymmetry in the eye-wall convection by reducing the inflow of the moist, warm air. Asymmetries in eye-wall convection cause the

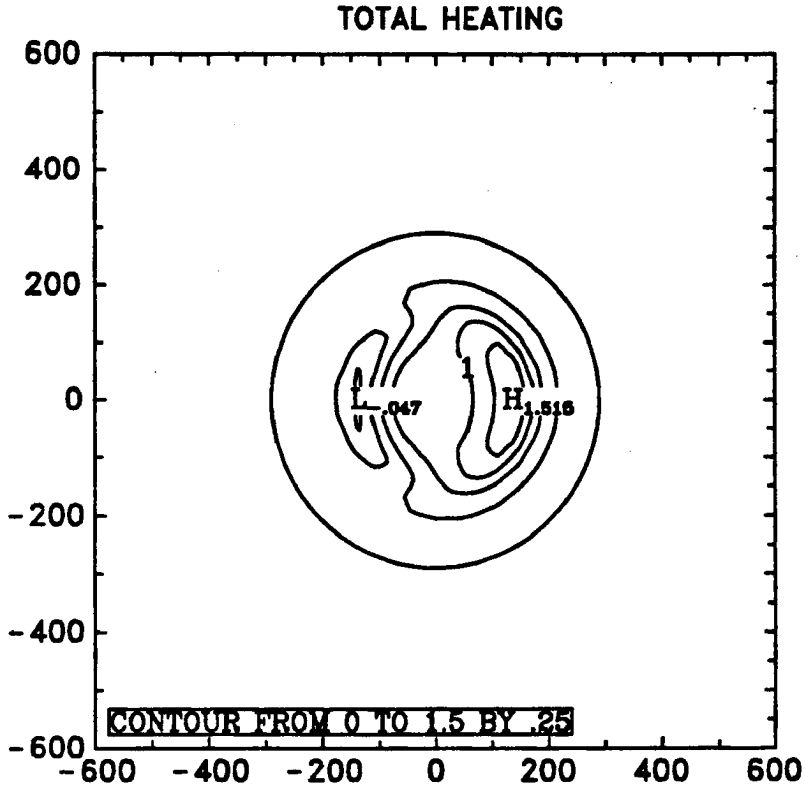

Figure 4.4: Diabatic heating in experiment ACF2

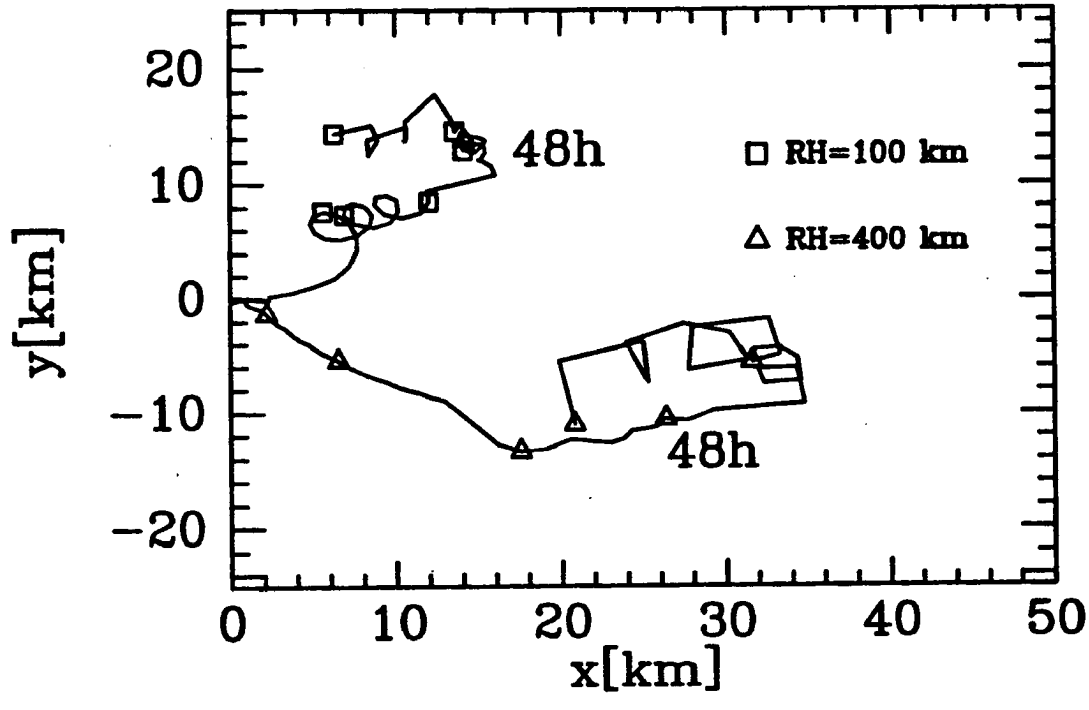

Figure 4.5: Vortex path on f-plane in experiments ACF2 and ACF3

wind asymmetries, which in turn contribute to vortex motion. Therefore an asymmetry localized at larger radius should cause the vortex to move in the opposite direction to a similar asymmetry in the eye-wall convection. In the next experiment (ACF3) we examine the case where asymmetric heating is located farther from the vortex center — at 400 km instead of 100 km. As in the previous experiment, RW=30 km. The amplitude of the heating function is four times smaller than in ACF2 (A=0.2), so that total heating east of the vortex center is the same as in the previous experiment. The path of the vortex for this experiment is shown in Fig. 4.5. In this case, the vortex moves towards the southeast with a displacement slightly greater than in ACF2. The fact that vortices in ACF2 and ACF3 move in opposite meridional directions agrees to some extent with Hallin's (1991) arguments on the effects of asymmetric heating on cyclone motion. However, even though the heating and cooling in ACF2 is concentrated in a small area where the vorticity is high and has a larger amplitude than heating asymmetry in ACF3, the asymmetric potential vorticity gradient near the vortex center in ACF2 is no larger than in ACF3 (Figs. 4.6) and 4.7), and the vortex moves slower when asymmetric heating is concentrated at smaller radii. This shows that the response of the vortex circulation to asymmetric heating is quite different than the response to symmetric heating. With symmetric heating the potential vorticity anomaly created by the presence of a diabatic heat source is larger for the source placed in the region with higher inertial stability. This is true for the tropical cyclones as well as other symmetric circulations (e.g., zonally symmetric Hadley circulation in Schubert et al., 1991). However, placing the asymmetric heating in the inertially stable region does not create large flow asymmetries. This result agrees with Carr and Williams' (1989) arguments on symmetrization of the flow in vortices with radial wind shear. Carr and Williams, using an analytical, barotropic model of a Rankine vortex, have shown that advection of asymmetric perturbations by radially shearing tangential mean flow destroys asymmetric perturbations. The damping is proportional to the magnitude of radial shear and the square of azimuthal wavenumber. Therefore, convective asymmetries in the hurricane eye-wall are unlikely to produce strong asymmetric circulation. Perturbations which maximize in the less stable area are damped at much slower rate. For example, potential

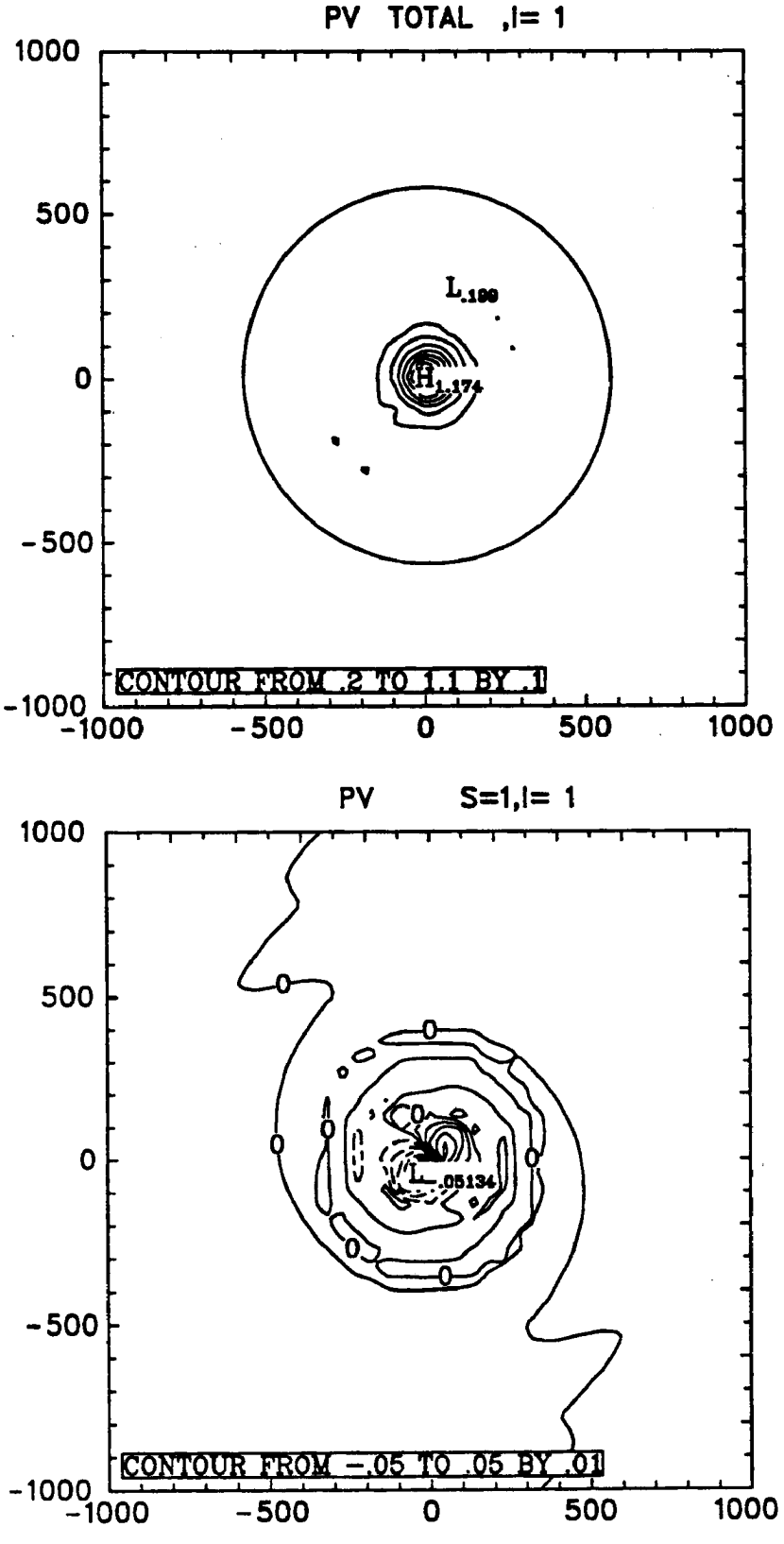

Figure 4.6: Potential vorticity after 48 hours of integration at 800 mb in ACF2

heating in ACF2 is concentrated in a small area where the vorticity is high and has a larger amplitude than heating asymmetry in ACF3, the asymmetric potential vorticity gradient near the vortex center in ACF2 is no larger than in ACF3 (Figs. 4.6) and 4.7), and the vortex moves slower when asymmetric heating is concentrated at smaller radii. This shows that the response of the vortex circulation to asymmetric heating is quite different than the response to symmetric heating. With symmetric heating the potential vorticity anomaly created by the presence of a diabatic heat source is larger for the source placed in the region with higher inertial stability. This is true for the tropical cyclones as well as other symmetric circulations (e.g., zonally symmetric Hadley circulation in Schubert et al., 1991). However, placing the asymmetric heating in the inertially stable region does not create large flow asymmetries. This result agrees with Carr and Williams' (1989) arguments on symmetrization of the flow in vortices with radial wind shear. Carr and Williams, using an analytical, barotropic model of a Rankine vortex, have shown that advection of asymmetric perturbations by radially shearing tangential mean flow destroys asymmetric perturbations. The damping is proportional to the magnitude of radial shear and the square of azimuthal wavenumber. Therefore, convective asymmetries in the hurricane eye-wall are unlikely to produce strong asymmetric circulation. Perturbations which maximize in the less stable area are damped at much slower rate. For example, potential

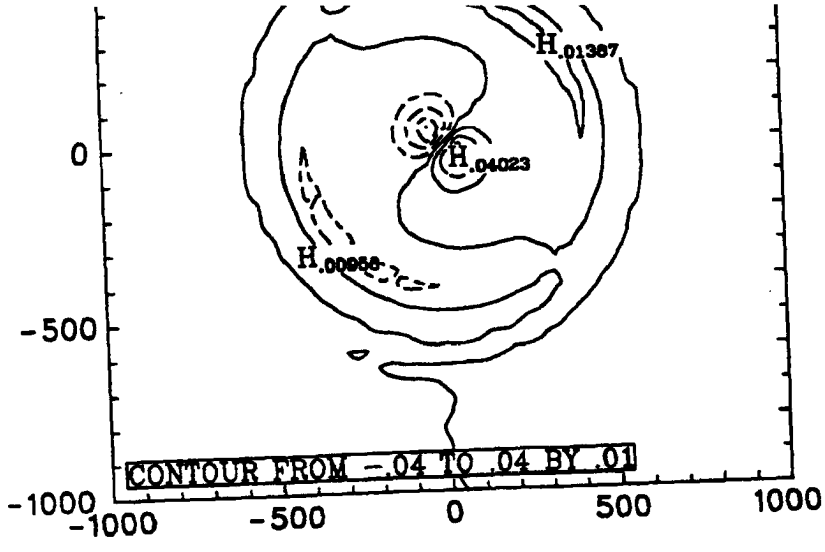

Figure 4.7: Potential vorticity after 48 hours of integration at 800 mb in ACF3

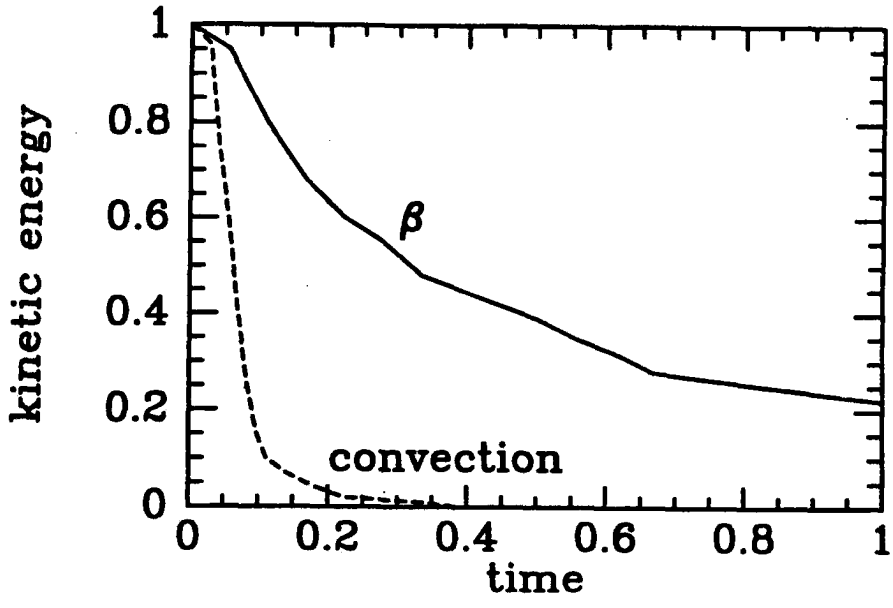

Figure 4.8: Decay of perturbation kinetic energy (normalized by initial value) with time for convection-induced (dash), and β-induced (solid) asymmetry (adapted from Carr and Williams, 1989).

vorticity anomalies created by advection of planetary vorticity are much more stable than those associated with asymmetries in the eye-wall convection (Fig. 4.8). These results suggest that a more appropriate conceptual model of the motion of the vortex under the influence of heating asymmetries should involve advection of an almost symmetric inner vortex by asymmetric flow associated with potential vorticity anomalies. These potential vorticity anomalies are the result of a redistribution of potential vorticity by diabatic heat sources, with a potential vorticity maximum developing below the source and minimum developing above the source.

In the next experiments we try to establish the role that steady heating asymmetries play in changing the movement of a vortex on a β-plane. As seen in Fig. 4.9, convective asymmetries (especially in the southern part of a cyclone) can persist for a few days. We choose the location of maximum asymmetric heating as RH=500 km from the vortex center. The amplitude of the heating is the same as in ACF3 (A=0.2), but asymmetric heating occupies the larger area (the half-width is 150 km instead of 30 km).

The influence of the heating asymmetry on movement can be seen from Fig. 4.10. When the asymmetric heating maximum is placed in the southern quadrant of the vortex

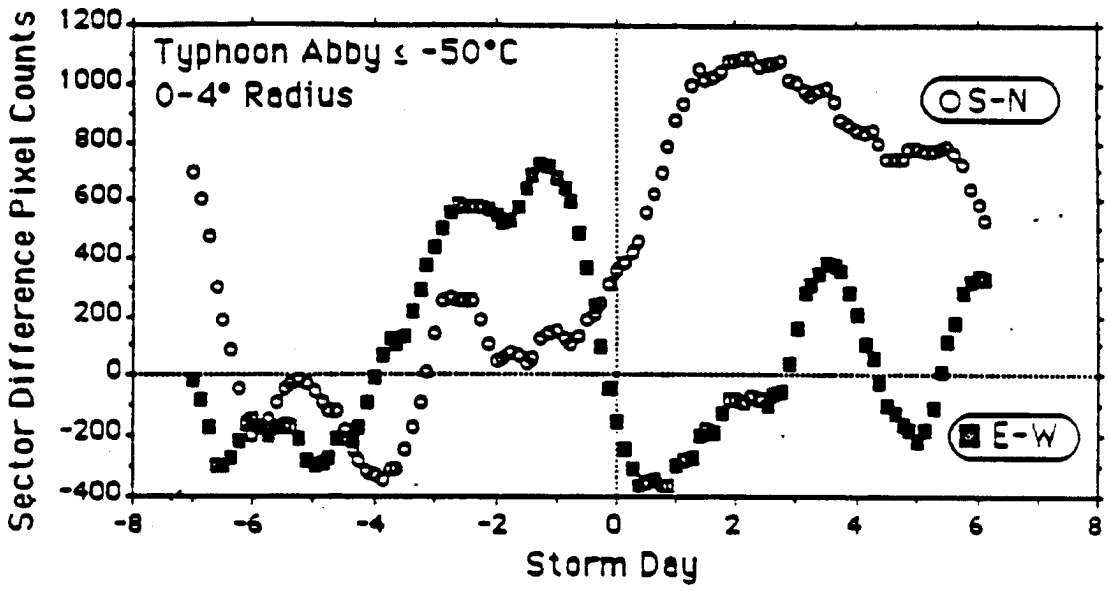

Figure 4.9: Time series of sector differences of -50^o convection for Typhoon Abby (from Shoemaker 1989)

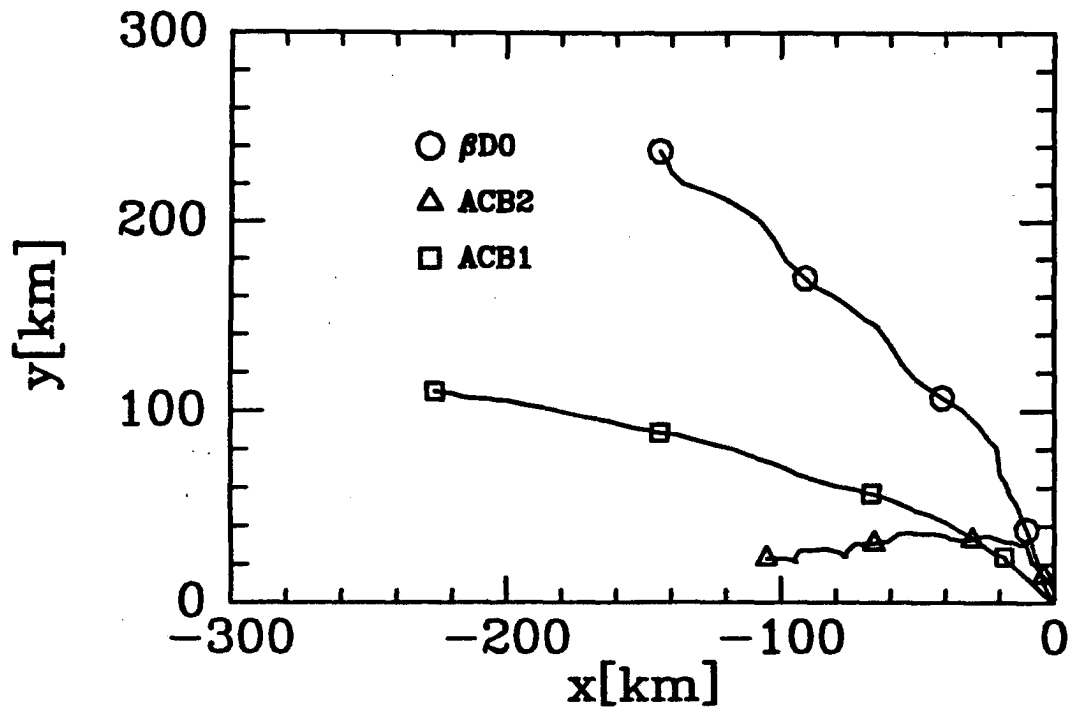

Figure 4.10: Trajectories of vortices in experiments ACB1, ACB2 (asymmetric heating on the β-plane) and βD0 (symmetric heating on the β- plane)

(experiment ACB1) the northward speed is decreased while the westward velocity of the moving vortex increases. This behavior can be explained by the fact that the presence of a heat source creates low-level potential vorticity maximum in the southern part of the vortex. The mean circulation advects the high potential vorticity air toward the east and low potential vorticity air toward the west. The flow between potential vorticity anomalies is directed toward the south-west, therefore reducing the β-induced northward motion, while strengthening the westward motion. When the heating maximum is placed in the southeastern quadrant (experiment ACB2) the vertical vorticity redistributions caused by the heat source reduces anomalies caused by advection of planetary vorticity (Fig. 4.11). The northward flow through the vortex center is reduced and the vortex becomes almost stationary.

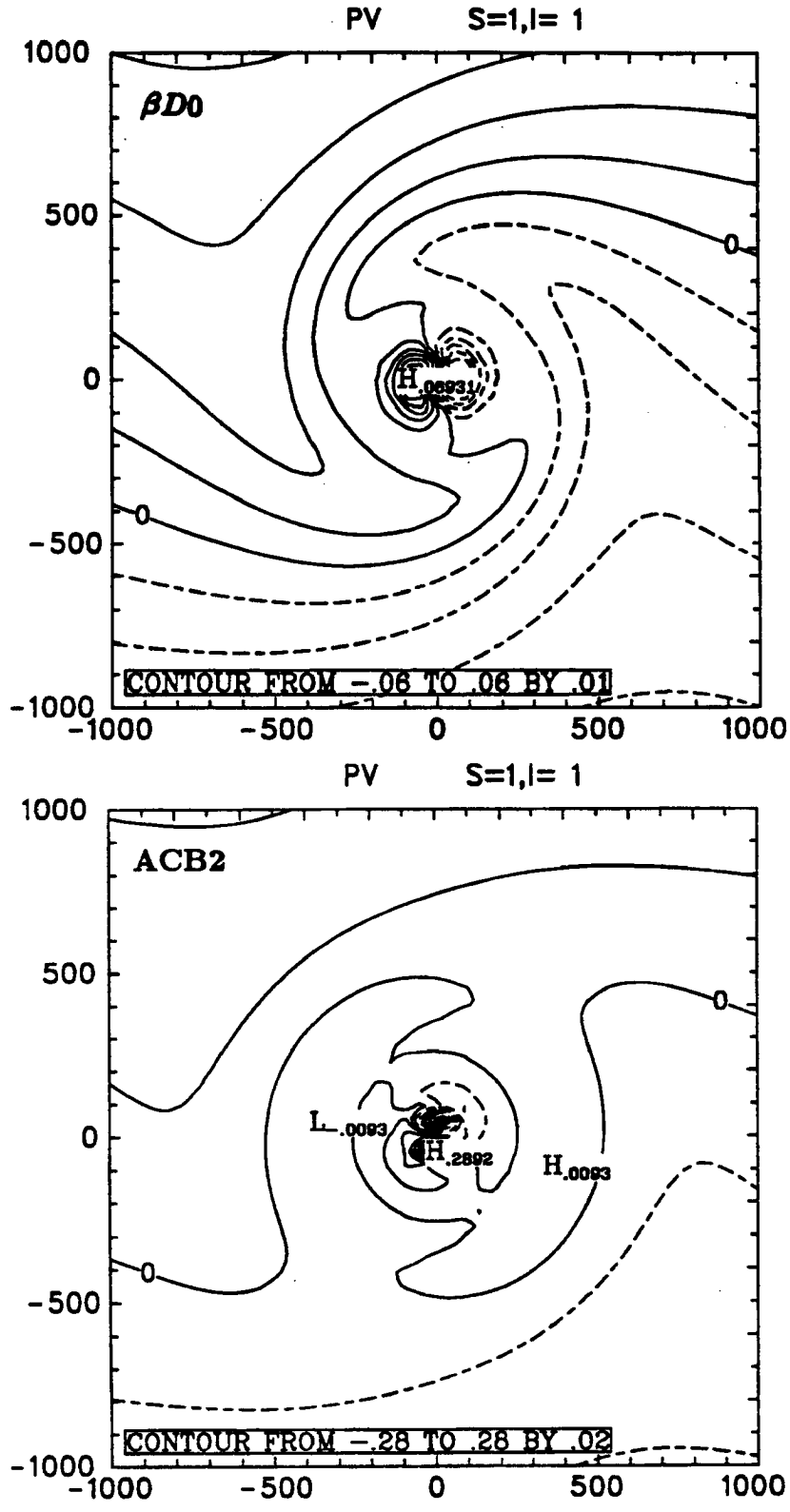

Figure 4.11: Asymmetric $s = 1$ component of 800 mb potential vorticity, after 48 h of calculation, in experiments $\beta D0$ (symmetric heating) and ACB2 (asymmetric heating)

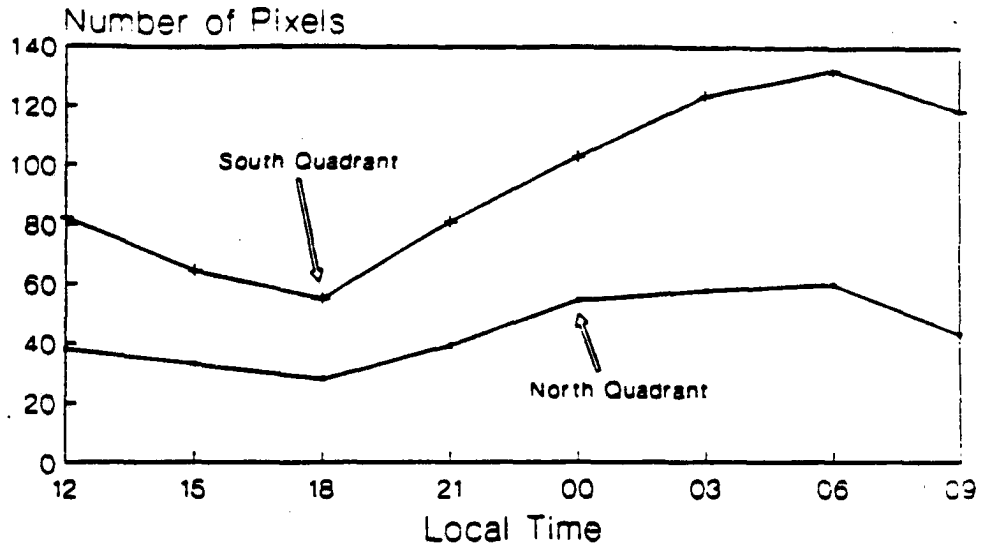

Figure 4.12: Diurnal variation of the north-south convective asymmetries as shown in the number of pixels colder than $-75°C$. From Hallin (1991).

4.2 Variable heating asymmetries

As outer convection varies on a diurnal basis, the north-south asymmetry also changes (Hallin, 1991), with the minimum in the evening (18 local time) and maximum in the early morning (Fig. 4.12).

In the next experiment, we examine the response of vortex motion to diurnal changes in diabatic heating in order to determine whether the diurnal cycle in heating asymmetries contributes to noticeable 24-hour fluctuations in the vortex path or speed. As in experiment ACB2, we assume that asymmetric heating has a maximum in the southeast quadrant, at RH=500 km from the vortex center. The heating and cooling, which integrated over 24 hours is the same as in ACB2, oscillates with the period of 24 hours. Therefore, the maximum heating (at RH=500 km) varies from zero to 40% of the maximum symmetric heating.

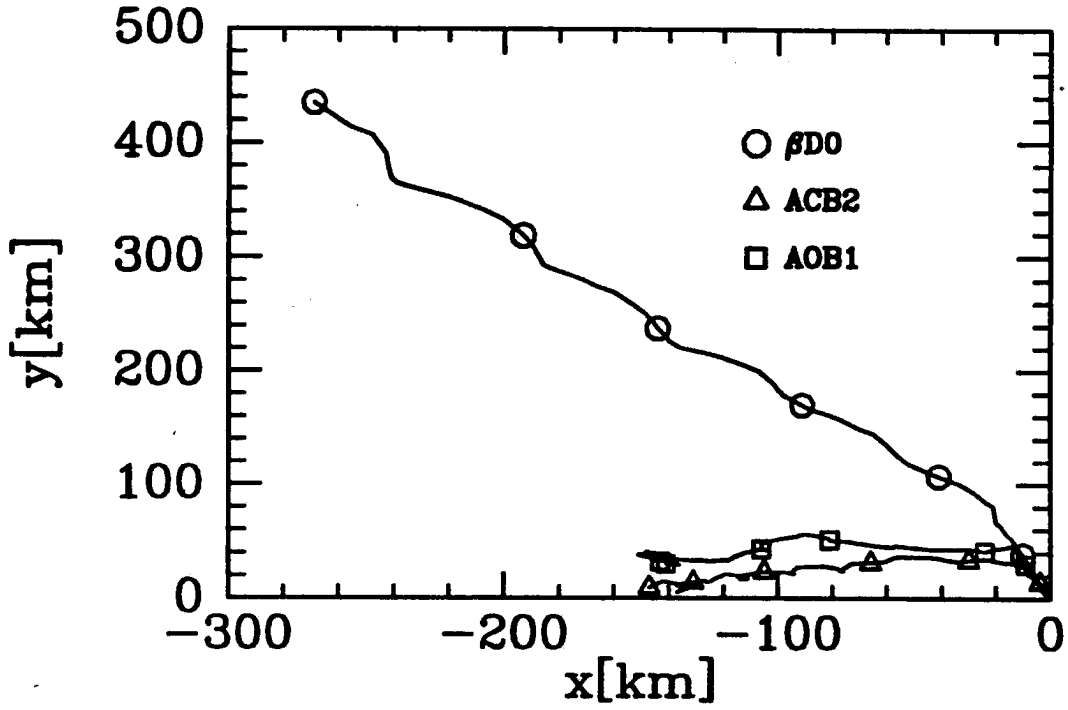

Figure 4.13: Trajectories of vortices in experiments ACB2 and AOB1

The trajectories of the vortex during three days of integration are shown in Fig. 4.13. We note that trajectories for experiments ACB2 and AOB1 are very similar and that the path in AOB1 does not suggest any diurnal oscillation. However, the oscillation can be detected in meridional and zonal vortex velocity. When asymmetric heating is at its minimum, the vortex moves toward the northwest as in the case of symmetric heating on the β-plane. For large asymmetric heating, the northward and westward velocity decreases. A time series of the difference in vortex meridional and zonal velocities between the oscillating and steady heating case are shown in Fig. 4.14. A twelve-hour running average is used to remove high-frequency temporal oscillations. The curves clearly show the 24-hour cycle. Although the amplitude of oscillation is fairly small (0.5ms^{-1}), it is comparable with the propagation velocity caused by the β effect(1.7ms^{-1} in meridional and 1.0ms^{-1} in zonal direction). We note also that this value (0.5ms^{-1}) agrees with the observed amplitude of the diurnal oscillations in cyclone motion (Hallin, 1991).

In a final experiment, we attempt to determine the influence of convective asymmetries which rotate around the cyclone center. Willoughby (1989) has shown, in his shallow

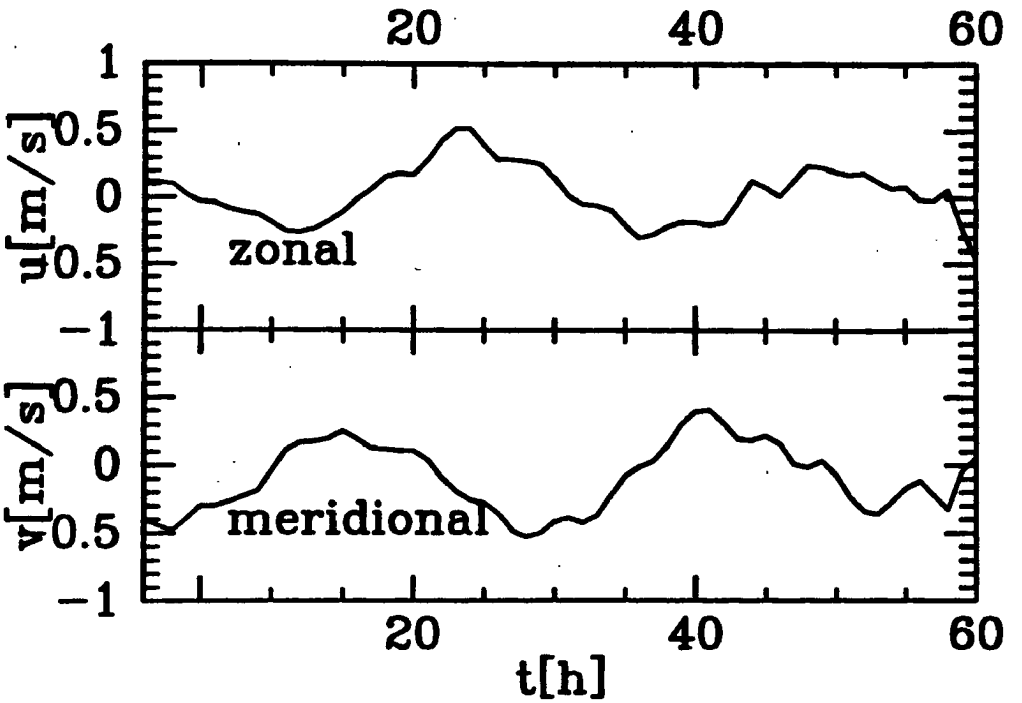

Figure 4.14: Diurnal variation of zonal and meridional velocities (AOB1-ACB2)

water linear model, that rotating sources and sinks of mass (representing asymmetric heat sources) influenced vortex motion. In Willoughby's model, the vortex motion was especially sensitive to mass sources rotating with the local angular velocity. To determine if the rotation of heat sources can enhance the response of the vortex to asymmetric heating at small radii, we repeated experiment ACF1, assuming that the asymmetry rotates with the angular velocity of the 900 mb tangential wind. Even though the movement of the vortex followed the heat source, the displacement of vortex from initial position was very small. Similar features were observed when we placed the rotating sources at larger radii. The direction of vortex movement agreed with the sense of rotation of diabatic heat sources, but we could not find any angular velocity for which a resonant response would occur.

4.3 Summary

In this chapter we investigated the response of baroclinic vortex motion to asymmetric heat sources. Our results show that heating asymmetries localized near the vortex center

do not have a large influence on vortex motion. However, when the asymmetries are placed at larger radii potential vorticity anomalies similar to "beta gyres" are created. The circulation associated with these anomalies advects the vortex. Heating anomalies located in the southern and southeastern part of a vortex significantly reduce the motion due to the β effect. Vortex motion also responds to time changes in the heating asymmetry.

Chapter 5

BAROTROPIC AND INERTIAL INSTABILITIES IN A HURRICANE OUTFLOW LAYER

In chapter II we have shown that the interaction between upper and lower layers of a baroclinic vortex can affect the motion of the vortex. We have examined the simple case of an initially symmetric vortex in a vertically sheared flow. In the next two chapters we will look at the dynamic processes in the outflow layer and their role in the vortex motion. The outflow, anticyclonic layer of a tropical storm its much more dynamically "active" than lower, inertially stable, layers. Both numerical models and observations indicate the existence of asymmetries of the upper layer flow. For example, Black and Anthes' (1971) analysis of wind fields in the outflow layer of four hurricanes and one tropical storm showed that horizontal eddies dominated the circulation beyond a radius of 400 km. Disturbances with azimuthal wavenumbers one and two accounted for most of the variance of momentum and kinetic energy. The question arises of how these asymmetries are generated. One obvious answer is they are due to interaction with the environment. Chen and Gray (1985) show the dependence of the outflow pattern on environmental synoptic conditions. However, the upper level asymmetries appeared also in a three dimensional numerical model which did not include the environmental flow (Anthes, 1972). This suggests that the asymmetries can be created by dynamic instability. In Anthes' (1972) model the wind in the upper layer of the modeled cyclone satisfied barotropic and inertial instability conditions. Energy budgets showed that barotropic conversion of mean to eddy kinetic energy was the dominant energy source for perturbations. Asymmetries which developed in this model had $s = 1$ and $s = 2$ azimuthal wavenumbers.

The criterion for barotropic instability demands that the gradient of potential vorticity changes sign somewhere in the domain (Ripa, 1983). Schubert and Alworth (1987)

discussed the mechanism by which the conditions favorable for barotropic instability can be created. They calculated the evolution of potential vorticity in a symmetric, balanced hurricane model and noted that during the early stages of the cyclone development a potential vorticity minimum in the upper level of the cyclone is located at the vortex center, above a potential vorticity maximum. Later on, the potential vorticity minimum gets pushed off the center by the ascending high potential vorticity air, thus creating a region where the potential vorticity gradient changes sign on an isentropic surface. This development can set the stage for barotropic instability. Merrill's (1985) composite analysis of upper-level wind fields in Atlantic hurricanes indicated that the vorticity gradient changes sign at about 400 km from the hurricane center. Merrill (1985,1988a) also suggested barotropic instability as a possible mechanism for creating the outflow asymmetries.

The inertial instability can develop in the regions where potential vorticity is negative. As suggested by Alaka (1962) this condition can be satisfied in the outflow layer of the observed tropical storms. It is also satisfied in some numerical models (Anthes, 1972; Kitade, 1980). However, Rotunno and Emanuel (1987) argue, using the results of their axisymmetric hurricane model, that although inertially unstable regions develop in the upper layer of the modeled cyclone, they are continually stabilized by moist convection.

In this chapter we try to throw some light on the complicated problem of hurricane outflow asymmetries by establishing the characteristics of barotropically and inertially unstable modes developing in the circular flow with the mean wind typical of the hurricane outflow layer. We follow the "classical" approach (e.g., Stevens and Ciesielski, 1986, and Gent and McWilliams, 1986) and treat inertial and barotropic instabilities using linear eigenvalue analysis. We first consider simplified tangential wind profile analogous to that used by Gent and Mc Wiliams (1986) . Later we use the wind profile observed in the hurricane outflow layer (namely the composite wind profile for Atlantic hurricanes from Merrill, 1985). Using this simplified model we can determine the growth rates of instabilities, wavenumbers of the most unstable modes, and the vertical scale and horizontal structure of the disturbances.

5.1 Model description

We use the equations for linearized perturbations in cylindrical coordinates (r, θ). We assume that the mean tangential wind depends only on radius ($\bar{v} = \bar{v}(r)$) and the mean radial wind vanishes ($\bar{u} = 0$). Because there is no vertical shear we can separate the vertical and horizontal structure (cf. Stevens 1983). The horizontal structure equations take the form.

$$\begin{aligned}
\left(\frac{\partial}{\partial t} + \bar{v}\frac{\partial}{r\partial\theta}\right)u' \;-\; \left(f + \frac{2\bar{v}}{r}\right)v' &= -\frac{\partial\Phi'}{\partial r}, \\
\left(\frac{\partial}{\partial t} + \bar{v}\frac{\partial}{r\partial\theta}\right)v' \;+\; \left(f + \frac{\partial(r\bar{v})}{r\partial r}\right)u' &= -\frac{\partial\Phi'}{r\partial\theta}, \\
\left(\frac{\partial}{\partial t} + \bar{v}\frac{\partial}{r\partial\theta}\right)\Phi' \;+\; \bar{\Phi}\left(\frac{\partial(ru')}{r\partial r} + \frac{\partial v'}{r\partial\theta}\right) + u'\frac{\partial\bar{\Phi}}{\partial r} &= 0.
\end{aligned} \tag{5.1}$$

In this system u', v' and Φ' are the horizontal structure components of radial and tangential velocity and geopotential perturbations, respectively. $\bar{\Phi} = gh + \int dr d\bar{\Phi}/dr$ where h is the separation constant arising from the solution of an eigenvalue problem for the vertical structure component of u, v and Φ. For the purpose of this calculation we assume that f is a constant.

We use a nondimensional form of the system (5.1) with a length scale equal to the earth's radius a, time scale $(2\Omega)^{-1}$ (where Ω is the earth's rotation rate), and velocity scale $(2\Omega a)$. Perturbations are assumed to have the form: $x'(r)\exp i(s\theta - \sigma t)$ where x' denotes u', v' or Φ', σ is the complex frequency and s is the azimuthal wavenumber. If we define the Doppler-shifted frequency $\hat{\sigma}$, absolute vorticity of the mean flow $\bar{\eta}$, and modified coriolis parameter $\tilde{f}$ as:

$$\begin{aligned}
\hat{\sigma} &\equiv \sigma - \frac{s\bar{v}}{r}, \\
\bar{\eta} &\equiv f + \frac{\partial r\bar{v}}{r\partial r}, \\
\tilde{f} &\equiv f + \frac{2\bar{v}}{r},
\end{aligned} \tag{5.2}$$

respectively, then (5.1) takes the form:

$$\begin{pmatrix} -\hat{\sigma} & \tilde{f} & -\frac{d}{dr} \\ \bar{\eta} & -\hat{\sigma} & \frac{s}{r} \\ \frac{\bar{\Phi}}{r}\frac{d}{dr}r + \frac{d\bar{\Phi}}{dr} & \frac{gh}{r}s & -\hat{\sigma} \end{pmatrix} \begin{pmatrix} -iu' \\ v' \\ \Phi' \end{pmatrix} = \begin{pmatrix} 0 \\ 0 \\ 0 \end{pmatrix}. \tag{5.3}$$

Eq. (5.3) is discretized in the radial direction on a staggered grid. Geopotential Φ' is defined at points $r = n\Delta r$ and u' and v' are defined at $r = (n+1/2)\Delta r$ where $n = 0, 1, 2...$ and Δr is the grid spacing. For the results to be shown, $\Delta r = 25$ km. The resulting eigenvalue problem for eigenvalues σ and eigenfunctions $(-iu', v', \Phi')$ is solved numerically with the following boundary conditions:

1. At the outer boundary ($r = 1500$ km) assuming no interaction of the cyclone with the environment implies:

   $u' = 0$

2. At the vortex center ($r = 0$) continuity of all physical variables in cylindrical coordinates requires:

   $\Phi' = 0$ for $s \neq 0$,

   $d\Phi'/dr = 0$ for $s = 0$.

Upon solving (5.3) we look for eigenvalues σ with a positive imaginary part as an indication of an instability.

5.2 Barotropic instability

5.2.1 Gaussian streamfunction profile

To investigate the role of barotropic instability we have used three different mean vorticity profiles. The first profile corresponds to the Gaussian streamfunction $\bar{\psi} = \psi_0 \exp(-r^2/r_\psi^2)$. Parameters $\psi_0 = .1 f_0 \times r_\psi^2$ and $r_\psi = 300$ km are chosen to satisfy the condition: $\mid \bar{\zeta} \mid \ll \mid f_0 \mid$. Mean tangential velocity is given by $\bar{v} = \partial\bar{\psi}/\partial r$ and mean relative vorticity by $\bar{\zeta} = 1/r\partial(r\bar{v})/\partial r$. In the second case (Fig. 5.1a) the magnitude of the mean vorticity is increased by a factor of ten, so that the flow is no longer geostrophic. The third profile, shown in Fig. 5.1b corresponds to the composite observed vorticity profile in the hurricane outflow layer from Merrill (1985) .

The first vorticity profile is used to compare the shallow water model results with Gent and McWilliams' (1986) barotropic instability calculations for quasi-geostrophic flow

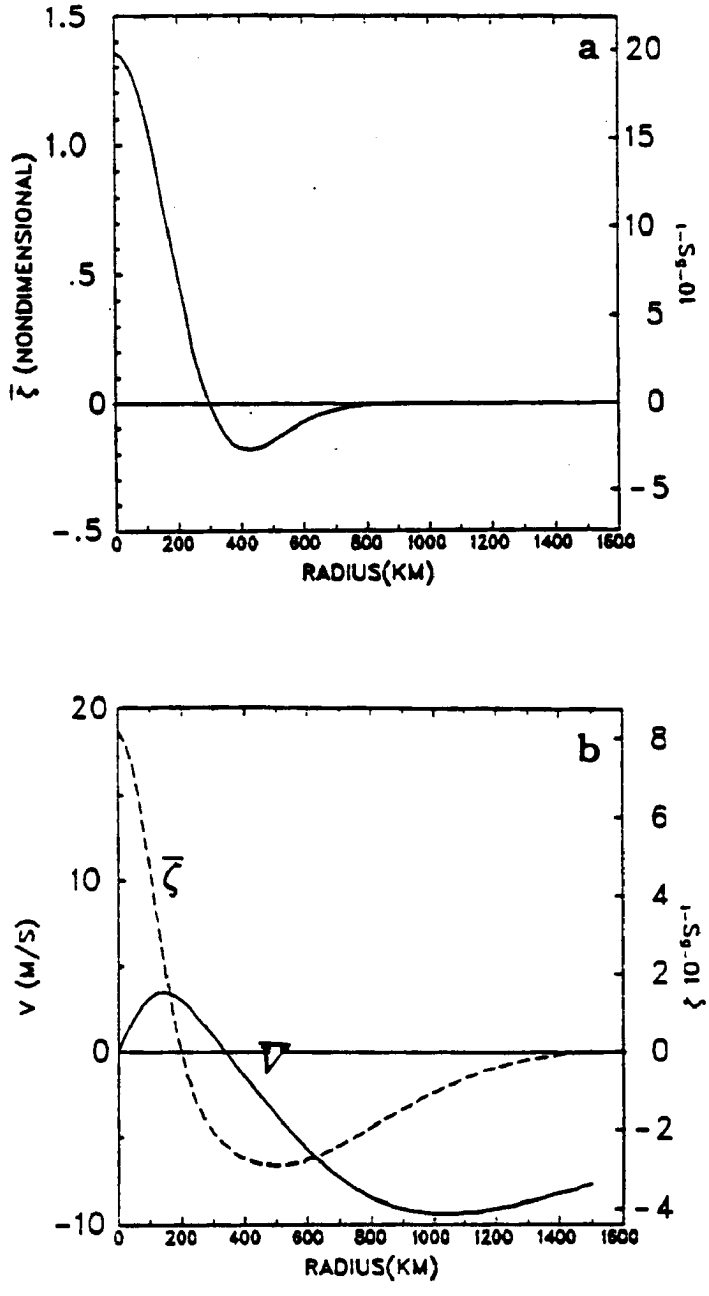

Figure 5.1: Relative vorticity of the mean flow for Gaussian nongeostrophic case ($\psi_0 = f_0 \times r_\psi^2$); and (b) relative vorticity and mean tangential wind for hurricane outflow layer from Merrill (1985)

in cylindrical coordinates. Gent and McWilliams solved the eigenvalue problem for the nondimensional, linearized quasi-geostrophic potential vorticity equation in the form:

$$(c - \bar{\psi}_r/r)[(r\psi_r)_r/r - (s^2/r^2 + m^2)\psi] + \psi\bar{Q}_r/r = 0 \tag{5.4}$$

where m is the vertical mode parameter, $c = \sigma/s$, and $\bar{Q}$ is the mean flow potential vorticity. The mean flow streamfunction $\bar{\psi}$ has the form: $\bar{\psi} \propto \exp(-r^2)$. It can be shown from (5.4) that the necessary condition for instability requires that $\partial\overline{Q}/\partial r$ changes sign somewhere in the domain. Since we are considering barotropic mean state flow and $f = f_0$, this is equivalent to the condition that the radial derivative of relative vorticity changes sign. All profiles used in our experiments satisfy this condition. In order to compare quasi-geostrophic results with those obtained using shallow water equations, we calculate dimensional values for Gent and McWilliams' parameters using the following scales:

length scale L=r_ψ=300 km

vorticity scale V/L= $0.1f_0 = 0.5 \times 10^{-5}\text{s}^{-1}$

velocity scale V=$0.1f_0L = 0.5 \times 10^{-5} \cdot 3 \cdot 10^5 = 1.5$ m/s.

In Figs. 5.2a and 5.2b we display the results of the shallow water model using the parameter m as well as the equivalent depth h. The values of the equivalent depth h in the shallow water system corresponding to different m's in Eq. (5.4) can be found by comparing the potential vorticity equation (5.4) with the analogous equation for the shallow water system:

$$-i\hat{\sigma}(\zeta' - \frac{\bar{\eta}}{\bar{\Phi}}\Phi') + u'\frac{d\bar{\eta}}{dr} = 0. \tag{5.5}$$

The term $\Phi'\bar{\eta}/\bar{\Phi}$ in Eq. (5.5) corresponds to $m^2\psi$ in Eq. (5.4). Therefore in dimensional form we have

$$\frac{f_0\bar{\eta}}{gh}\Phi' = \frac{m^2}{L^2}\Phi'. \tag{5.6}$$

When the vorticity of the mean flow is much smaller than f_0, $\bar{\eta} \approx f_0$ and we can write

$$h \approx \frac{L^2 f_0^2}{m^2 g}.$$

Therefore we define m as

$$m^2 \equiv \frac{L^2 f_0^2}{gh} = \frac{L^2}{L_{R0}^2} \tag{5.7}$$

where L_{R0} denotes the geostrophic Rossby radius. We continue to use the parameter m defined by (5.7) with $L = 300$ km to indicate the equivalent depth for nongeostrophic cases (Fig. 5.2b and 5.3) even when the condition $| \bar{\zeta} | \ll | f_0 |$ is not satisfied.

Our results for wave numbers one and two, shown in Fig 5.2a are identical with those obtained by Gent and McWilliams. The largest instability occurs at $s = 1$ and vertical mode $m = 0.8$ which corresponds to the equivalent depth $h = 35$ m. This is different from results for parallel shear flow where the most unstable mode is always external ($m = 0$ or $h = \infty$). At $s = 2$ the external mode is the most unstable, but its growth rate is about one half the maximum growth rate at $s = 1$. It is also worth noting that the instability is very weak - with the maximum growth rate corresponding to an e-folding time scale of $\tau = 23$ days. The growth rates for higher wave numbers $s > 2$ are much smaller than those for $s = 1$ and $s = 2$.

When we increase the mean vorticity ten times the flow is no longer geostrophic but the dependence of the growth rates on the equivalent depth does not change drastically. Fig. 5.2b shows that the equivalent depth for the maximum growth rate slightly increases (to about 40 m). The growth rates at $s = 1$ and $s = 2$ increase approximately ten times. In addition the internal instability at $s = 1$ becomes even more significant in comparison to the external instability at $s = 2$. The e-folding time scale corresponding to the maximum instability is equal to 1.7 days.

5.2.2 Composite hurricane outflow layer

To investigate the role of barotropic instabilities in hurricane development we ran our model with the velocity profile in the outflow layer from Merrill (1985) . The mean tangential wind and relative vorticity for this flow is shown in Fig. 5.1b. The relative vorticity in the hurricane outflow layer has a minimum roughly at the same radius as the vorticity for the Gaussian non-geostrophic case shown in Fig.5.1a. The magnitude of the vorticity at this radius is also the same, but the region with anticyclonic absolute vorticity is about two times wider in the hurricane outflow case. As was shown by Gent and McWillams for geostrophic flow, the increase in the radial scale of the mean vortex

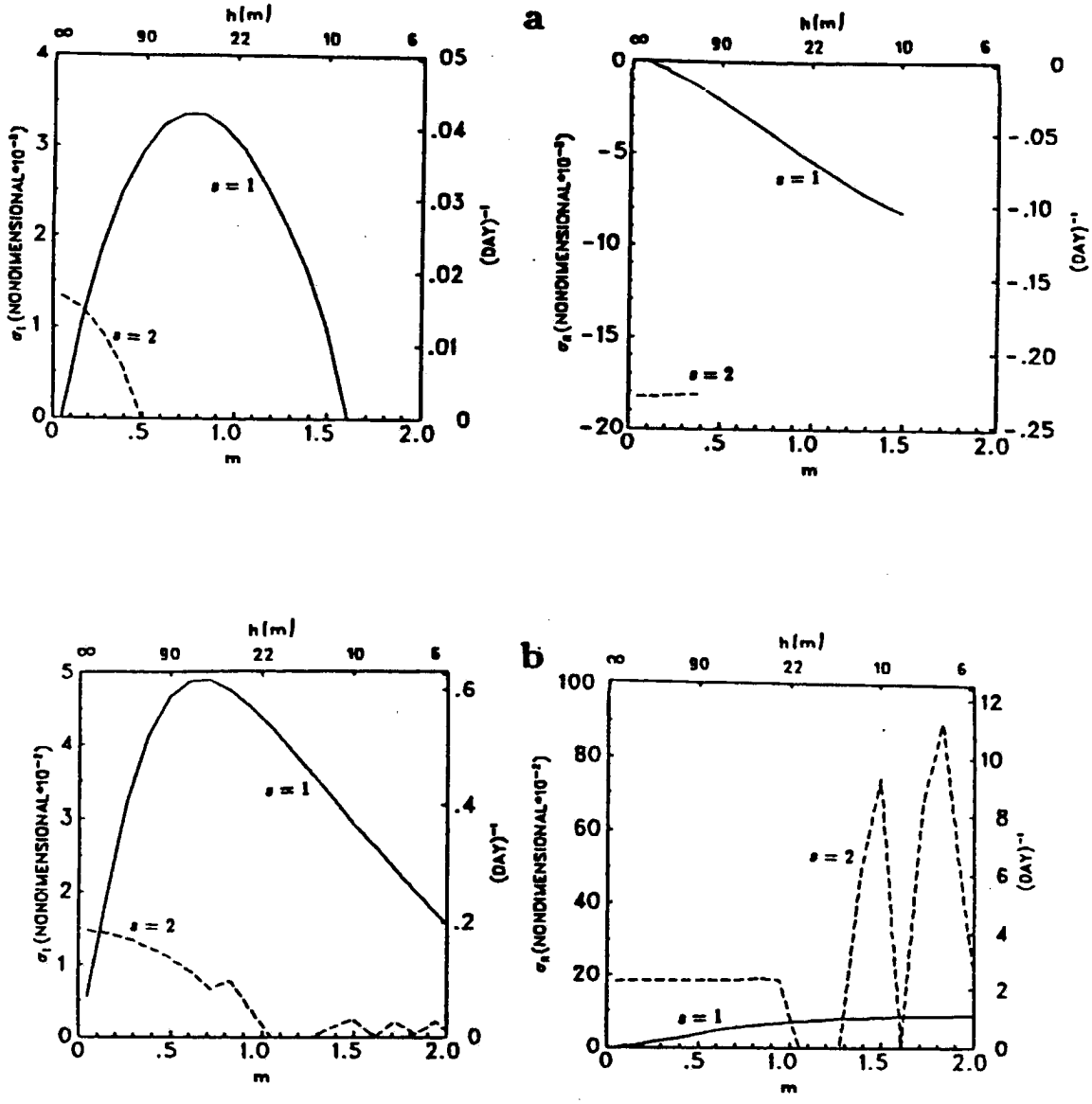

Figure 5.2: Frequencies and growth rates of the most unstable modes for the Gaussian streamfunction profiles. (a) for Gaussian geostrophic mean flow; (b) for Gaussian non-geostrophic mean flow.

causes a decrease in growth rate. Comparison of Figs. 5.2b and 5.3 shows that this is also true in the nongeostrophic case. The growth rates for the composite hurricane outflow are approximately four times smaller than those for the exponential profile case and the e-folding time for the maximum instability is about 7 days. The equivalent depth for this mode is $h = 25$ m. The vertical structure corresponding to this equivalent depth is shown in Fig. 5.4 which was adapted from Hack and Schubert (1986) . The maximum growth rate for $s = 2$ is about four times smaller and occurs for the largest investigated equivalent depth ($h = 9$km).

A test of numerical stability shows that the eigenvalue results for $s = 1$ are not sensitive to increased radial resolution. For $s = 2$, new unstable modes appear for small equivalent depths when the resolution of the model is increased. They are characterized by singular frequencies satisfying the condition $F(r) = (\hat{\sigma}_R)^2 - \tilde{f}\bar{\eta} = 0$. It can be shown that if we combine the system (5.1) into one equation for Φ', the resulting equation has the singularity for critical radius r_s such that $F(r_s) = 0$. Those instabilities are the manifestation of neutral inertial oscillations, which due to limited resolution are not properly resolved in our model.

In Fig. 5.5 we display the perturbation wind associated with the most unstable, $s = 1$ mode. The u and v perturbations structure is similar to that obtained for the geostrophic case and the Gaussian streamfunction profile. The amplitude of the disturbance is largest at $r = 0$ and decreases away from the storm center (note that only $s = 1$ perturbations can have non-zero winds at the storm center). There is no significant wind perturbation beyond $r = 400$ km. For $s = 2$ (not shown) the disturbance has maximum winds at about 400 km. The radial wind perturbation vanishes at the outer radius $r = 1500$ km as a result of imposed boundary conditions, but it decreases much more slowly than in the $s = 1$ case. Fig. 5.6 shows the wind and geopotential fields in the inner region for $s = 1$. It can be seen that the flow is strongly cross-isobaric so that quasi-geostrophy would not be a good assumption.

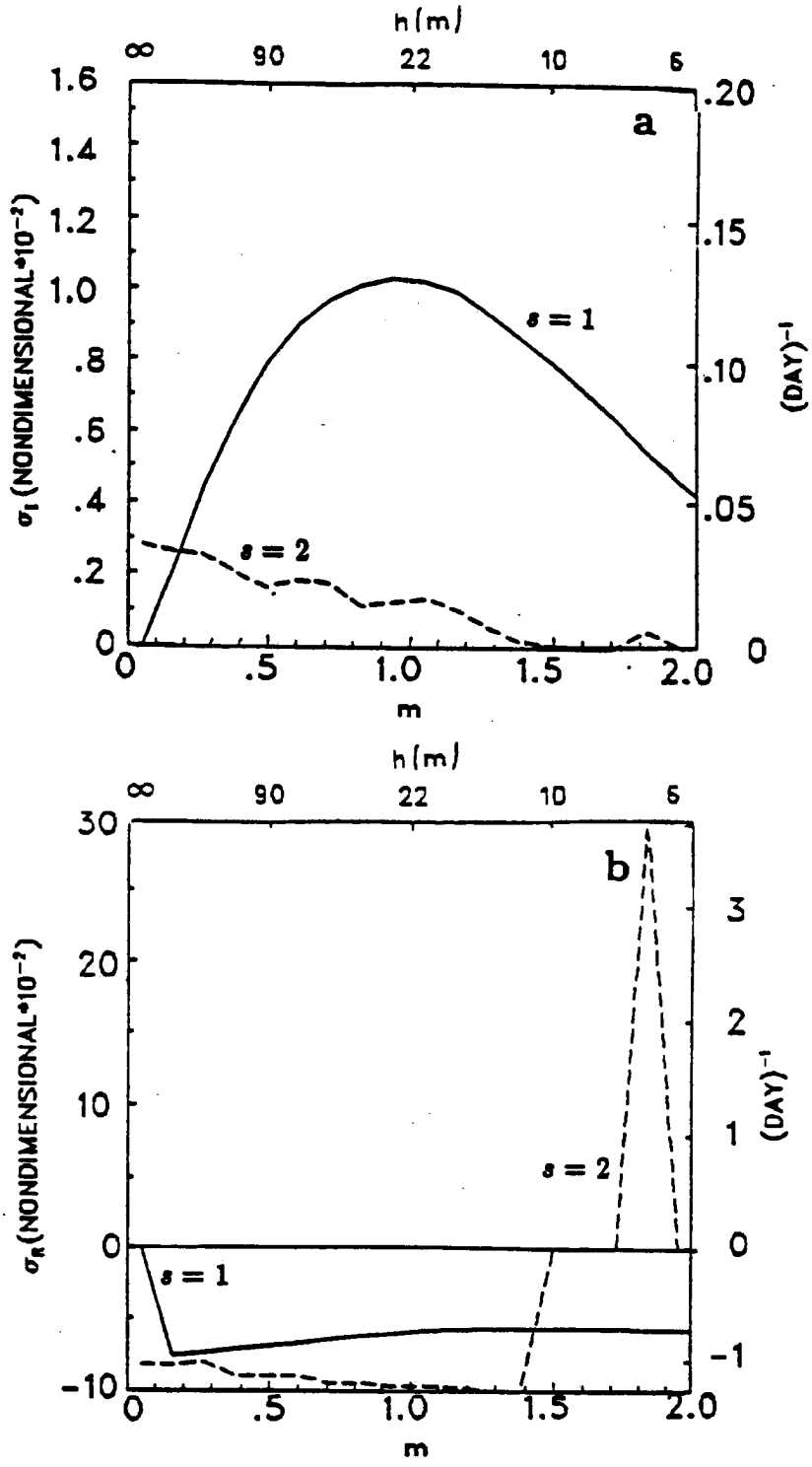

Figure 5.3: (a) Growth rates and (b) frequencies of the most unstable modes for $s = 1$ (solid line) and $s = 2$ (dashed line) for composite hurricane outflow.

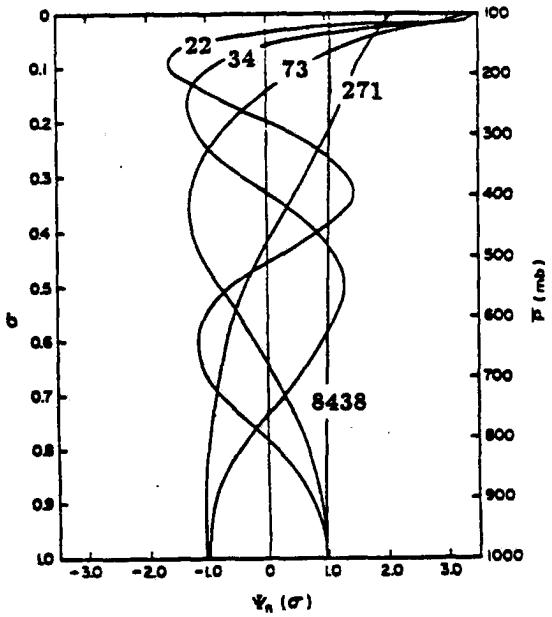

Figure 5.4: Vertical structure of the modes with different equivalent depths (in meters), calculated using static stability for the clear tropical areas. (adapted from Hack and Schubert's (1981) Fig.1).

In the absence of a secondary circulation, the momentum equation for the azimuthally averaged tangential wind can be written as

$$\frac{\partial \bar{v}}{\partial t} = -\bar{u}\frac{\partial \bar{v}}{\partial r} - \left(f + \frac{\bar{v}}{r}\right)\bar{u} + F_{nsym} \tag{5.8}$$

where F_{nsym} denotes the forcing on the mean flow by wave momentum fluxes and can be written as

$$F_{nsym} = -\frac{\partial(r\overline{u'v'})}{r\partial r} + \frac{\overline{u'v'}}{r} = \frac{\partial(r^2\overline{u'v'})}{r^2\partial r}. \tag{5.9}$$

Angular momentum fluxes $r\overline{u'v'}$ and eddy forcing $-1/r^2\partial(r^2\overline{u'v'})/\partial r$ for $s = 1$ and $s = 2$ are shown in Fig. 5.7. In both cases one can see the abrupt change of momentum flux at the critical radius where $\hat{\sigma}_R = 0$ (at about 400 km). The effect of the critical radius is more pronounced at $s = 2$. The $s = 1$ disturbance which reaches the hurricane center shows strong eddy forcing close to the vortex center, in the region of the cyclonic mean vorticity[3]. These results agree with the analogy between barotropic instability and overreflection

[3]Experiments with different vorticity in the center show that as the cyclonic vorticity decreases, the momentum flux profile for $s = 1$ approaches that for $s = 2$ with an abrupt change at the critical radius.

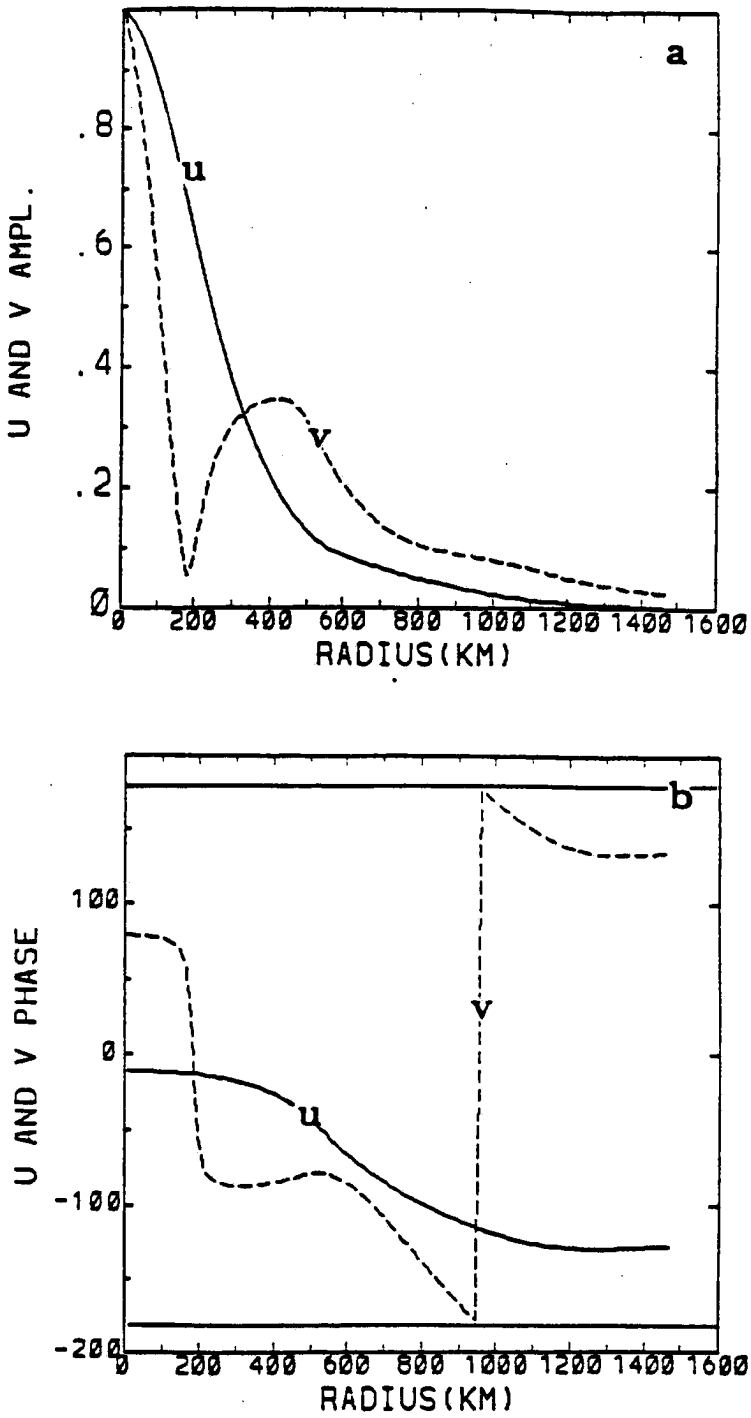

Figure 5.5: Barotropic instability in the hurricane outflow layer. u (solid line) and v (dashed line) eigenfunctions for the most unstable mode ($s = 1$), $h = 25$m, $\sigma = (0.055, 0.013)$. (a) amplitude; (b) phase;

as shown by Lindzen and Tung (1978). They note that although barotropic instability demands the existence of the inflection point, the key interaction between the disturbance and the mean flow occurs at the critical radius, not at the inflection point. They also point out that another necessary condition for barotropic instability - the semicircle theorem - requires that the critical radius exists somewhere in the domain.

5.3 Inertial vs. barotropic instability

The wind profiles we considered up to now did not satisfy the necessary (and sufficient) condition for inertial instability; i.e., in all cases the inertial parameter $\tilde{f}\bar{\eta}$ was greater than zero at all radii. Now, we modify slightly the basic state for the hurricane outflow layer, in order to assess the character of inertial instability. In the first experiment we simply decrease the value of the coriolis parameter from $f = 0.5 \times 10^{-4} s^{-1}$ (20°N) to $f = 0.25 \times 10^{-4} s{-}1$ (10°N). As shown in Fig. 5.8a, this change creates an area of negative $\tilde{f}\bar{\eta}$ between 400 and 700 km from the hurricane center with the minimum value of the nondimensional inertial parameter $(\tilde{f}\bar{\eta})_{min} = -1.56 \times 10^{-3}$. In a second experiment the wind profile is modified (Fig. 5.8b) in order to obtain stronger instability. When the anticyclonic wind is increased by a factor of two, the minimum instability parameter reaches $(\bar{\eta}\tilde{f})_{min} = -1.47 \times 10^{-2}$. Following Stevens and Ciesielski (1986) we introduce the parameter $\epsilon = \sqrt{-(\tilde{f}\bar{\eta})_{min}}$ which represents the maximum possible nondimensional growth rate. In the first experiment $\epsilon = 0.039$ and in the second experiment $\epsilon = 0.12$. The corresponding e- folding time scales are 48 and 16 hours, respectively.

The ratio of the growth rate of the most unstable mode to the maximum possible growth rate for different equivalent depths is shown in Fig. 5.9. The comparison of these results with the growth rates of the barotropic instability calculated before, shows that decreasing the coriolis parameter increases only slightly the maximum possible growth rate. The most unstable mode appears now at $s = 0$ and the smallest investigated equivalent depth $h = 0.01$m. The real frequency of this mode is equal to zero, and the growth rate approaches ϵ. This agrees with Stevens' (1983) results for inertial instability. The growth rate of the symmetric mode decreases very rapidly with increasing equivalent depth and for

$h = 0.1$ m is equal to zero. For $s = 1$ the maximum instability occurs also for $h = 0.01$ m and its growth rate is only slightly smaller than that for s=0.

For $s = 2$ (not shown) the maximum growth rates also occur for the smallest equivalent depths. The results for these equivalent depths display the numerical instabilities mentioned earlier, and therefore it is difficult to precisely determine the shape of the $\sigma_I(h)$ curve. As best as we can determine though, the maximum growth rate for $s = 2$ is no greater than 0.3ϵ. When the anticyclonic wind is increased by a factor of two, and the minimal value of the inertial parameter reaches -0.0156, the maximum nondimensional growth rate becomes much larger (e-folding time scale of 16 hours). Still, the inertial instability dominates only for very small equivalent depths ($h < 0.1$m).

The wind structure for inertial instability at $s = 1$ is shown in Fig. 5.10; the symmetric instability ($s = 0$) structure is similar. Unlike the barotropic instability case, the disturbance is confined to the region where the condition for instability is satisfied. The radial scale of the disturbance is small compared with the azimuthal scale. It can be seen from Figs. 5.10 that the disturbance resembles the inertial instability on a sphere as calculated by Stevens and Ciesielski (1986). As the equivalent depth increases the perturbation wind maximum migrates toward the vortex center and gradually the structure of the most unstable mode approaches the structure of the barotropic mode shown in the previous section. For $h > 10$ m the structure of the most unstable mode is identical to the structure of the barotropically unstable modes investigated earlier, and therefore may be indentified as barotropic instability.

The results described above suggest that inertial instability alone cannot be responsible for the hurricane intensity change. The most unstable modes which occur at infinitesimal vertical scales (in our case the smallest vertical scales we examined $h = 0.01$m) are very likely to be stabilized by turbulent mixing processes. At large vertical scales, the influence of inertial instability rapidly decreases and the most unstable modes are connected with barotropic instability, with e-folding times of the order of a few days.

5.4 Summary and conclusions

In the previous sections we examined inertial and barotropic instabilities, in the context of a shallow water, linear model in cylindrical coordinates. We have shown that if the flow is geostrophic, i.e. $| \zeta | \ll | f_0 |$, barotropic instabilities are essentially identical to those obtained by solving the quasi-geostrophic potential vorticity equation (Gent and McWilliams, 1986). For this case we found that the fastest growing mode is internal, with a slow growth rate $\tau = 23$ days.

When we considered the composite, observed profile of the mean tangential flow in the hurricane outflow layer, we were able to identify inertial and barotropic instabilities. Inertially unstable modes had very small vertical scale and in a real atmosphere would be stabilized by turbulence. The symmetric mode was the most unstable but only for the smallest (generally unobservable) scales. Therefore inertial instability is not likely to dominate the dynamical processes in the hurricane outflow layer.

Barotropically unstable modes revealed some features observed in the hurricane outflow channels. For example, the most unstable modes occurred for azimuthal wavenumber $s = 1$ and $s = 2$. The structure of the most unstable modes resembled the outflow channels from Black and Anthes (1971). The instabilities had rather small growth rates (e-folding time for the most unstable modes was about 7 days). The period of oscillation for this mode was about 1.7 day. The slow growth rates suggest that the spontaneus development of asymmetries (without the influence of environment) is not very probable. However, the small frequency of the unstable modes indicates that time-dependent environmental factors can cause resonant response.

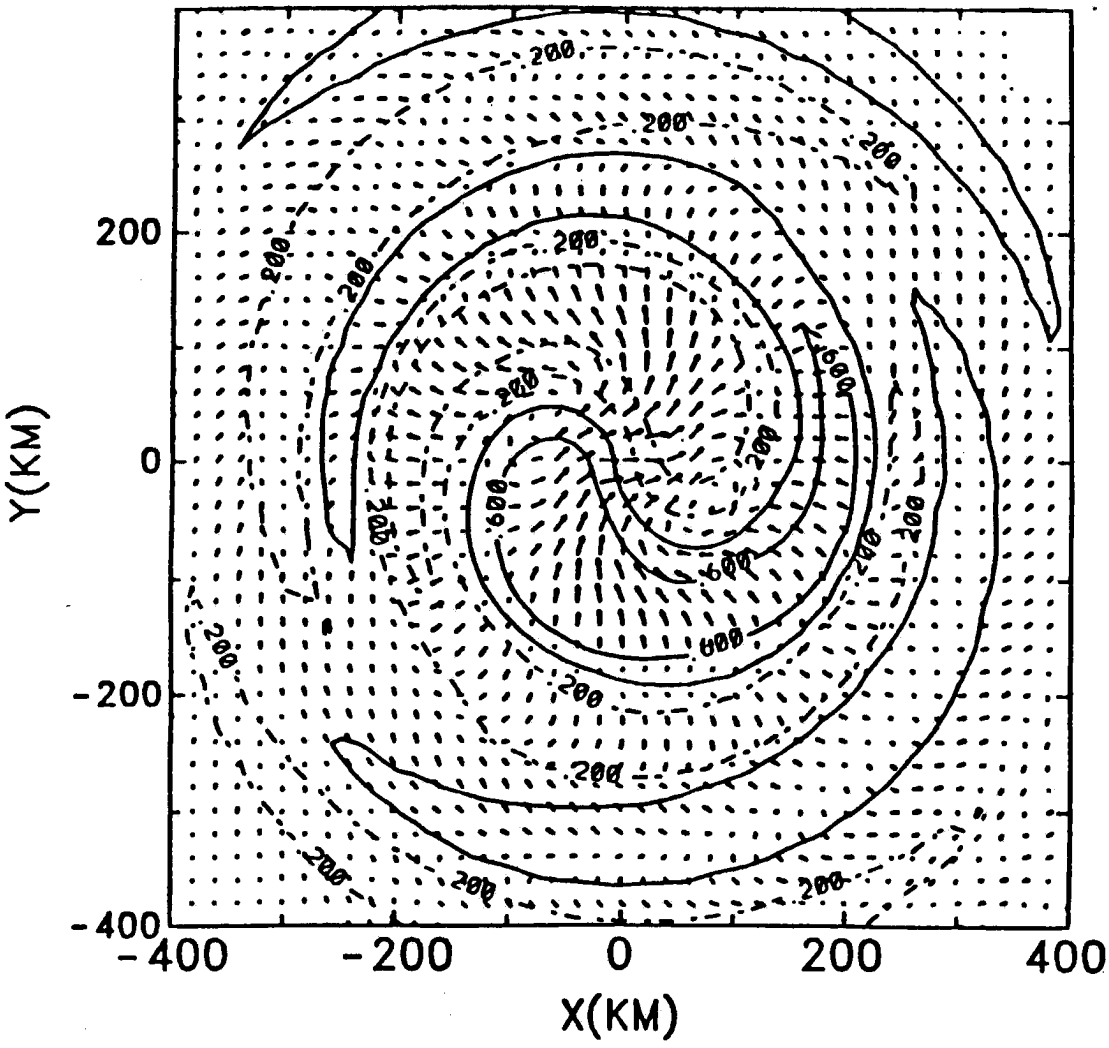

Figure 5.6: Barotropic instability. Wind and geopotential structure for the most unstable mode.

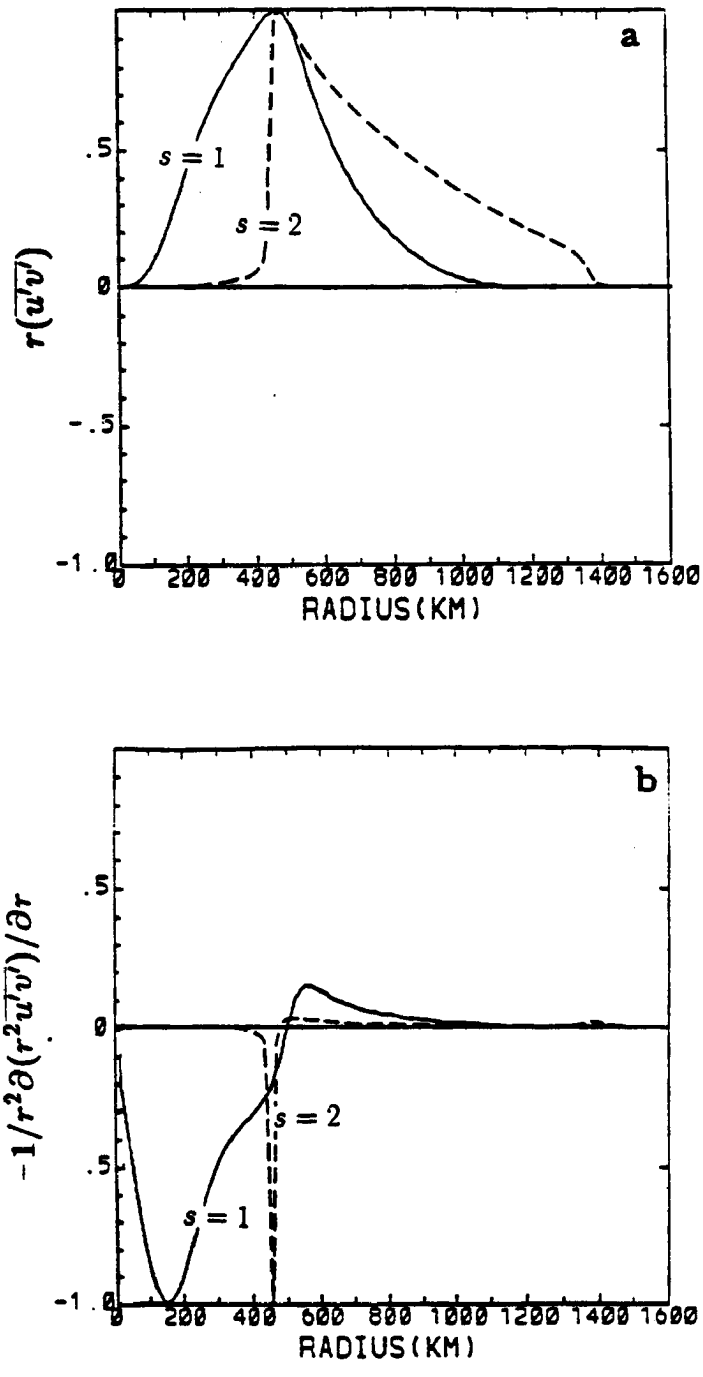

Figure 5.7: Momentum flux $\overline{ru'v'}$ and radial and radial forcing $-1/r^2\partial(r^2\overline{u'v'})/\partial r$ for barotropic instability (a) momentum flux for $s = 1$, (b) radial forcing for $s = 1$, (c) momentum flux for $s = 2$, (d) radial forcing for $s = 2$

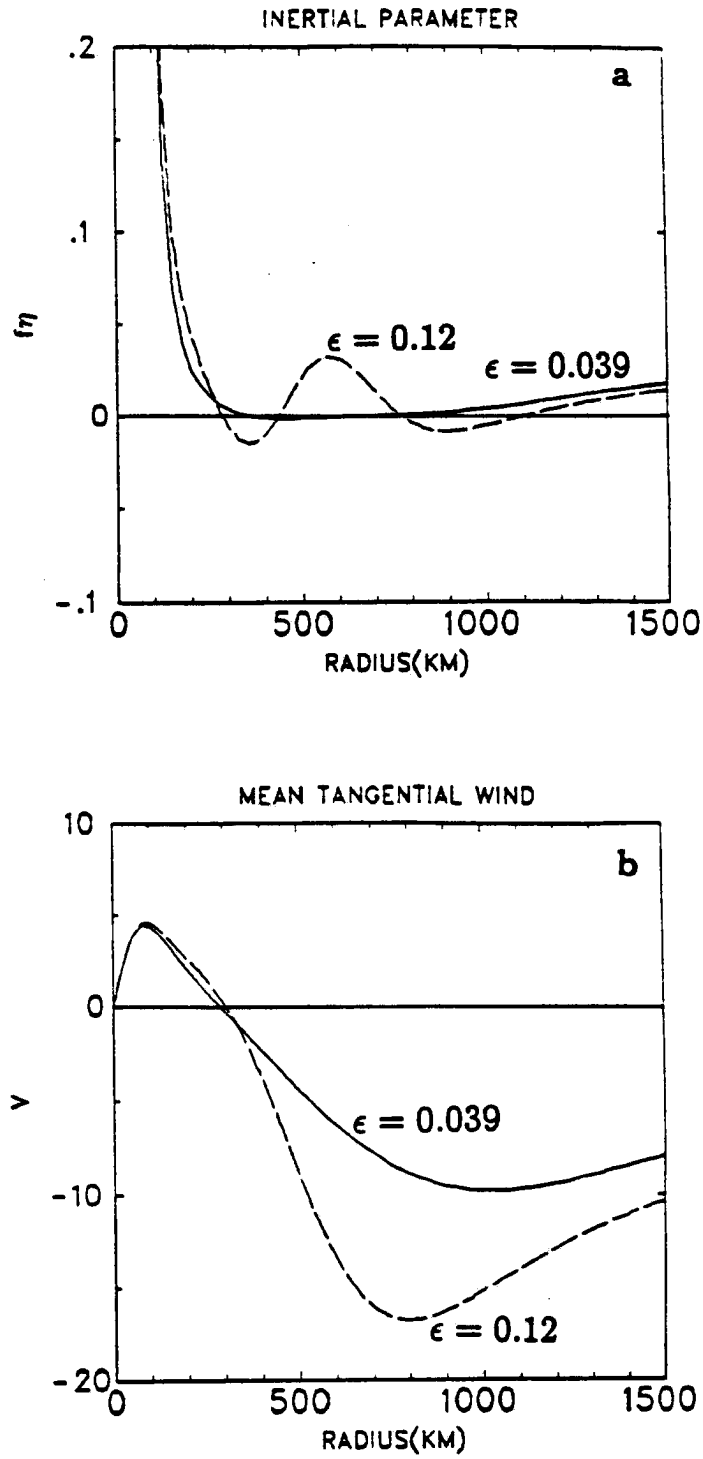

Figure 5.8: (a) Inertial parameter ($\tilde{f}\tilde{\eta}$) and (b) mean tangential wind profile for the two inertial instability experiments. Solid line - $\epsilon = 0.039$, dashed line $\epsilon = 0.12$.

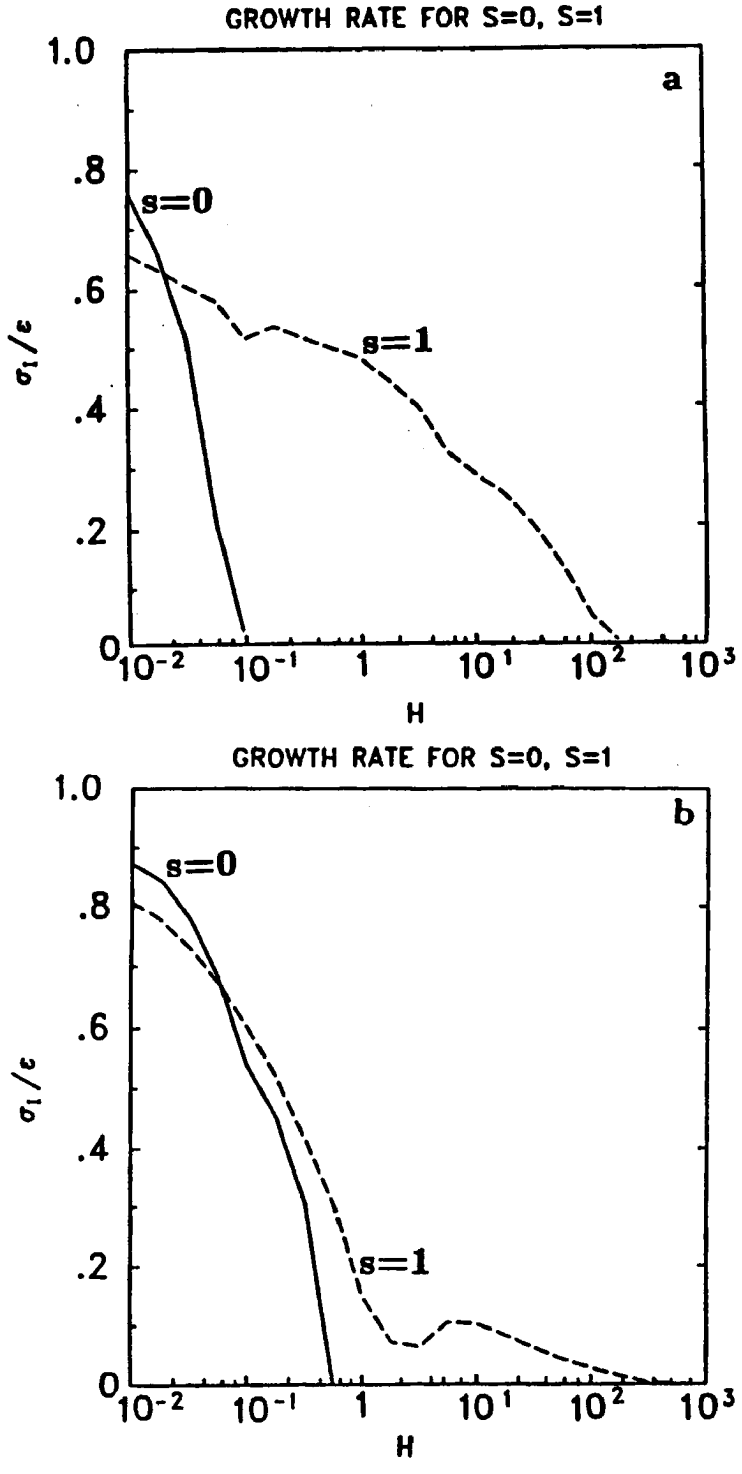

Figure 5.9: Largest growth rates as a function of equivalent depth. (a) for $\epsilon = 0.039$, (b) for $\epsilon = 0.12$.

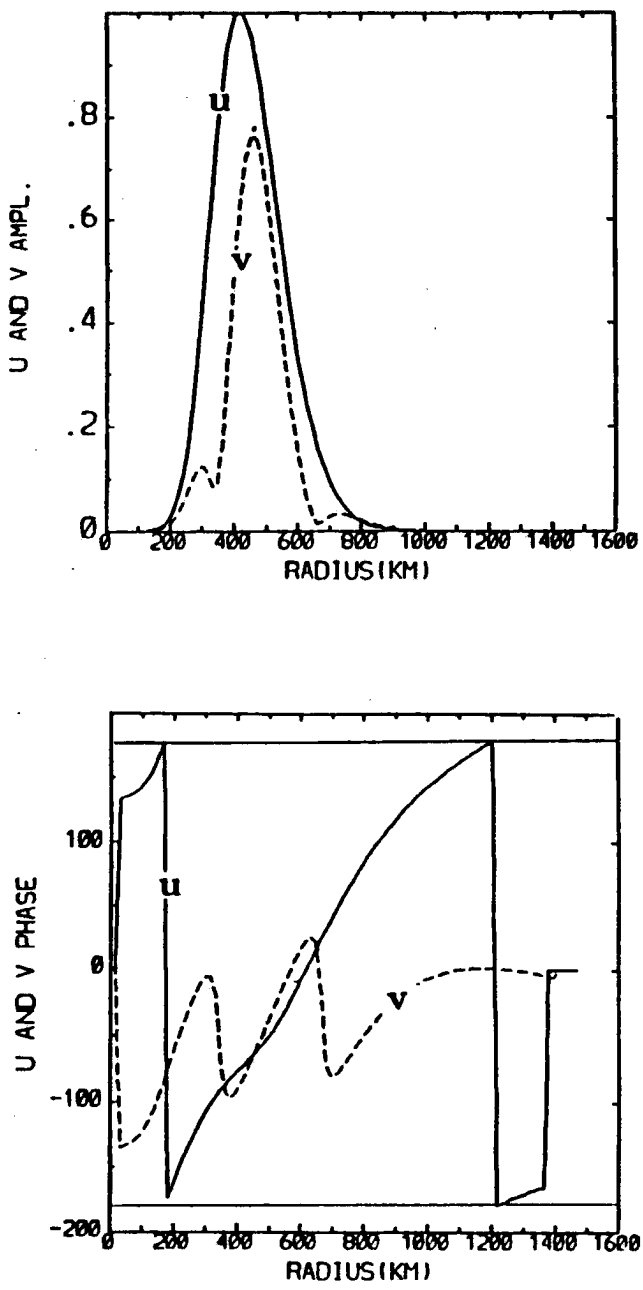

Figure 5.10: The structure of the most unstable mode for $\epsilon = 0.039$ and $h = 0.01$m

Chapter 6

DYNAMIC INSTABILITIES IN A THREE-DIMENSIONAL BAROCLINIC VORTEX

In the previous chapter, we discussed the development of dynamic instabilities in a tropical cyclone outflow layer using the shallow water model. We now extend the results of our calculations using our three-dimensional nonlinear model. The basic questions we want to answer are:

- Can the unstable modes we observed in a linear shallow water model be identified in the three-dimensional, primitive equation model?
- Can unstable modes influence the vortex dynamics and vortex motion?

6.1 Inertial instability

In three dimensions, the inertial instability condition demands that potential vorticity be less than zero in some regions. Although some numerical models can produce negative potential vorticity (Ooyama, 1969; Anthes, 1972), the assumptions of a model may not allow instabilities to develop in spite of necessary conditions for instabilities being satisfied (Ooyama, 1969). Chapter V showed that the e-folding time scale for inertial instability (specially for the most unstable, symmetric mode) strongly depends on the vertical scale. This result suggests that development of inertially unstable modes may depend on the vertical resolution of a numerical model. To test this hypothesis we use the symmetric version of the model. Eliminating asymmetries allows us to focus on inertial instability, since barotropically unstable modes are always asymmetric.

We look at the development of instabilities for the 5, 11, and 21 level versions of the symmetric model (experiments S5, S11 and S21 respectively). The model is integrated

from an initial state at rest with Newtonian friction in the lowest layer with 6 days time scale and Raleigh cooling with 10 days time scale.

In Fig. 6.1 we show the results of integration after four days of simulation. Even though all parameters except the number of vertical levels are kept the same, the winds produced by S5, S11, and S21 simulations differ. Surface winds are strongest in S5, while anticyclonic winds in the outflow layer have the larger maximum value in S21. The differences in tangential wind are due to the fact that development of the cyclone in a numerical model depends on vertical distribution of diabatic heating (Hack and Schubert, 1986). Even though in all cases the diabatic heating is given by the same analytical formula, the difference in resolution places the maximum heating on slightly different levels. In addition, the crude vertical resolution in S5 "smooths out" the angular momentum contours in S5 (Fig. 6.1). As a result, even though after four days of integration negative potential vorticity (Q) appears in all three experiments, the value of negative Q in S5 is much smaller than in S11 and S21 and occupies a very small area. The absolute values of negative Q are largest in S21. In addition, S21 allows perturbations with relatively small vertical scale and therefore we can expect instabilities to occur first in this version. Indeed, the 21 level version becomes unstable after 6 days of integration (Fig. 6.2). The instability appears in the region where potential vorticity was negative at day 4 and has the smallest vertical scale allowed by the vertical resolution of the model. The negative potential vorticity region moves toward larger radii. There is further development of negative Q for S5 and S11. After 8 days of integration (Fig. 6.3) the 11-level model becomes inertially unstable. Unstable modes do not appear in the 5-level model, although by eigth day of integration, the negative potential vorticity in S5 reaches the values much larger than negative Q in S11.

These results show that development of inertially unstable modes is very sensitive to vertical resolution of the numerical model.

It is still not clearly established how the inertial instability in the outflow layer influences the dynamics of a tropical cyclone. Alaka (1962), following Sawyer (1947), suggested that symmetric inertial instability can initiate intensification of a tropical cyclone. It is

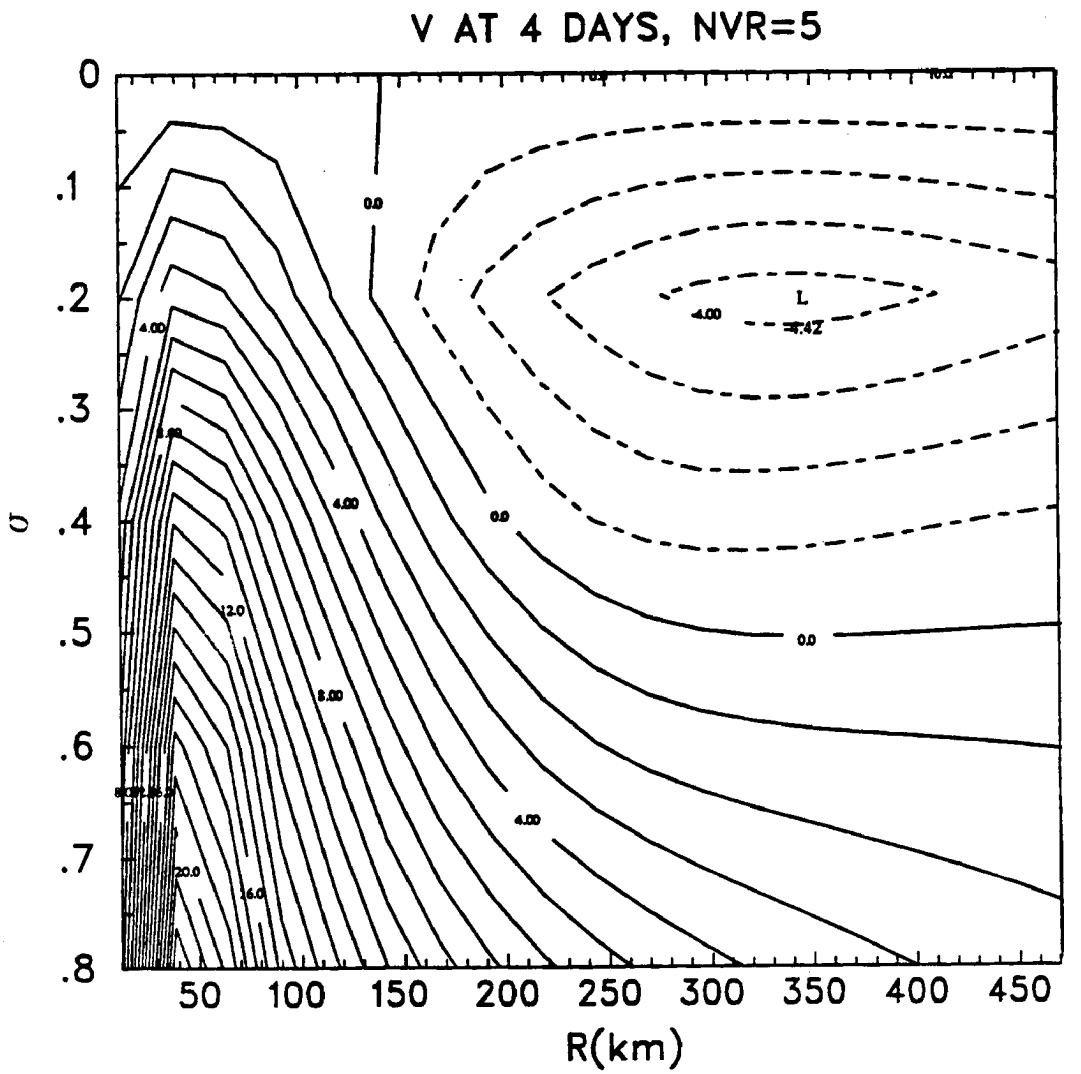

Figure 6.1: Tangential wind and angular momentum after 4 days of integration; Shading denotes the area where potential vorticity is negative. a)Tangential wind in S5

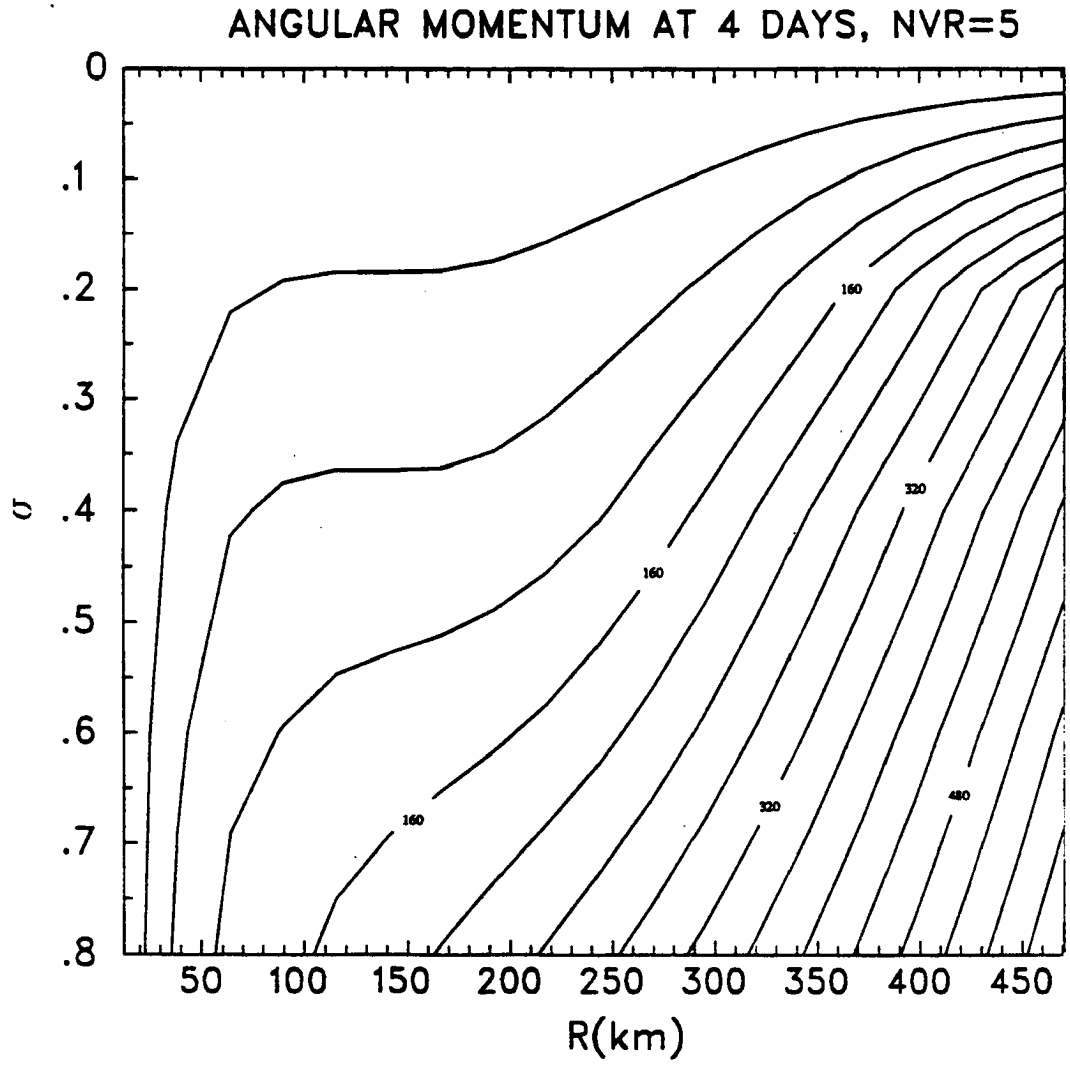

Figure 6.1: continued. b)Angular momentum in S5

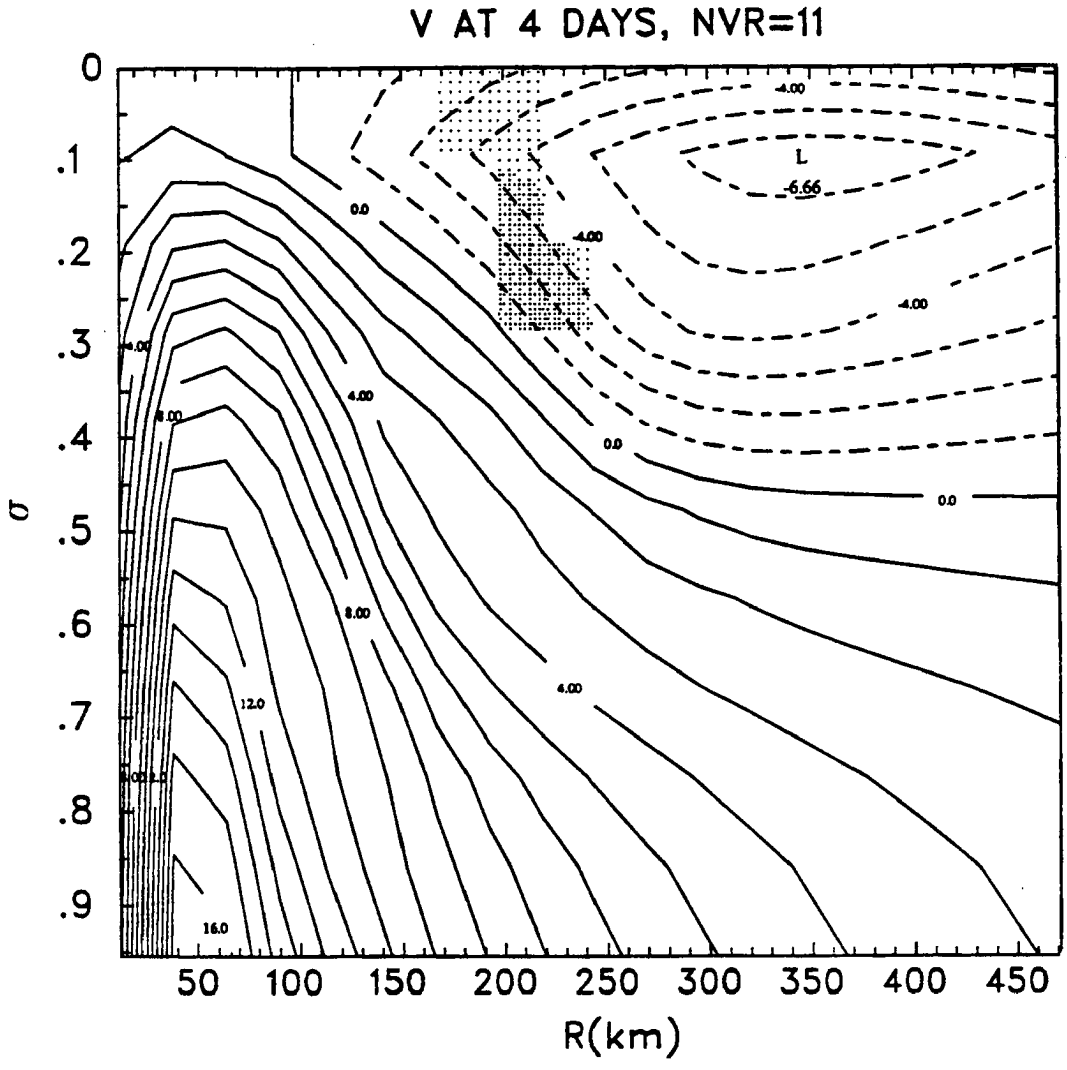

Figure 6.1: continued. c)Tangential wind in S11

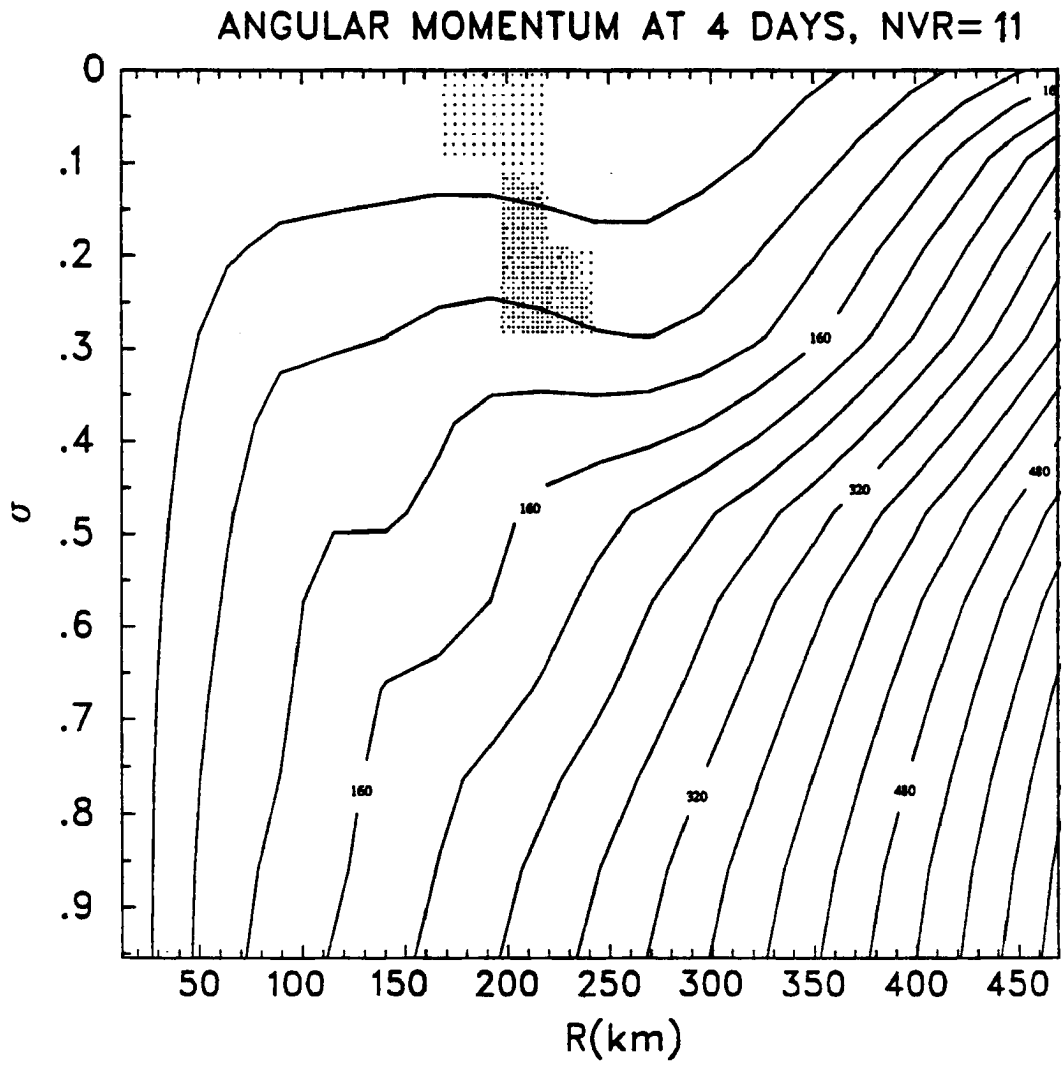

Figure 6.1: continued. d)Angular momentum in S11

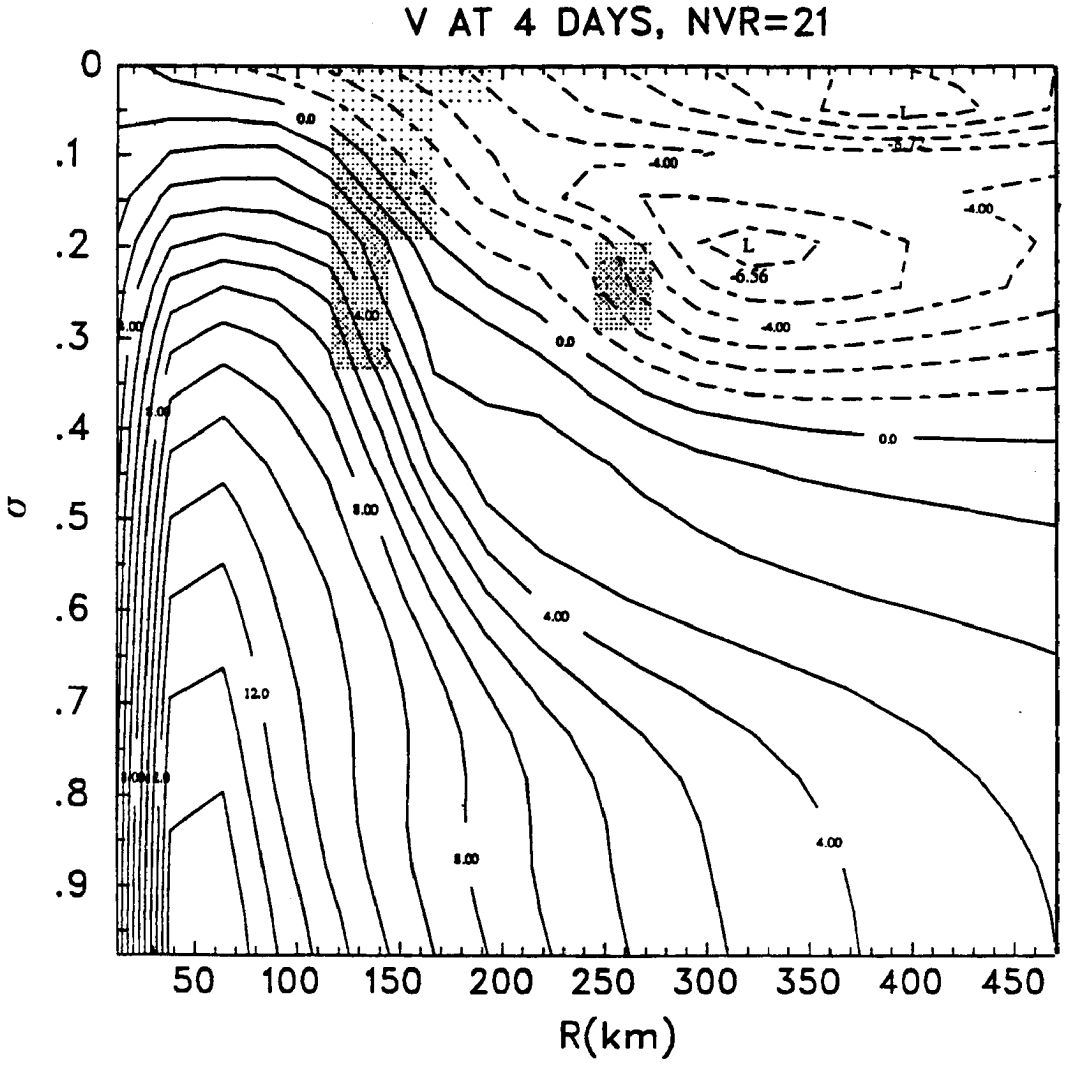

Figure 6.1: continued. e)Tangential wind in S21

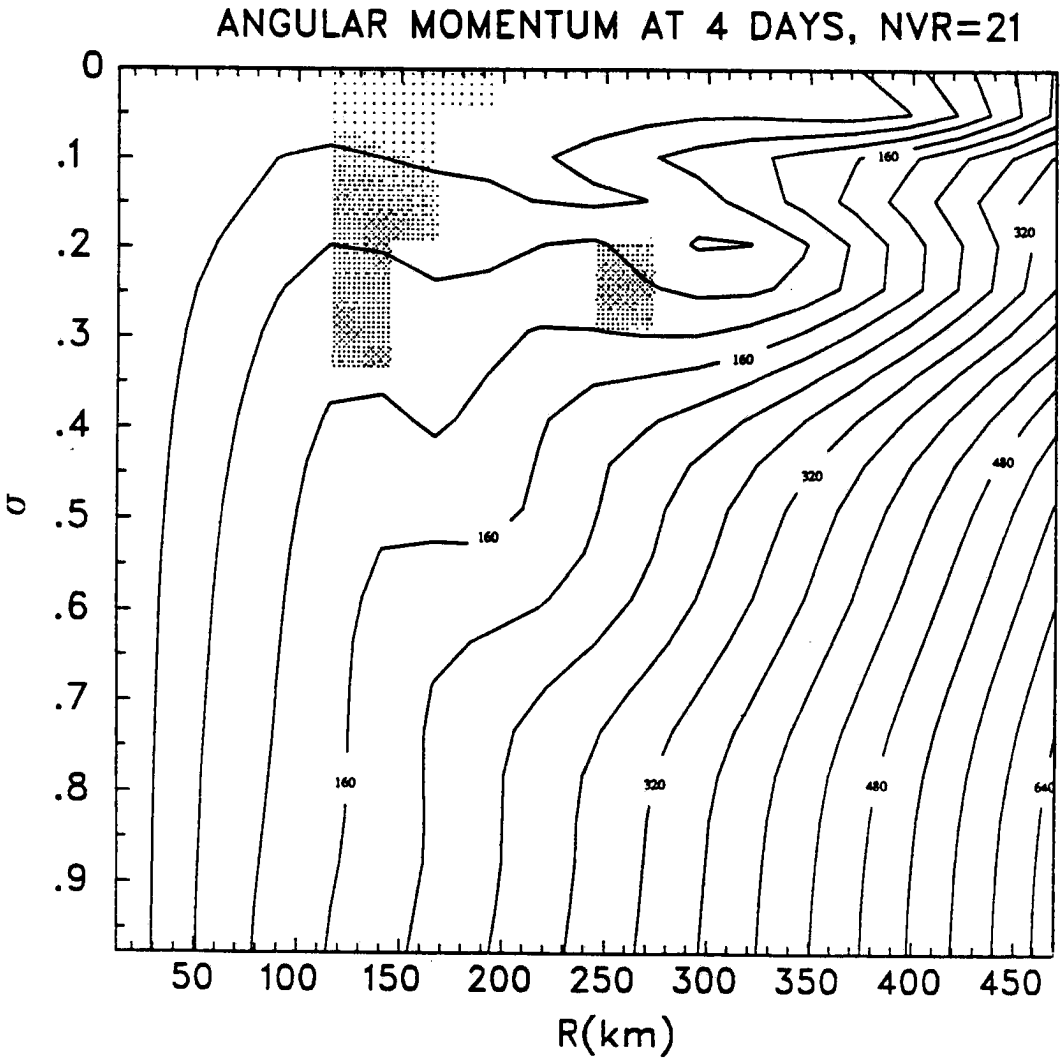

Figure 6.1: continued. f)Angular momentum in S21

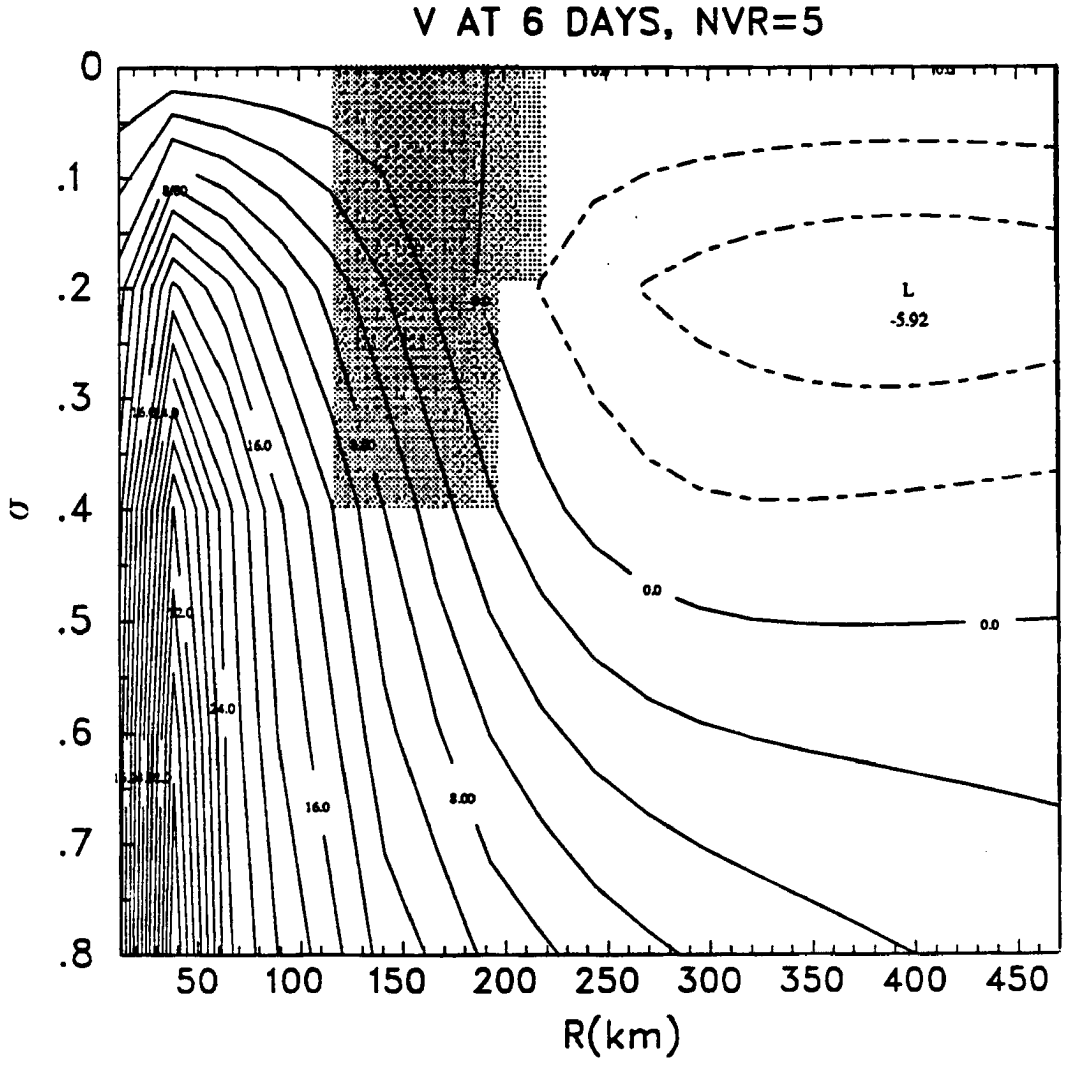

Figure 6.2: Tangential and radial wind after 6 days of integration; Shading denotes the area where potential vorticity is negative. a)Tangential wind in S5

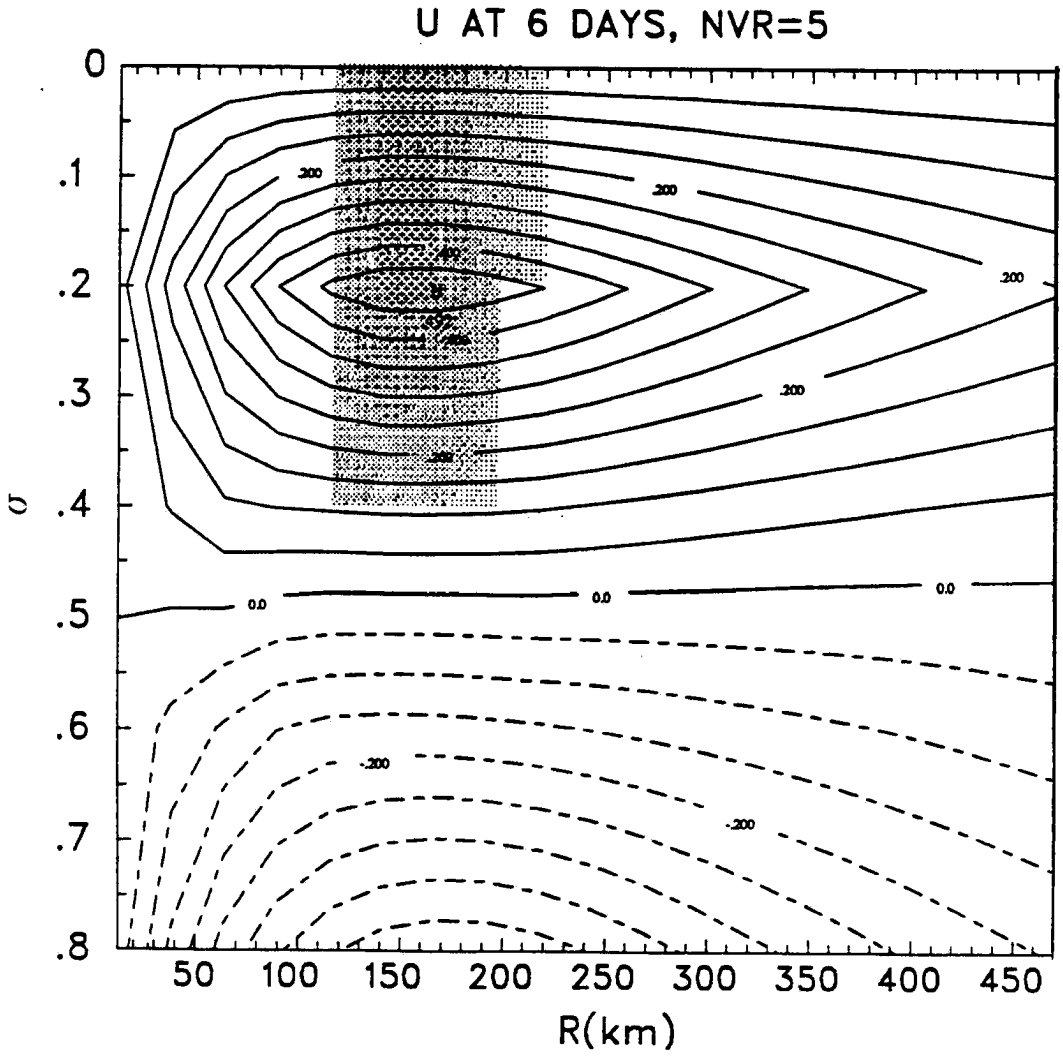

Figure 6.2: continued. b)Radial wind in S5

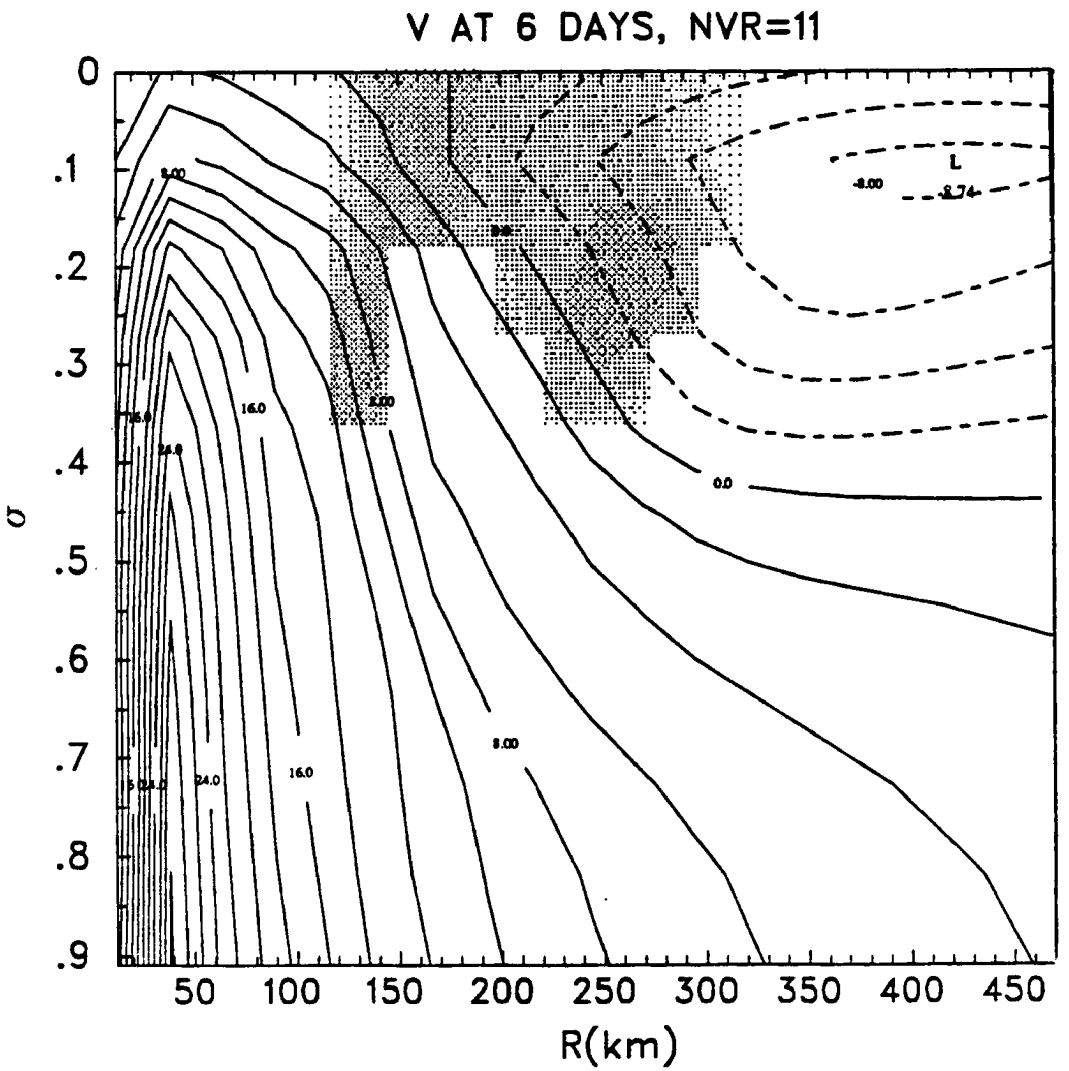

Figure 6.2: continued. c)Tangential wind in S11

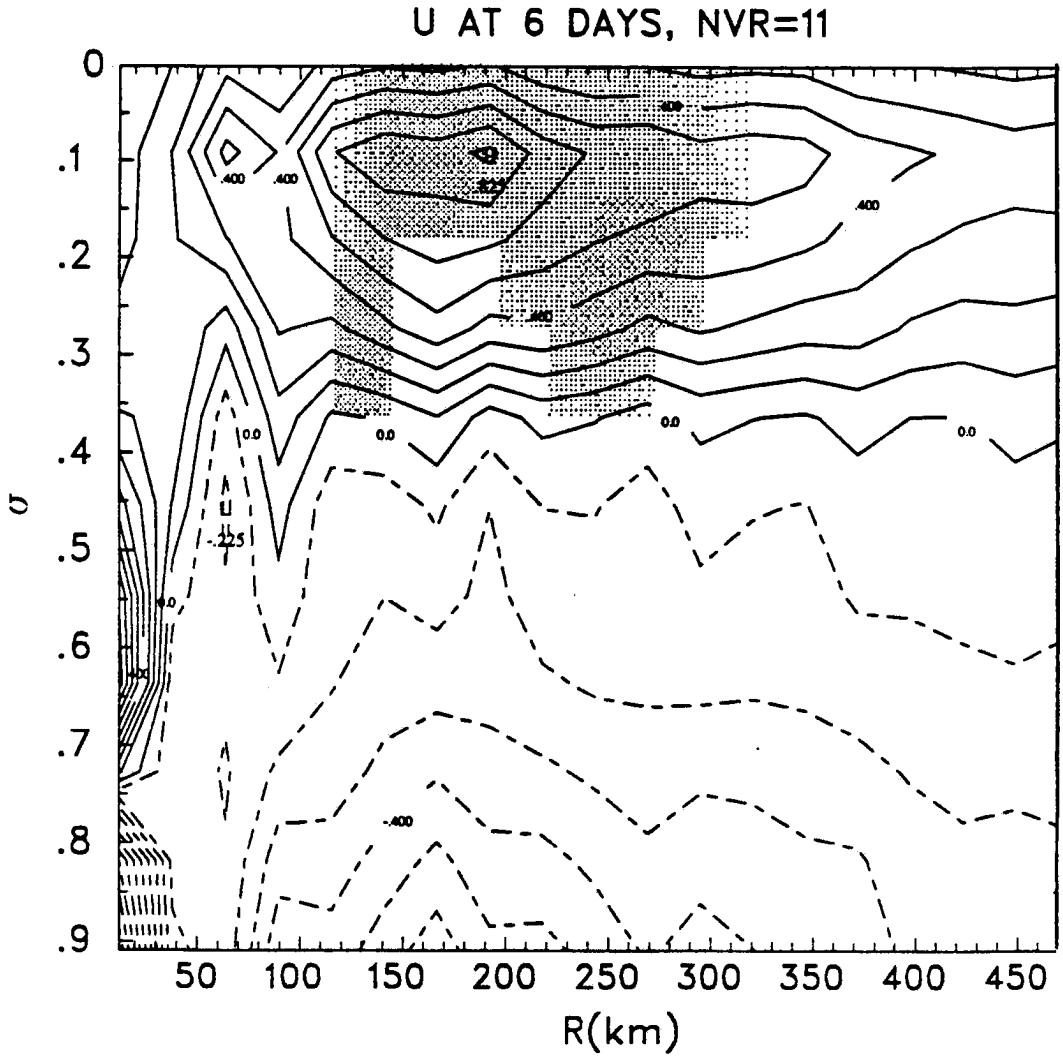

Figure 6.2: continued. d)Radial wind in S11

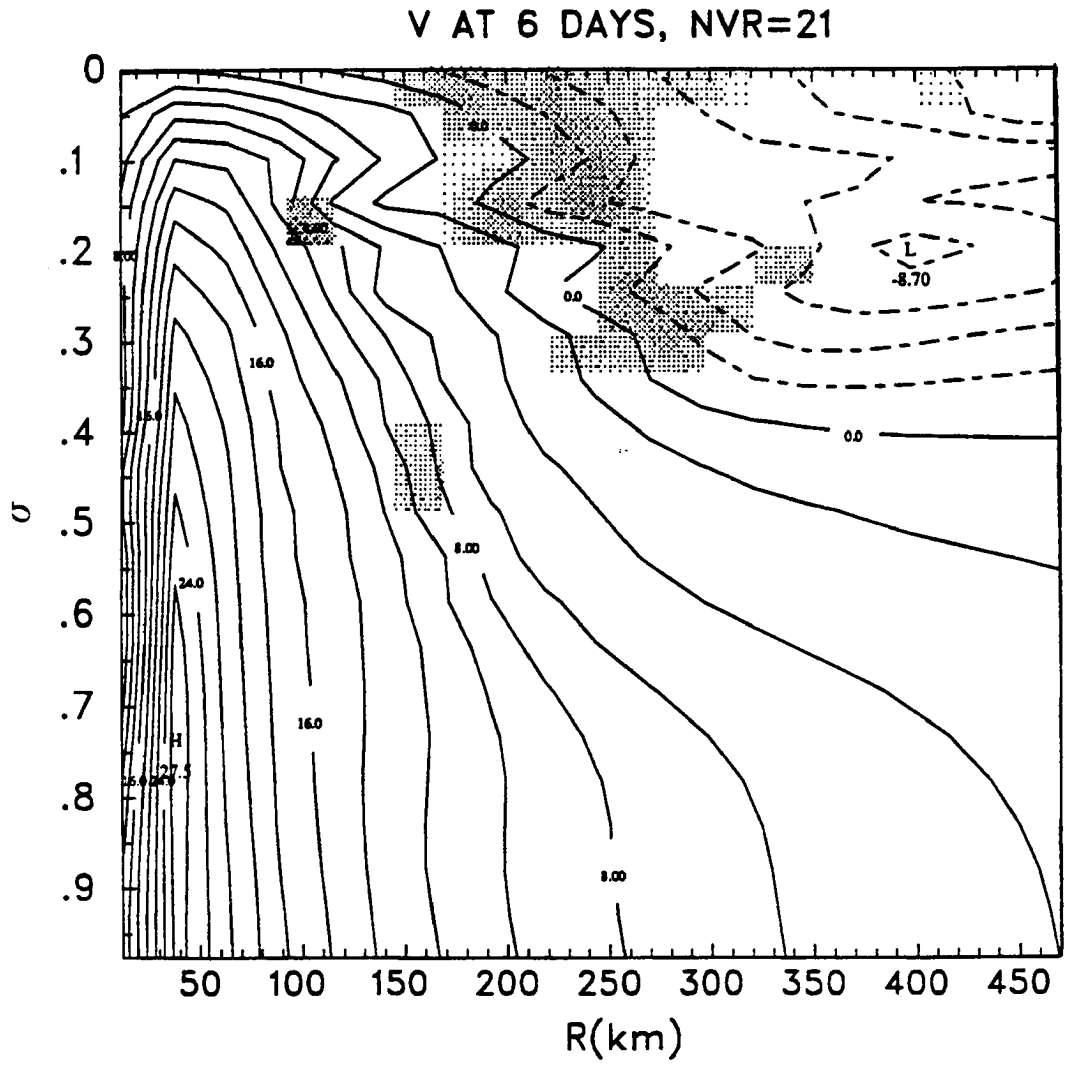

Figure 6.2: continued. e)Tangential wind in S21

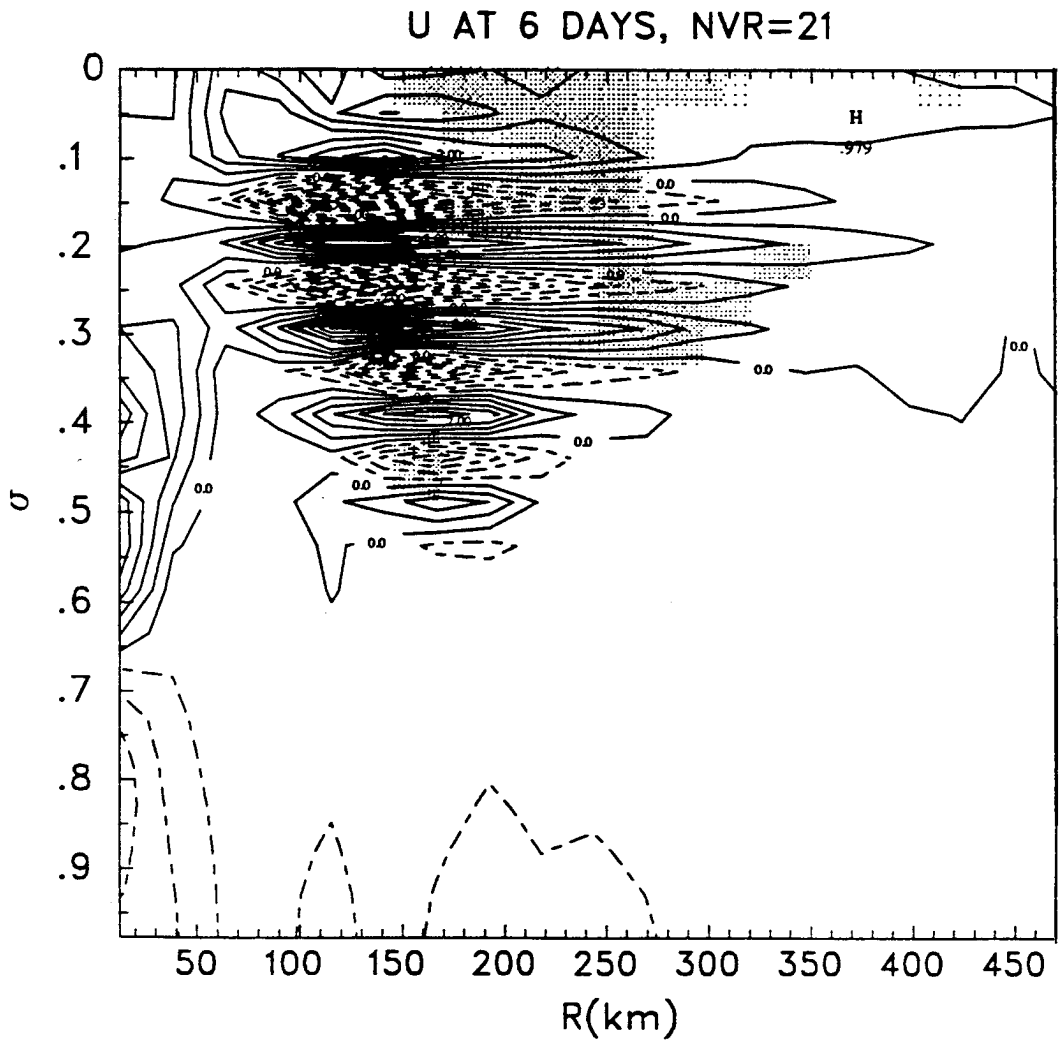

Figure 6.2: continued. f)Radial wind in S21

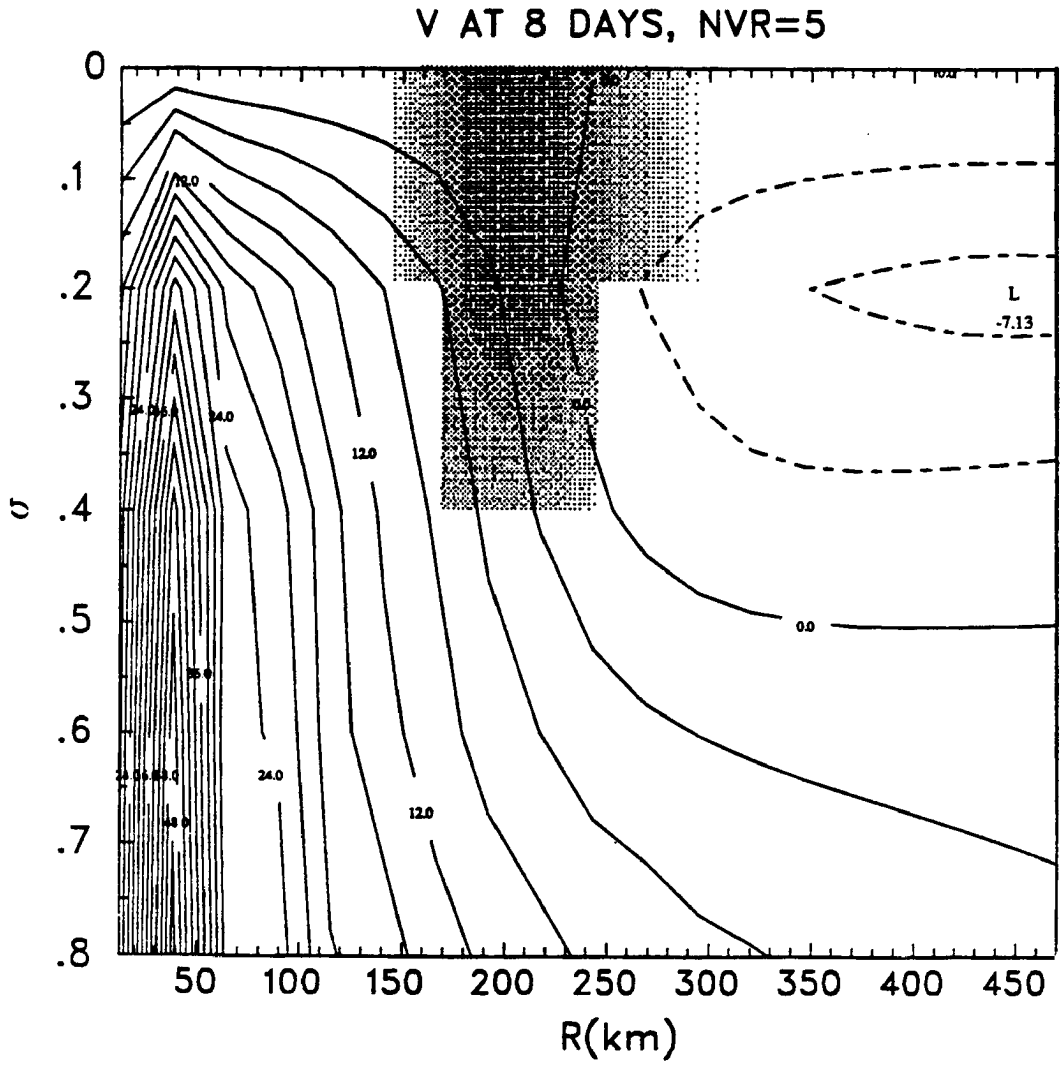

Figure 6.3: Tangential and radial wind after 8 days of integration; Shading denotes the area where potential vorticity is negative. a)Tangential wind in S5

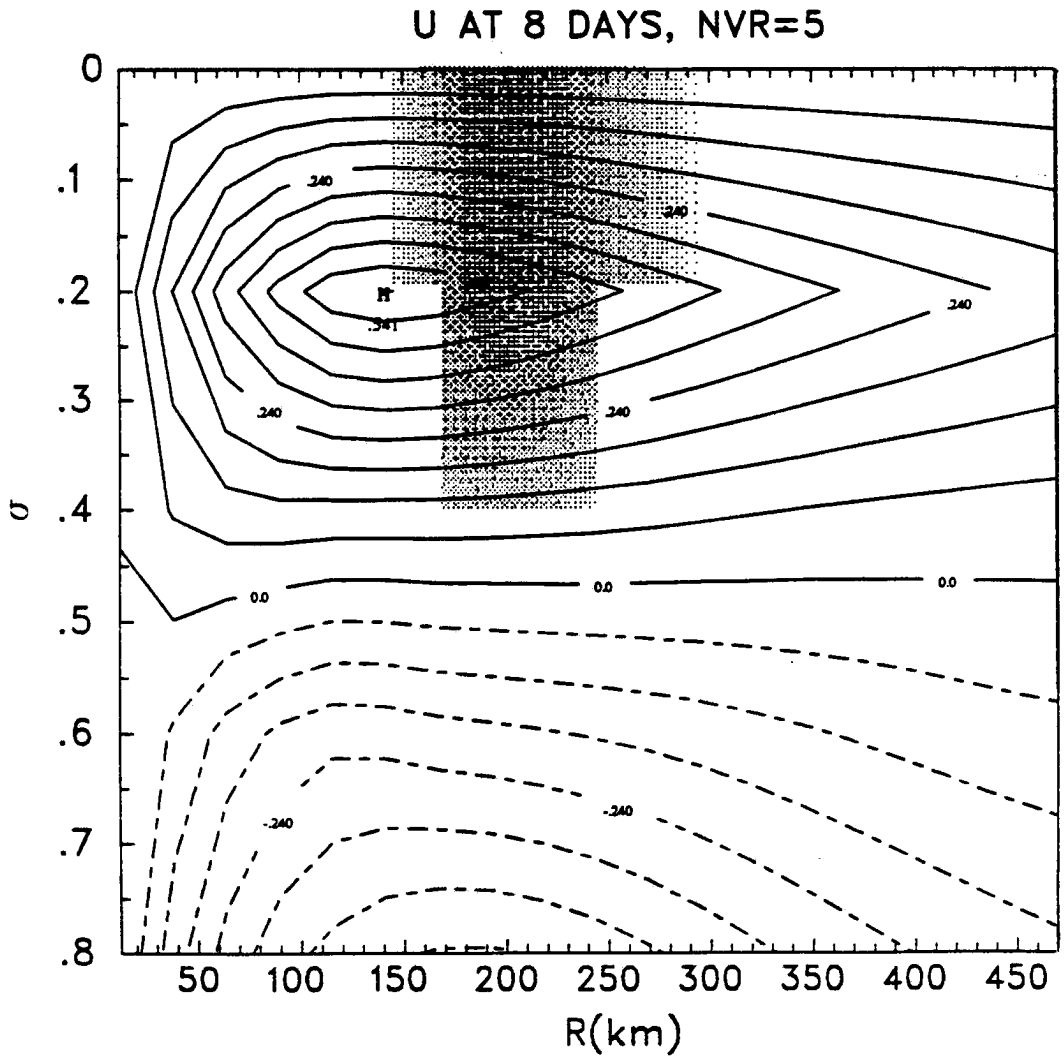

Figure 6.3: continued. b)Radial wind in S5

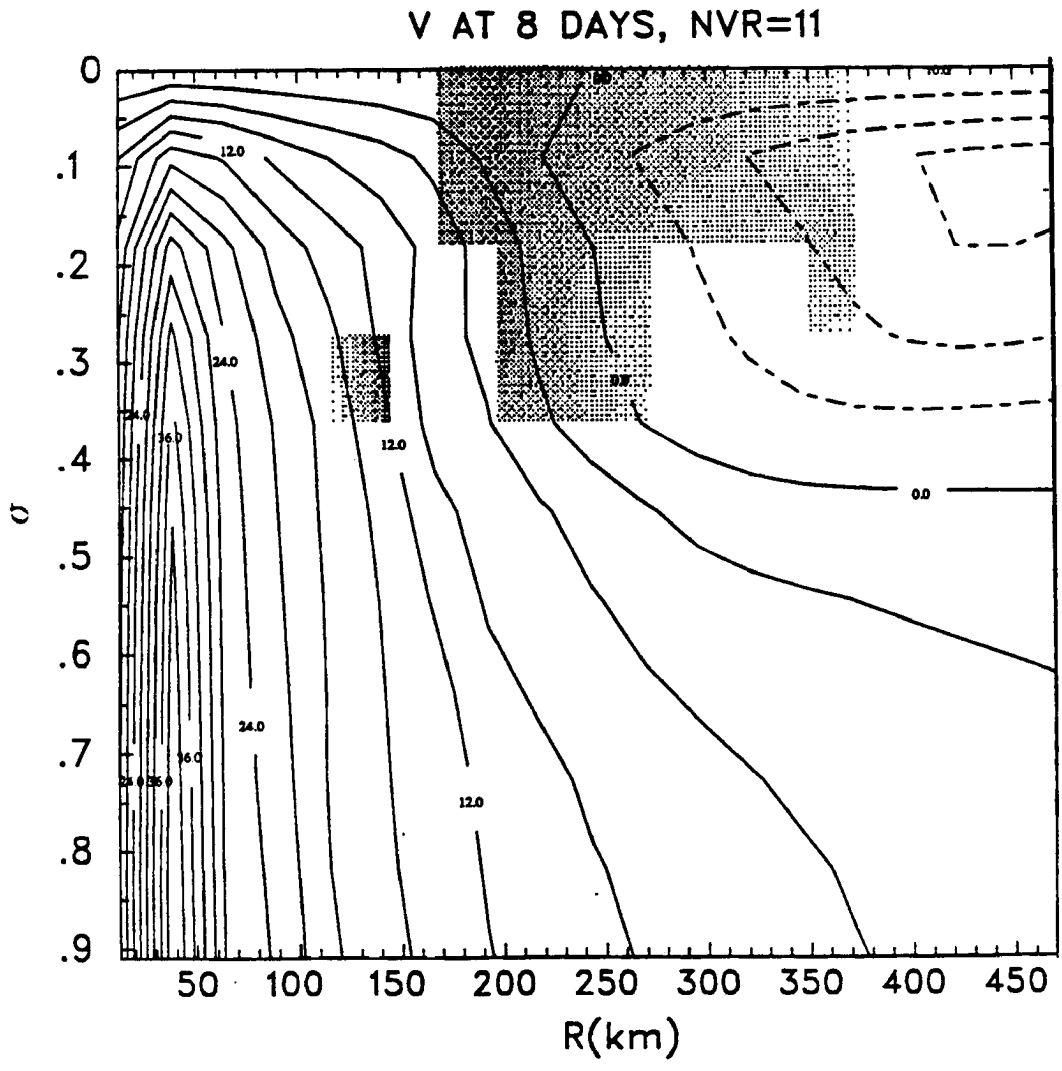

Figure 6.3: continued. c)Tangential wind in S11

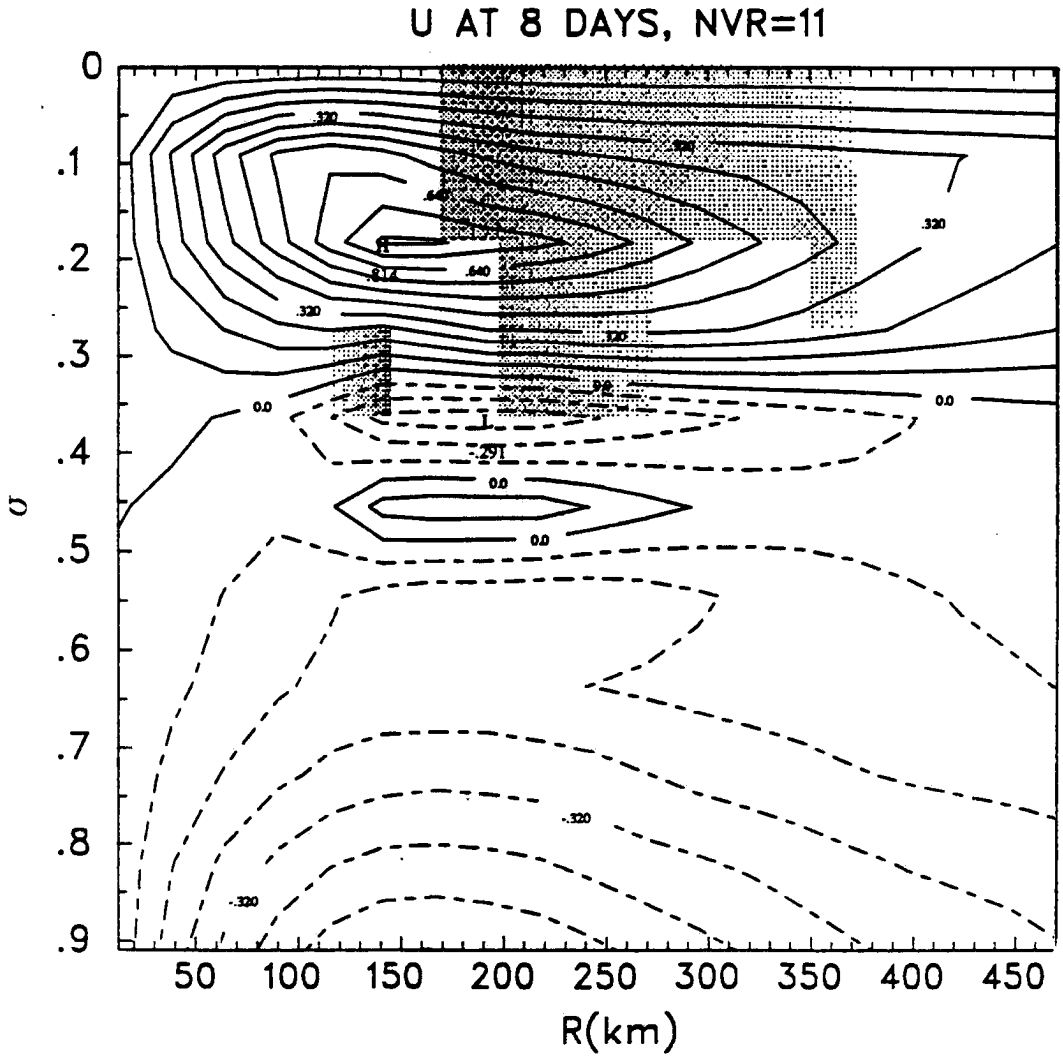

Figure 6.3: continued. d)Radial wind in S11

now believed (Ooyama, 1987) that inertial instability is the result rather than the cause of cyclone intensification. In our calculations there is also no indication of faster intensification connected with instability. On the contrary, surface pressure starts to rise after circulation identified with inertial instability develops. However, there are other processes in tropical cyclones in which inertial instability can play a role. Willoughby *et al.* (1984) suggest inertial instability as a mechanism for initiating convective rings in hurricanes. He speculates that even though the unstable modes are confined to the region where the instability condition is satisfied (that is, usually to the upper troposphere), they can induce ascending motion in the lower troposphere which in turn can give an impulse to convection. Our results show that proving this hypothesis using a numerical model can be difficult. If the resolution of the model is too crude, the absence of stabilizing small scale motions can cause unrealistic growth of the inertially unstable area. As a result, inertially unstable modes which finally develop in the model can have larger scale and growth rates than inertially unstable motion in the real atmosphere.

In models with low vertical resolution, symmetric modes will not develop at all. However, asymmetric modes can appear. Development of inertially unstable modes with $s = 1$ structure depends on the tangential wind profile. When the anticyclonic wind in the outflow layer is strong, (Fig. 5.9) the growth rates for asymmetric modes are close to these for symmetric modes. When the tangential wind is smaller, the growth rates for asymmetric mode decay, with increasing vertical scale, much slower compared with growth rates for symmetric modes. It is therefore possible that in that case some inertially unstable modes can develop in a numerical model with low vertical resolution. However, when the resolution of the model is low, it may be difficult to determine if the unstable, asymmetric mode is caused by barotropic or inertial instability. In the previous chapter we have shown that the modes which can be clearly identified as barotropic have maximum amplitude at the vortex center, while those due to inertial instability have maximum amplitude in the region where the condition for instability is satisfied. Figure 6.4 shows the most unstable mode for different vertical equivalent depths. It can be seen that for intermediate equivalent depths, the most unstable mode does not have clearly barotropic or inertial instability structure.

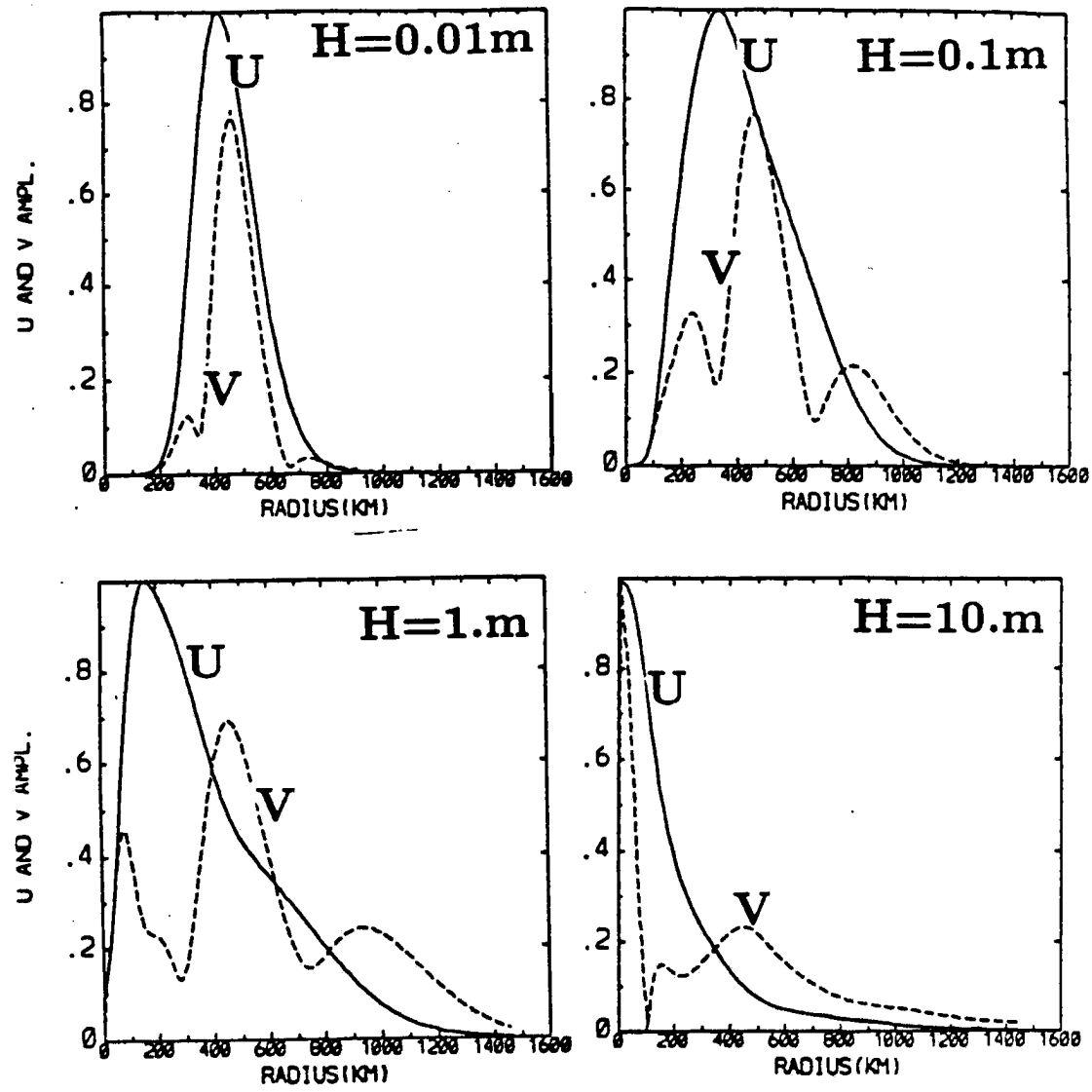

Figure 6.4: The structure of the most unstable mode as a function of equivalent depth h in the shallow water model.

In the next set of experiments we will use the five-level model. Since the five-level model can resolve only relatively large vertical scales of motion, we will assume in our further discussion that asymmetric unstable modes are due to barotropic instability.

6.2 Barotropic instability - the influence of asymmetric modes on the vortex motion

As we have shown in the previous chapter, the barotropically unstable mode has the largest growth rates for azimuthal wavenumber $s = 1$ with maximum perturbation at the vortex center. It is therefore probable that it can influence the movement of the vortex. Examples of such influence can be seen in one-level models. Willoughby (1988) observed the sudden change in calculated vortex movement if the frequency of the forcing matched the maximum anticyclonic angular velocity in the vortex. Peng and Williams (1990) noticed the presence of the rotating gyres close to the vortex center. The streamfunction for these perturbations was similar to what we obtained for the barotropically unstable mode with $s = 1$ zonal wavenumber. In one-layer models the mean flow usually satisfies the barotropic instability conditions because of the existence of anticyclonic circulation at large radii. The presence of anticyclonic circulation at the vortex periphery is the consequence of the demand that total relative angular momentum of the vortex L_R is equal to zero. As shown by DeMaria (1987), assuming that L_R=0 for the initial vortex (i.e., an isolated vortex) reduces the errors in numerical prediction of hurricane movement based on a barotropic model.

Such a condition is not necessary in a three-dimensional model where anticyclonic flow in the upper layer balances the cyclonic flow in the lower layers. In three-dimensional models as well as in reality (e.g., Merrill, 1985) the condition for barotropic instability is satisfied in the upper troposphere. Therefore, one can ask to what extent processes in the upper troposphere can influence the motion. Some models (Anthes, 1972) show that appearance of dynamically unstable flow in upper layers, followed by development of an asymmetric structure in that layer, coincides in time with a meandering motion of the cyclone. Therefore the looping motion of a cyclone is sometimes explained in terms of flow instabilities. Additionally, Holland (1988) suggests that development of barotropically

unstable modes, triggered by approaching midlatitude trough, can affect recurvature of a cyclone.

6.3 Description of numerical experiments

In the numerical experiments described below, we examine how the development of dynamic instabilities and the subsequent changes in the cyclone motion depend on the intensity of an initial vortex and the form of the environmental forcing. A series of numerical experiments are carried out for two types of vortices. Vortex A has large tangential velocities (V_{max}=30m/s) and satisfies the criteria for barotropic (potential vorticity gradient reversal on isentropic surface) and inertial (negative potential vorticity) instabilities in the upper layers (Fig.6.5). There is a region with negative potential vorticity located near 200 km radius in the middle and upper layers. The vorticity gradient changes sign in this area. The reversal of potential vorticity gradient can be also observed in the upper layers (300 - 200 mb) at about 550 km radius. The tangental velocity plots indicate that angular velocity near the radii where potential vorticity changes sign, is equal to about $-1.2 \times 10^{-5}s^{-1}$ for the radius of 550 km. Since another potential vorticity minimum extends from about 500 mb to 200 mb, the angular velocity at this radius depends on the level. It is equal to about $1. \times 10^{-5}s^{-1}$ on 300 mb and $4 \times 10^{-5}s^{-1}$ on 500 mb. Vortex B has small (V_{max}=10m/s) tangential velocity and is inertially stable. There is a region of potential vorticity reversal at about 250 km from the center. The angular velocities at this radius are rather small — $7.5 \times 10^{-6}\mathrm{s}^{-1}$ — corresponding to periods of about 230 hours (9.6 days). We consider two types of environments. In the first type we assume that an asymmetric wind field is superimposed on the initial vortex. The initial wind field is uniform in space and consists of easterly wind with $U = -1$m/s. Another way of defining the environmental influence is to include in the governing equations an additional term representing an environmental momentum forcing. The forcing term is used only in upper layers. The forcing acts only in the x-direction so it can either speed up or slow down the zonal flow. This term is either horizontally uniform (experiment III) or has the Gaussian distribution (experiment IV, V and VI) with maximum amplitude at $r_B = 500$ km, that

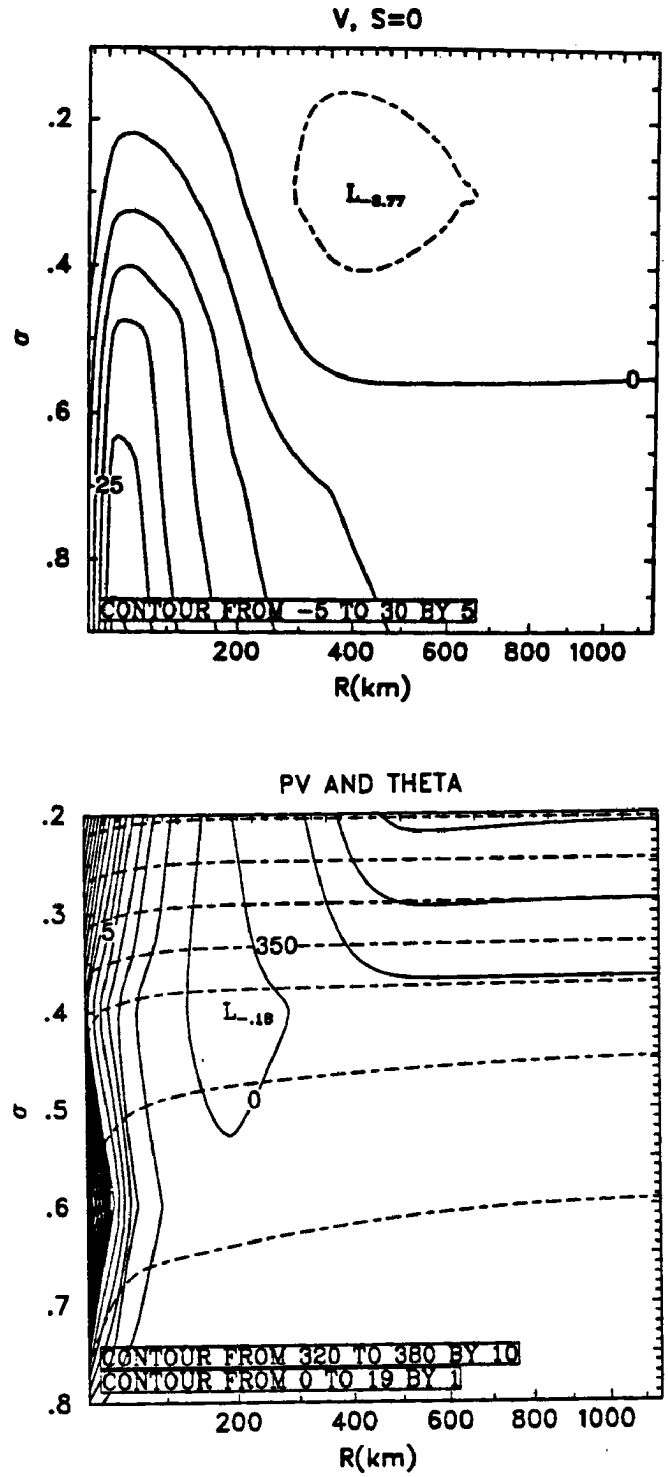

Figure 6.5: Initial symmetric vortices — tangential wind, potential vorticity and potential temperature (dashed lines) a) the strong vortex (vortex A)

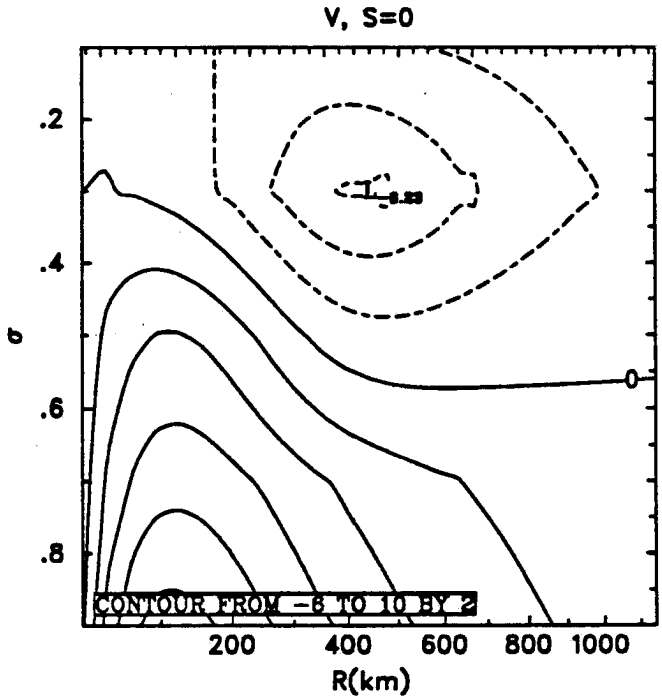

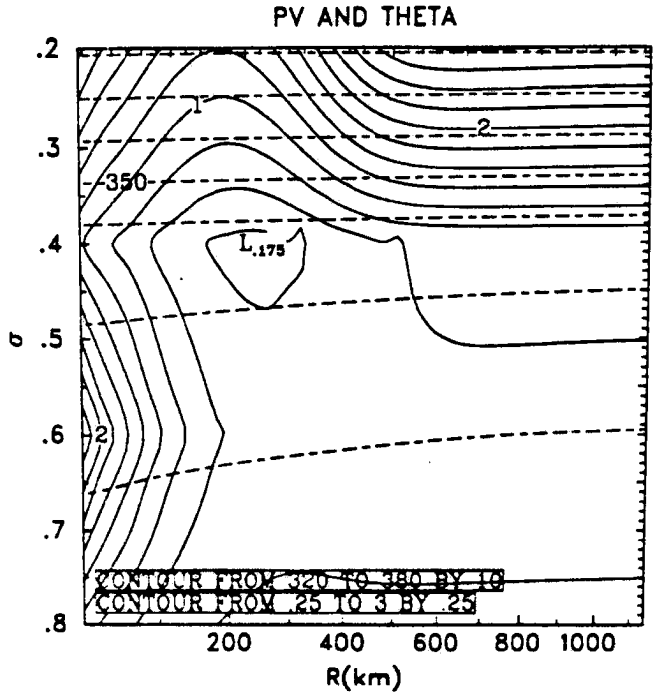

Figure 6.5: continued. b) the weak vortex (vortex B)

Table 6.1: List of experiments

Experiment	Vortex	Initial wind	Forcing
I	B	$u = -1$m/s	0
II	A	$u = -1$m/s	0
III	A	$u = -1$m/s	uniform, T=T_{Bar}=140h
IV	A	u=0	at 500 km, T=12.5 h
V	B	u=0	at 500 km, T=140 h
VI	A	u=0	at 500 km, T=140 h

is in the vicinity of the region where the condition for barotropic instability is satisfied ($\partial Q/\partial r = 0$ at $r = r_B$). The forcing can vary with time with different frequencies. One frequency corresponds to the period of 12.5 hours and is not connected with any special dynamic properties of the system. Another frequency with the period of $T = T_{Bar} = 140$ hours is equal to the frequency of the unstable barotropic mode. In our shallow water model, we found that the critical radius on which the frequency of the unstable mode was equal to angular velocity was located near the radius where the potential vorticity gradient changed sign. Therefore, for the purpose of this calculation we estimate the frequency of the most unstable mode as angular velocity of the flow at $r = r_B$.

The experiments are listed in Table 6.1.

Since barotropic instability develops slowly, the model is integrated for 8 days.

6.3.1 Motion in a steady environmental flow

Figs 6.6 and 6.7 shows the vortex tracks and meridional vortex velocities for experiments I and II.

In a steady 1 m/s flow, both vortices experience the cyclonic looping motion with amplitudes of about 100 km. The velocity diagram (Fig 6.7) indicates that trochoidal oscillations develop early in the weak vortex, while the strong vortex for about 80 hours moves with the environmental flow. The maximum amplitude of oscillations is slightly larger for the strong vortex, but it decays rapidly at about 150 hours. The power spectrum of kinetic energy of the vortex movement for these experiments is shown in Fig. 6.8. It can be seen that both vortices experience cyclonic oscillations with relatively short periods

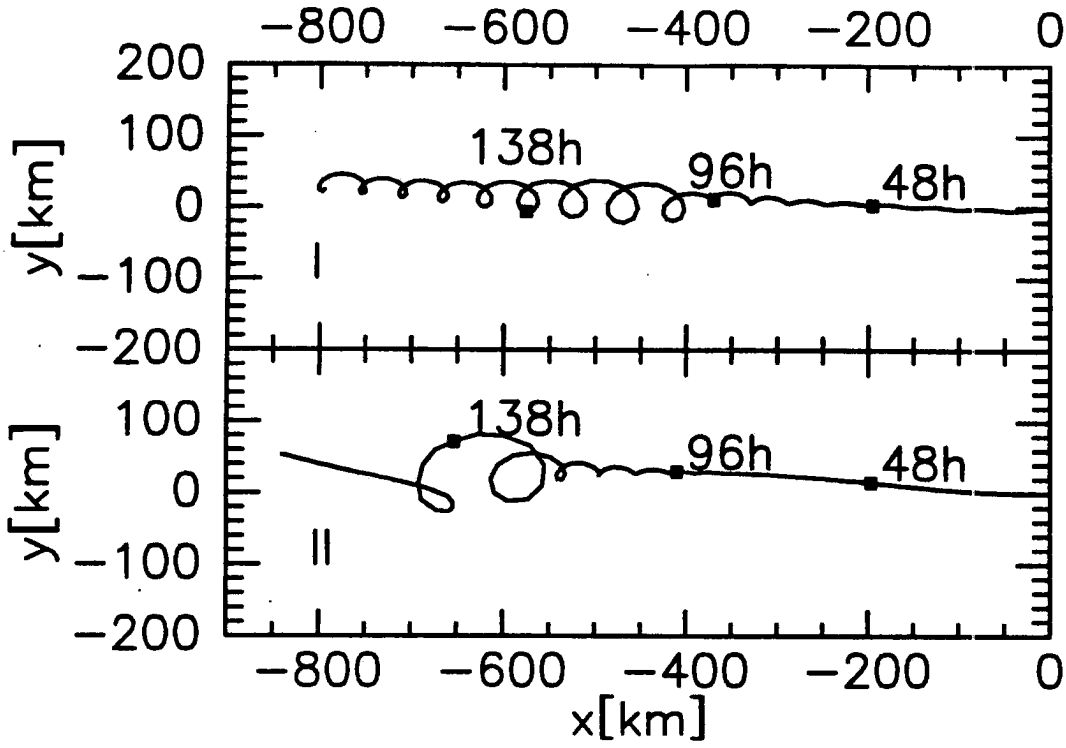

Figure 6.6: Vortex track for weak (exp. I) and strong (exp. II) vortex in uniform environmental wind field u=-1m/s.

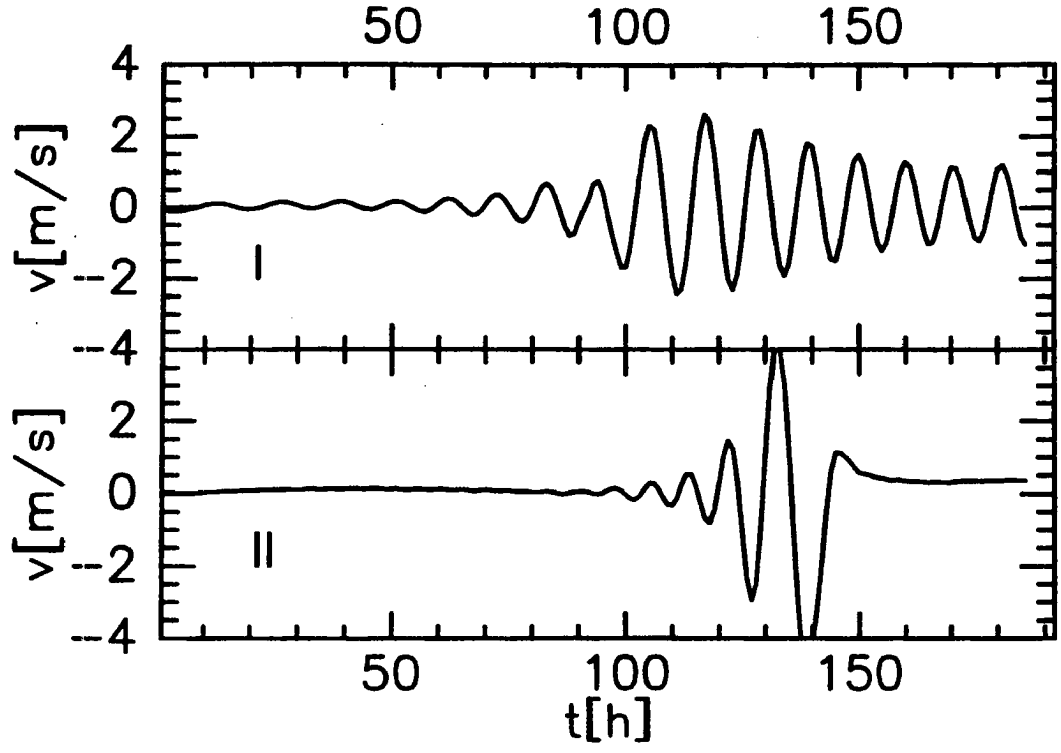

Figure 6.7: Meridional vortex velocity for weak (exp. I) and strong (exp. II) vortex in uniform environmental wind field u=-1m/s.

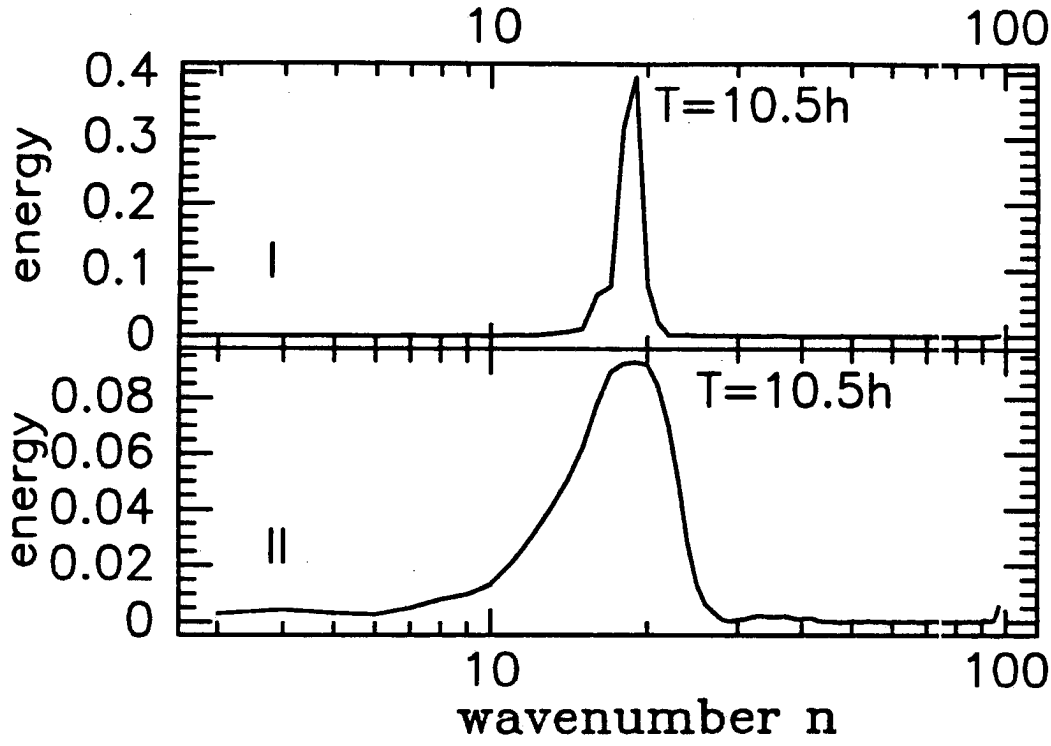

Figure 6.8: Power spectrum for the weak (exp. I) and strong (exp. II) vortex. The energy is normalized to the total kinetic energy of the vortex motion. The wavenumbers are plotted on logarithmic scale. The frequency of the mode with wavenumber n is equal to $\omega_n = 2\pi n/L$ where L=8 days.

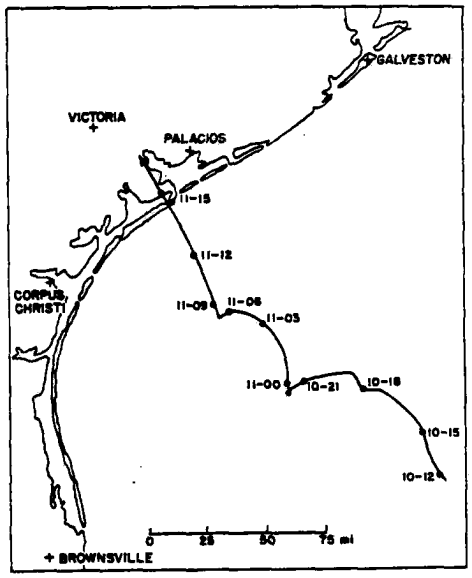

Figure 6.9: Track of hurricane Carla (from Jordan, 1966)

(8-9 hours). The periods of these oscillations are much smaller that the periods of possible barotropic oscillations in vortices A and B. The looping motion with similar periods and amplitudes of a few tens of kilometers can be sometimes observed in real cyclones (Fig. 6.9). They were also seen in other three-dimensional numerical models of tropical cyclones (e.g., Kitade, 1980). This type of oscillation is not connected with dynamical instabilities but can be explained as a result of hydrodynamic forces acting on the vortex in solid rotation moving in a uniform flow. The mechanism of such oscillations was described by Yeh (1950) and Kuo (1960). If the vortex moves in the uniform zonal flow with velocity U, its path can be described by the equations:

$$\begin{aligned} x &= A\cos(\omega t + \epsilon) + Ut \\ y &= A\cos(\omega t + \epsilon) \end{aligned} \tag{6.1}$$

According to Yeh, the period $T = 2\pi/\omega$ of the oscillations depends only on the characteristics of the vortex (small and intense vortices oscillate more rapidly than large weak vortices). The amplitude of oscillation A is proportional to the period T and the difference between the velocity of the vortex relative to the basic flow. The power spectrum (Fig. 6.8) shows that, contrary to Yeh (1950), calculated periods of oscillations are similar for the strong and weak vortex. We have to remember, however, that in Yeh's calculations

the air inside certain radius R is assumed to move with the vortex. This assumption may not be valid, especially for the weak vortex. The very sharp and narrow peak in the power spectrum of the weak vortex indicates that for the weak vortex this is the sole internal mechanism responsible for looping. There is no energy in the low-frequency modes. In the real atmosphere, the situation is of course much more complicated because of the influence of the environment and asymmetries of convective heating.

For the strong vortex the power spectrum is much broader. Even though cyclonic looping dominates, there is a small peak near the frequency of $-1.2 \times 10^{-5} s^{-1}$ corresponding to barotropic instability (it is difficult to see it on the power spectrum diagram, but it can be noticed in the data). Our goal is to find out if there is a forcing which excites oscillations with this frequency. Because the phase speed for the barotropically unstable modes is negative, such oscillations could be responsible for anticyclonic turning of the vortex. As shown by Holland (1991) and Xu and Gray (1982), both cyclonic and anticyclonic looping motion is observed in tropical storms.

6.3.2 Motion with environmental forcing

To excite the barotropically unstable modes, we repeat the experiment II adding environmental forcing which is horizontally uniform and oscillates with the period of barotropically unstable modes T_{Bar}=140 hours (exp. III). Even though the forcing is relatively slow, the power spectrum for this case is even more concentrated, with maximum near T=8.5 hours period (Fig. 6.10). The cyclonic loops appear earlier than in the steady flow case and do not decay after 6 days (Fig. 6.11). We do not see any amplification of the barotropically unstable mode. The situation is different, however, when the model is initialized with no environmental wind and the forcing is concentrated near the critical radius (Experiment IV). The forcing has a form of Newtonian nudging, and Gaussian horizontal distribution:

$$F_c = -(U - U_c)/T_c \exp(-(r - r_c)^2/{r_w}^2) \cos(\omega t) \tag{6.2}$$

where U is a zonal flow, U_c=-1 m/s, time scale T_c=6 h r_c = 500 km , r_w =200 km and frequency $\omega = 1.2 \times 10^{-4} s^{-1}$ ($T = 14h$). Therefore, there is only a very weak forcing of

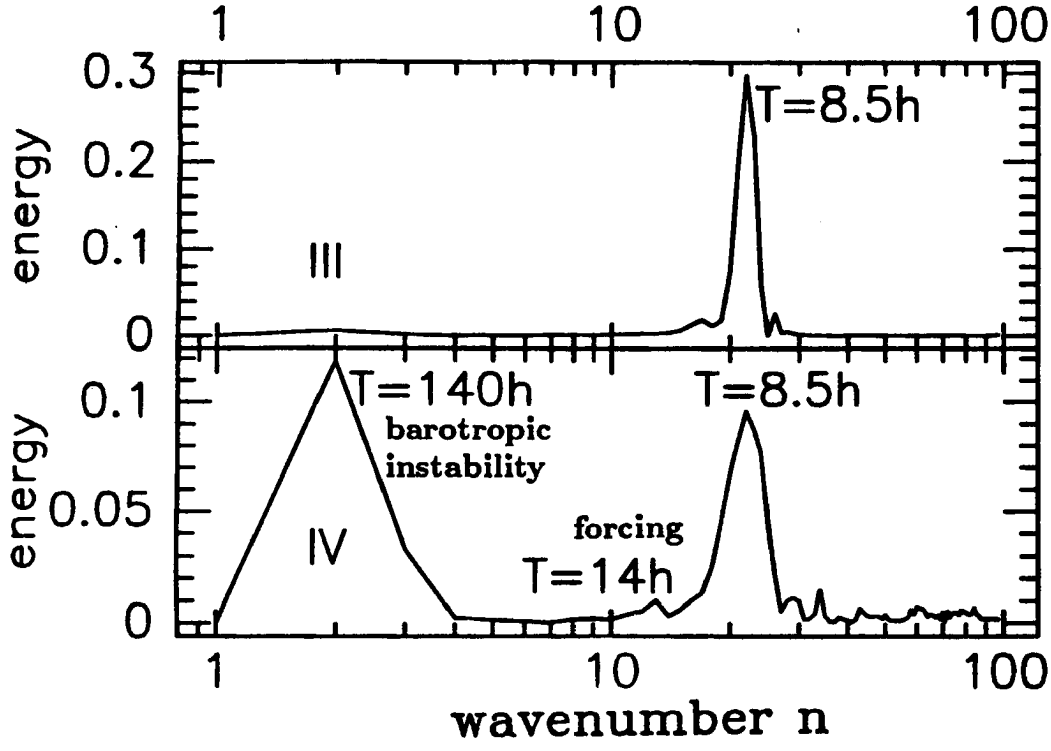

Figure 6.10: Power spectrum for experiment III and IV. The energy is normalized to the total kinetic energy of the vortex motion. The wavenumbers are plotted on logarithmic scale. The frequency of the mode with wavenumber n is equal to $\omega_n = 2\pi n/L$ where L=8 days.

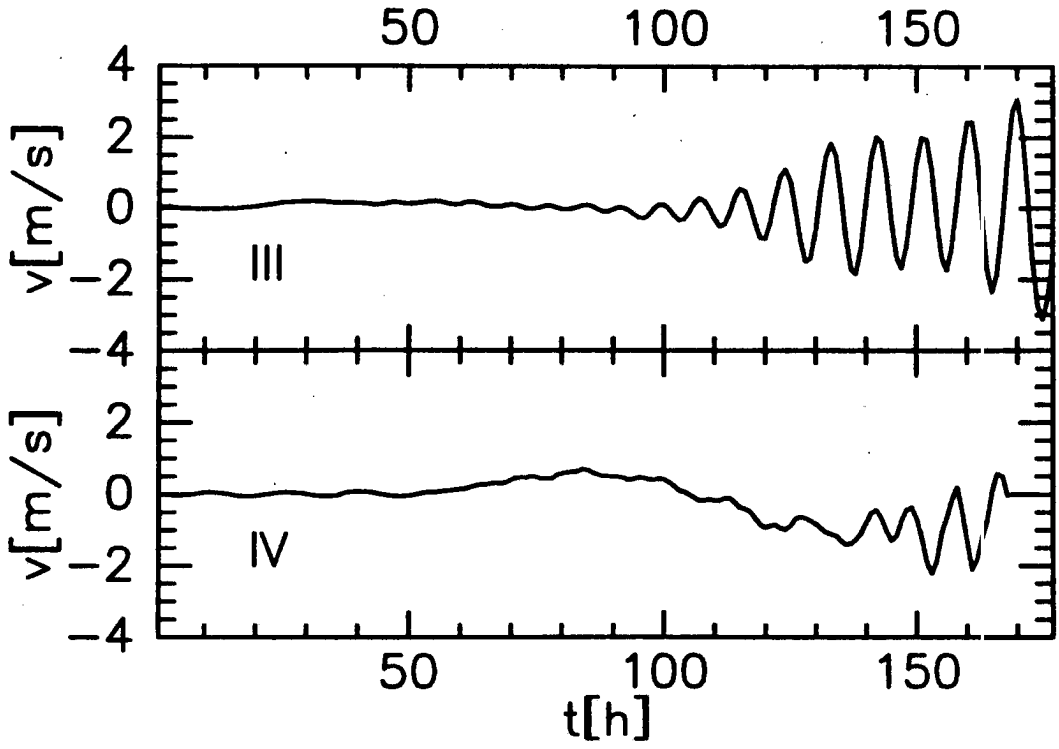

Figure 6.11: Meridional vortex velocity for experiment III and IV

asymmetric flow near the the vortex center. In this case, even though the frequency of the forcing does not match the barotropic instability frequency ($\omega = 10\omega_{Bar}$), we obtain the strong response at the period T_{Bar} (Fig. 6.10) and the vortex makes a large anticyclonic loop with $T = T_{Bar}$. The anticyclonic loop is followed by cyclonic loops (Fig. 6.12). The upper-layer asymmetric flow (Fig. 6.13) confirms our conclusion that barotropic instability caused the anticyclonic loop in experiment IV. For the weak vortex, the flow in the upper layer is very similar to the initial environmental flow. In the strong vortex in a steady environment we can see the amplification of the asymmetric flow near the vortex center - the structure similar to that observed in barotropically unstable modes in the shallow water model. The upper layer flow is stronger than the initial flow and concentrated near the vortex center. The asymmetric wind in Exp. IV has a similar structure but is much stronger than that in Exp. II. The anticyclonic loops with period of a few days can be observed in real cyclones. Fig 6.14 shows the examples of the looping track of four Atlantic cyclones. In all these cases, the storms were intense and the looping motion had amplitude of about 150 km and period of a few days. This suggests that the looping motion in these

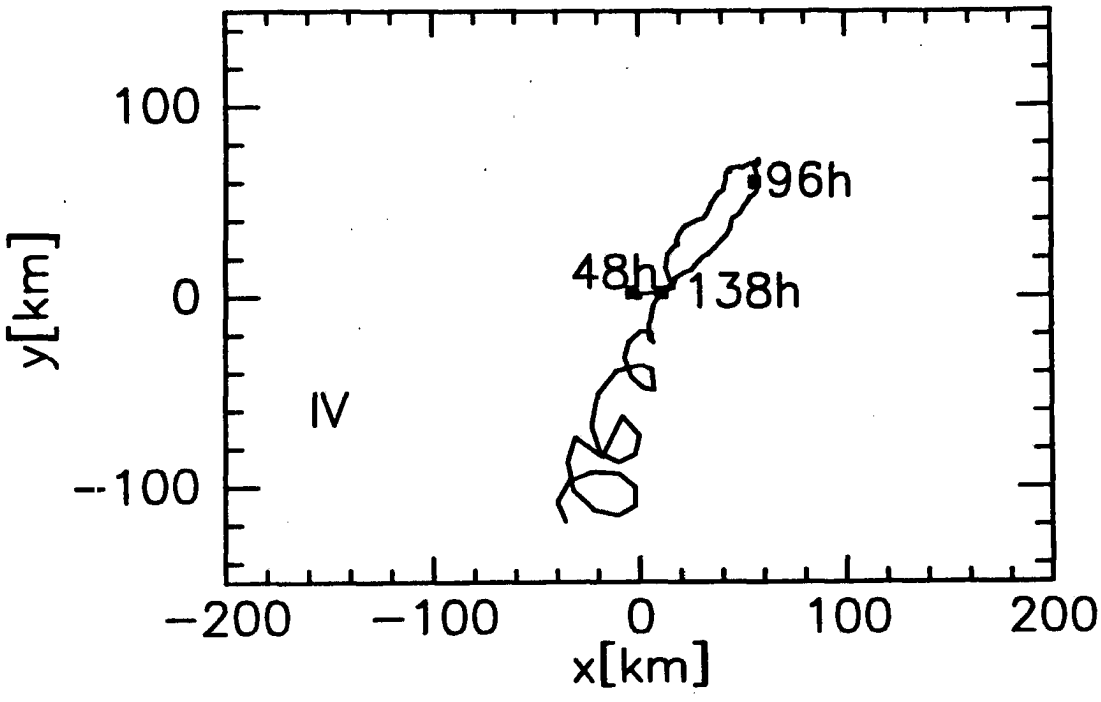

Figure 6.12: Vortex track in experiment IV

storms could result from interaction of barotropically unstable internal flow and varying in time environmental flow (Xu and Gray (1982) note that typical synoptic situation for the looping motion of the tropical storm involves deepening midlatitude trough or rapidly moving short wave trough). It is however difficult to determine if their looping tracks were caused by resonant interaction between the cyclone flow and environment or just by advection by changing environmental flow.

We now compare the effect of the identical environmental forcing on the two different vortices - strong vortex A and weak vortex B. As in experiment IV, we put the vortices in stagnant initial flow and introduce the forcing with Gaussian distribution centered at 500 km radius. To make the forcing term independent of the calculated flow, we use the constant amplitude U_c/T_C, instead of nudging form $(U - U_c)/T_c$. As in experiment IV, U_c=-1m/s, but we use a larger time scale of T_c=24 hours. In this experiment the frequency of forcing $\omega = 1.2 \cdot 10^{-5} s^{-1}$ which is close to the frequency of barotropically unstable mode.

As can be seen from Fig. 6.15, the response of both vortices to the identical forcing is quite different. In the case of the strong vortex, most energy (about 20 %) is concentrated

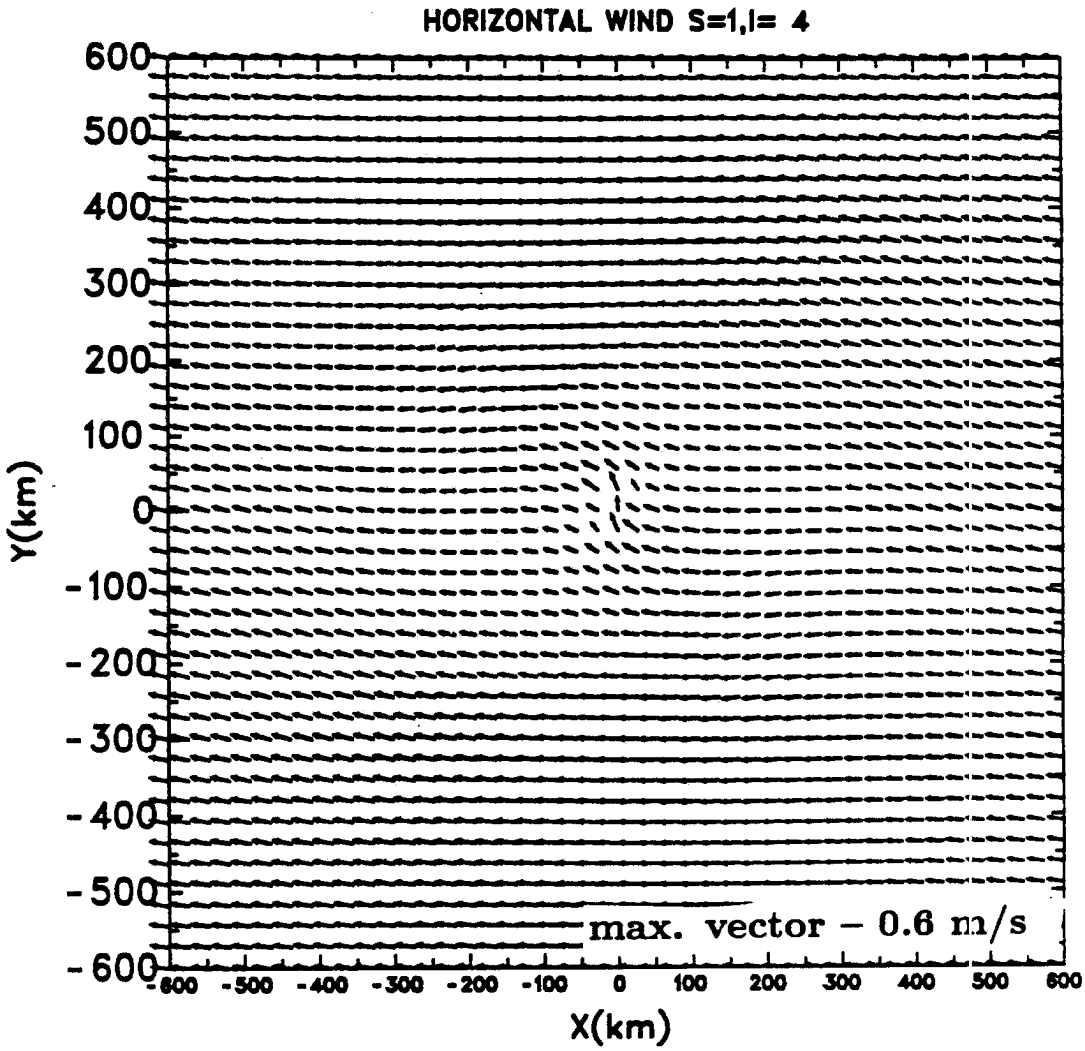

Figure 6.13: a)Upper level asymmetric flow in experiment I after four days of simulation

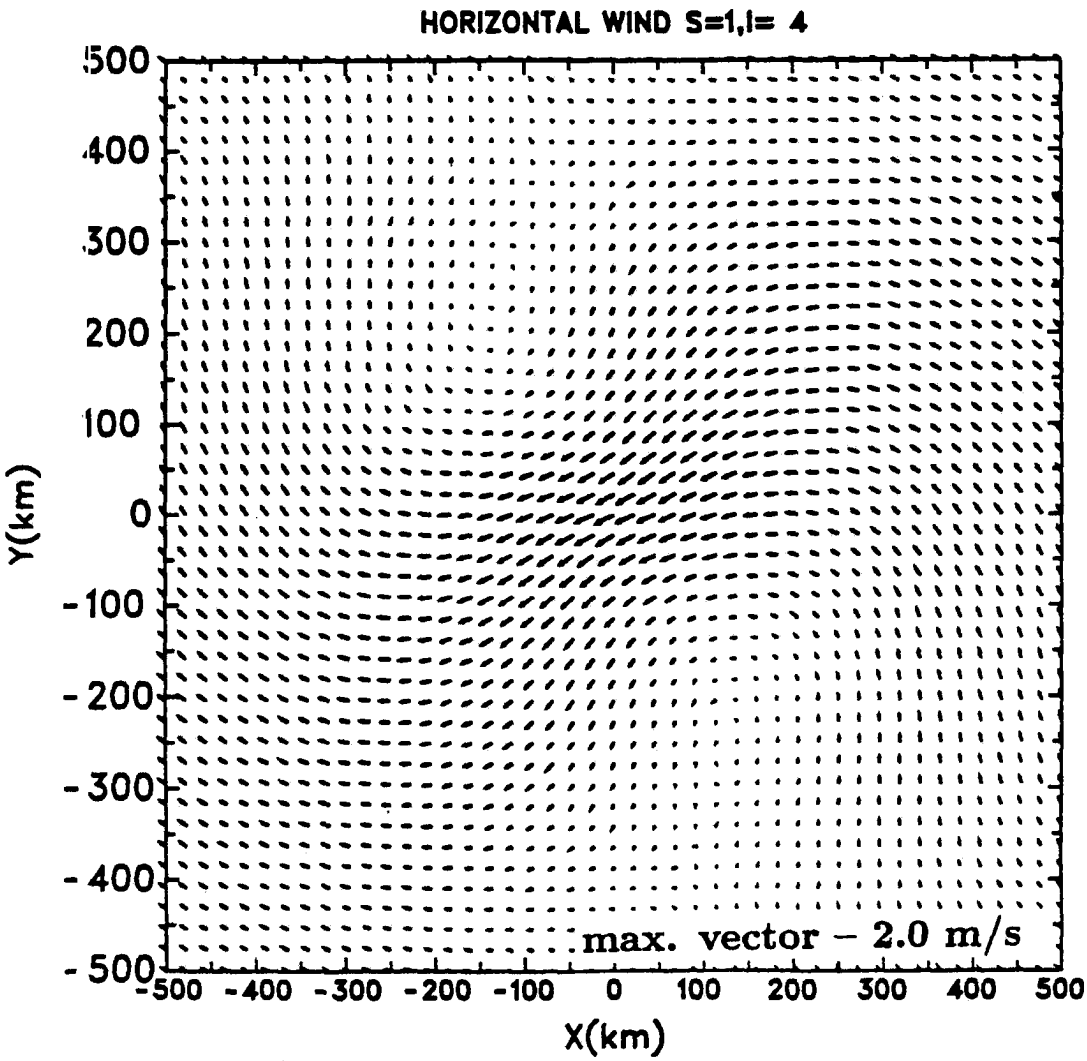

Figure 6.13: b)Upper level asymmetric flow in experiment II after four days of simulation

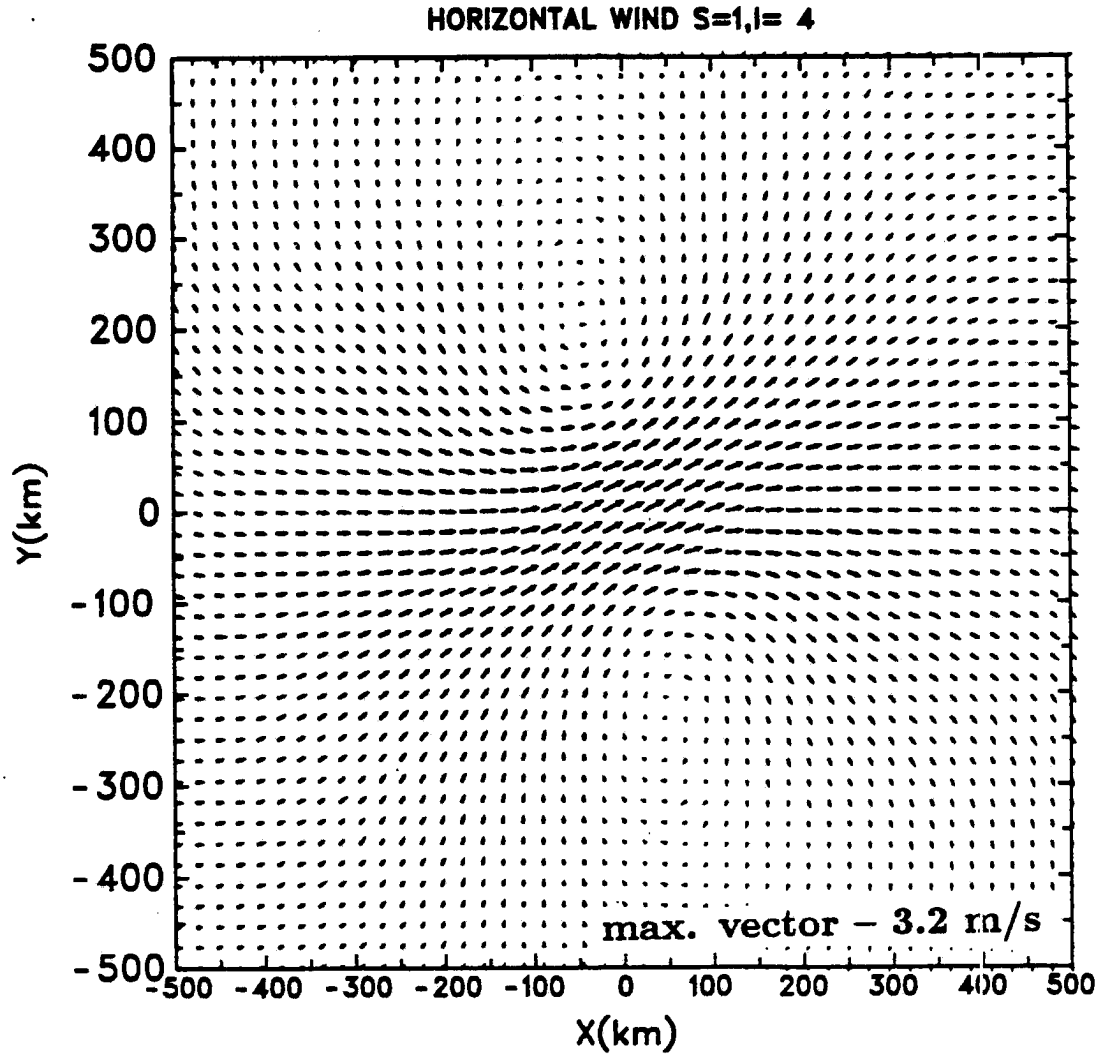

Figure 6.13: c)Upper level asymmetric flow in experiment IV after four days of simulation

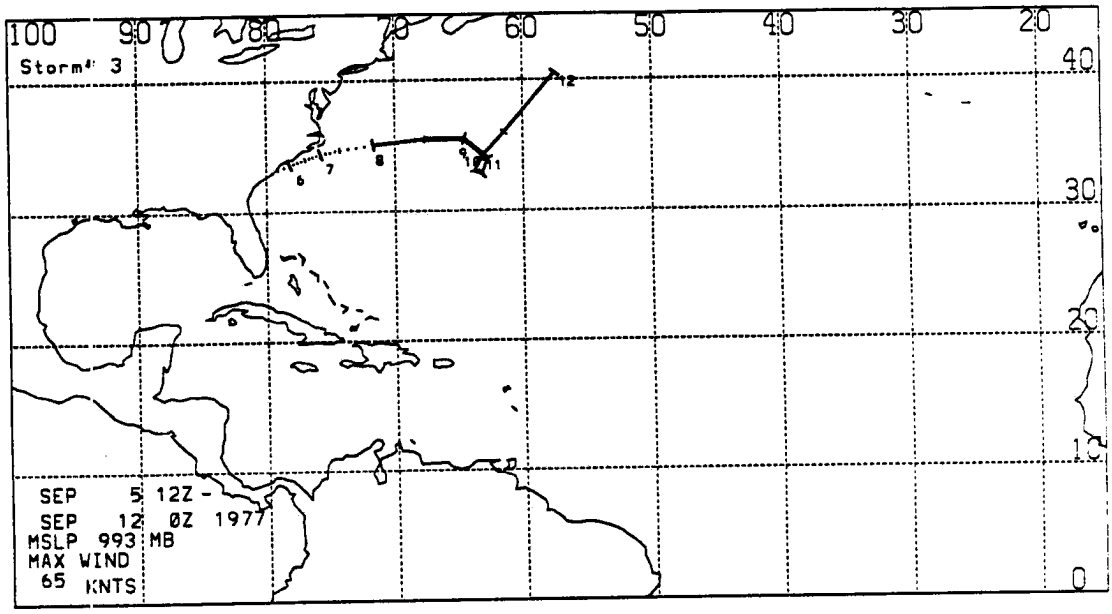

TYPHOON STORM # 3 YEAR 1977

Date	P(mb)	V	Dir	Spd
SEP 5 12	1015	20	60	8
SEP 6 0	1013	20	65	6
SEP 6 12	1011	25	70	5
SEP 7 0	1010	30	70	6
SEP 7 12	1010	30	80	8
SEP 8 0	1006	35	80	13
SEP 8 12	993	65	85	14
SEP 9 0	998	65	110	11
SEP 9 12	999	55	155	7
SEP 10 0	1000	45	230	4
SEP 10 12	1001	45	355	3
SEP 11 0	1002	45	40	8
SEP 11 12	1001	45	35	19
SEP 12 0	1001	45	35	27

Figure 6.14: The examples of anticyclonically looping tropical cyclones a) hurricane Clara

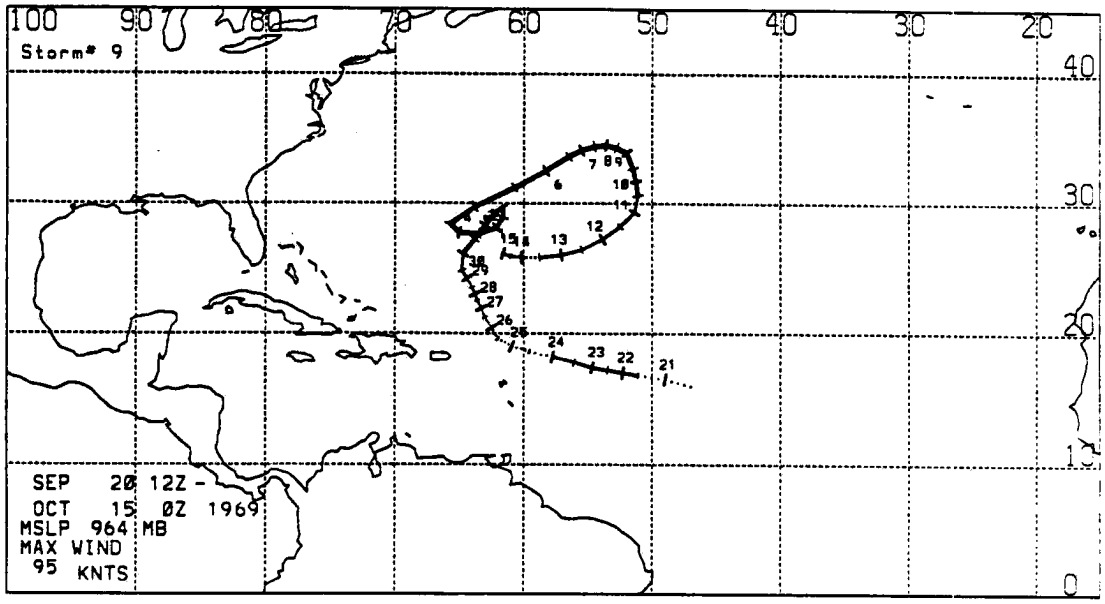

TYPHOON STORM # 9 YEAR 1969

Date	P(mb)	V	Dir	Spd
SEP 20 12	9999	25	285	9
SEP 21 0	9999	30	280	10
SEP 21 12	1001	40	280	7
SEP 22 0	9999	45	280	5
SEP 22 12	1007	50	280	5
SEP 23 0	9999	55	285	6
SEP 23 12	1006	35	285	7
SEP 24 0	9999	30	285	8
SEP 24 12	1007	25	285	7
SEP 25 0	9999	30	295	6
SEP 25 12	9999	30	310	5
SEP 26 0	9999	25	330	4
SEP 26 12	9999	25	335	4
SEP 27 0	9999	25	335	3
SEP 27 12	9999	25	345	3
SEP 28 0	9999	25	335	2
SEP 28 12	1000	30	335	3
SEP 29 0	9999	35	330	3
SEP 29 12	992	50	340	4
SEP 30 0	9999	65	30	7

Date	P(mb)	V	Dir	Spd
SEP 30 12	990	75	35	6
OCT 1 0	9999	80	35	6
OCT 1 12	990	80	40	5
OCT 2 0	9999	80	145	2
OCT 2 12	987	80	200	4
OCT 3 0	9999	70	230	5
OCT 3 12	989	70	260	6
OCT 4 0	9999	70	285	5
OCT 4 12	980	75	15	6
OCT 5 0	9999	90	60	13
OCT 5 12	964	95	60	13
OCT 6 0	9999	95	60	10
OCT 6 12	980	80	55	6
OCT 7 0	9999	80	65	4
OCT 7 12	981	85	75	4
OCT 8 0	9999	85	100	3
OCT 8 12	988	65	115	3
OCT 9 0	9999	75	145	4
OCT 9 12	985	75	165	5
OCT 10 0	9999	70	170	4

Date	P(mb)	V	Dir	Spd
OCT 10 12	993	60	170	5
OCT 11 0	9999	60	210	7
OCT 11 12	998	50	225	7
OCT 12 0	9999	40	240	8
OCT 12 12	1001	35	250	7
OCT 13 0	9999	35	260	7
OCT 13 12	1003	30	265	7
OCT 14 0	9999	30	270	4
OCT 14 12	1008	25	290	2
OCT 15 0	9999	25	290	2

Figure 6.14: continued; b) hurricane Inga

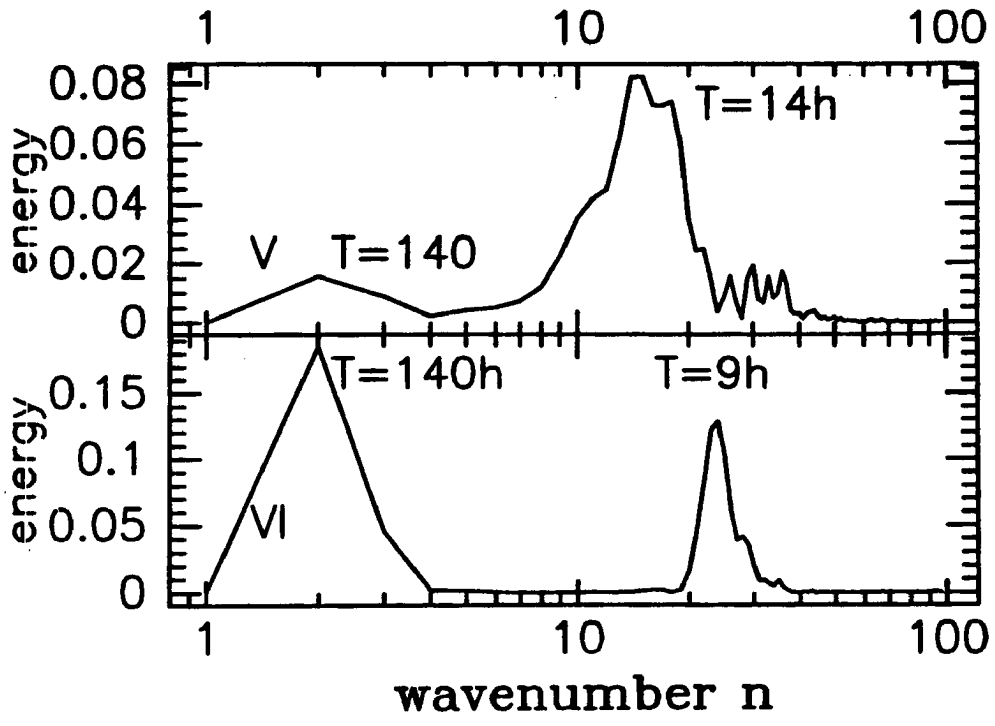

Figure 6.15: Power spectrum for experiment V (vortex B —weak) and VI (vortex A — strong). The energy is normalized to the total kinetic energy of the vortex motion. The wavenumbers are plotted on logarithmic scale. The frequency of the mode wavenumber n is equal to $\omega_n = 2\pi n/L$ where L=8 days.

in the modes with the smallest frequency corresponding to the frequency of the forcing. For the weaker vortex, the modes with periods of about 14 hours contain the most energy. Only 2% of the energy is contained in the low-frequency modes. Therefore, there is no indication of barotropic instability (since reversal of potential vorticity gradient is only a necessary, but not sufficient, condition for barotropic instability, this is a reasonable result) The difference of the response can be seen also in vortex velocity. In both cases, the zonal velocity corresponds to forcing, but the response is stronger and appears earlier for the strong vortex. The meridional velocity of the weak vortex stays close to zero until about 140 hours of integration (when cyclonic loops appear), while meridional velocity for the strong vortex changes in response to forcing (Fig. 6.16). The tracks of the two vortices are also quite different (Fig. 6.17). The stronger vortex makes at first the slow loop, while the weak vortex stays motionless. After about five days both vortices experience the cyclonic looping motion, although the loops are larger for the weaker vortex.

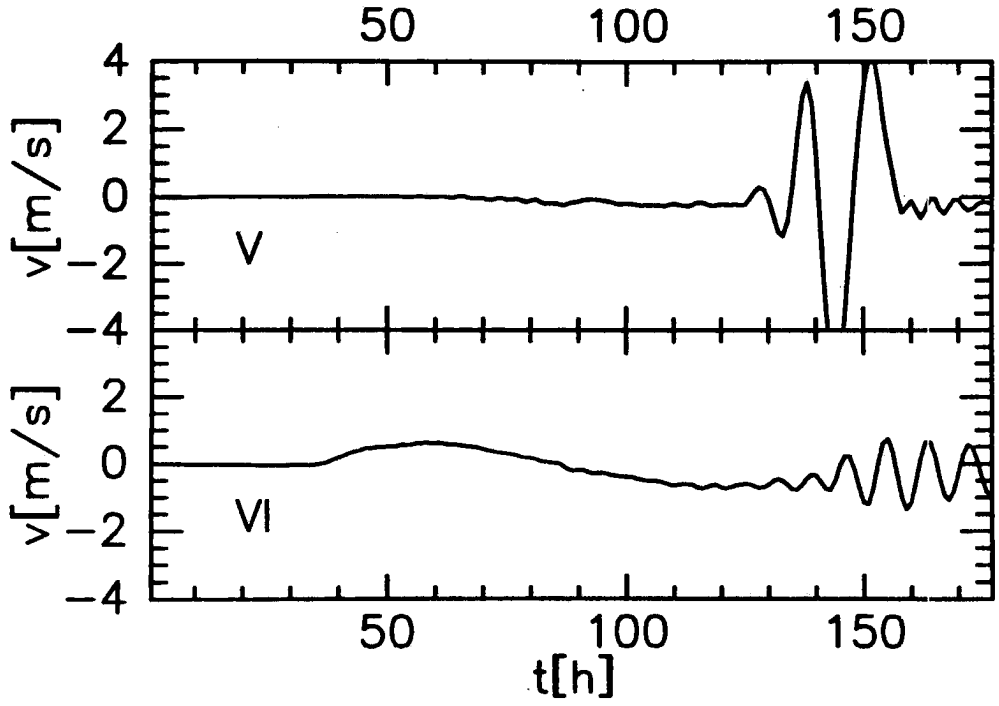

Figure 6.16: Meridional vortex velocity for experiment V (vortex B — weak) and VI (vortex A — strong)

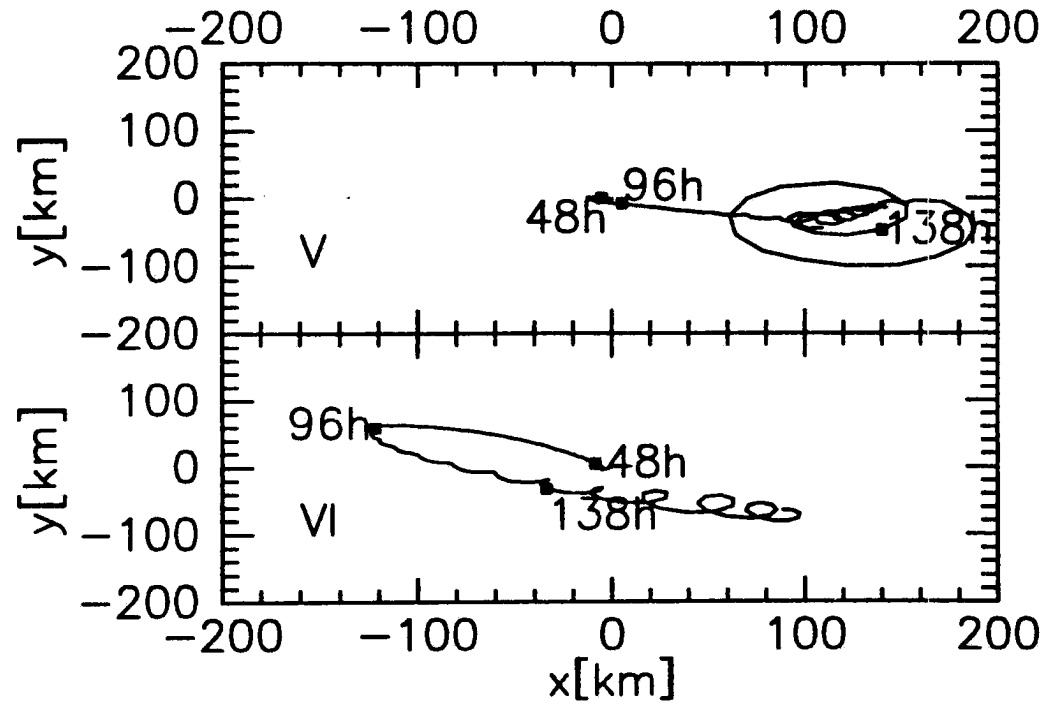

Figure 6.17: Vortex track in experiment V (vortex B — weak and VI(vortex A — strong).

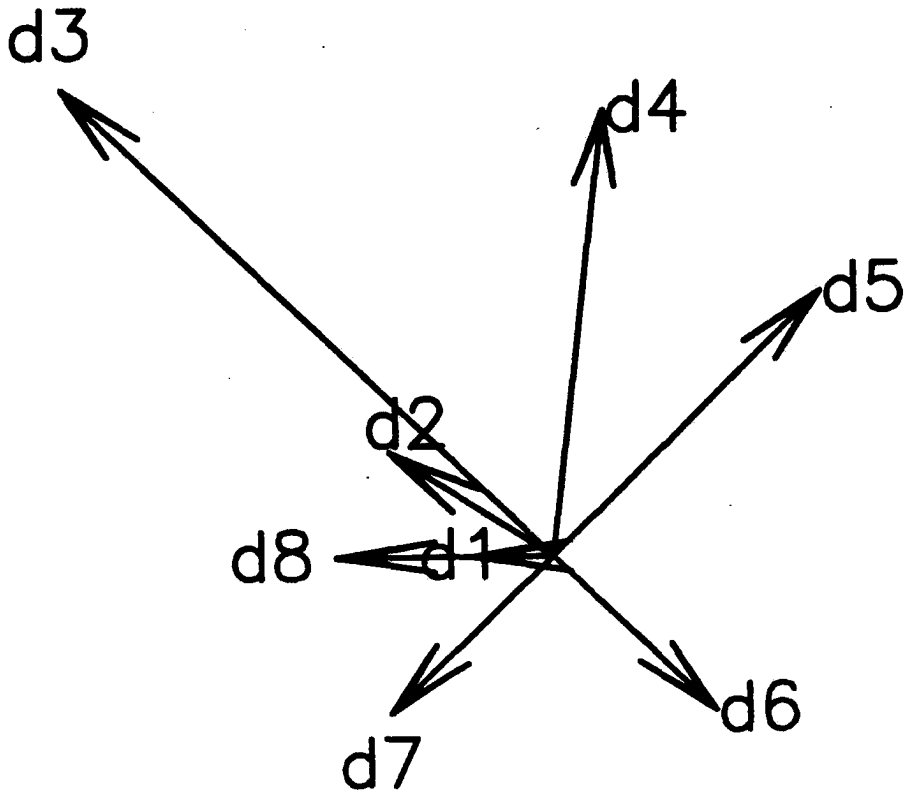

Figure 6.18: Upper-level asymmetric flow, near the vortex center in exp VI. The length of arrows is proportional to the asymmetric wind velocity at the vortex center. The symbol d1 denotes the first 24 hour of calculations, d2 the second day etc.

It is worth noting that the slow loop in the track of vortex A is cyclonic, even though the low frequency of this motion and the fact that it appears only for the stronger vortex suggests that it is connected to barotropic instability of the upper layer flow (the asymmetric flow in the upper layer turns anticyclonically as could be expected for barotropic instability (Fig.6.18)). Therefore it is difficult to find the simple criterion allowing us to look for the effect of barotropic instability in hurricane data.

6.4 Summary

We examined here the dynamic instabilities in a three-dimensional baroclinic vortex. We have shown that development of symmetric inertial instability depends on vertical resolution of a model. In the five-level model, the unstable symmetric modes did not develop even though we could observe an area of negative potential vorticity.

When we looked at the motion of vortex in the five-level model, we could see two types of looping motion. The first type of periodic motion, with periods of about 8-10

hours, developed in both weak and strong vortices. This type of motion can be associated with the mechanism decribed by Yeh (1950).

In the strong vortex, we could also observe looping motion with the large periods corresponding to the barotropically unstable mode. This type of motion depended strongly on the horizontal distribution of environmental forcing. The forcing concentrated at 500 km radii excited this mode, while the horizontally uniform forcing did not. This may be due to the fact that, according to Yeh (1950), the amplitude of cyclonic oscillations depends on relative wind speed between the vortex and environment. When the forcing reaches the vortex center, the speed of a cyclone relative to the environment is large, compared to the case with forcing limited to the large radii. Since tropical cyclones usually move with the speed roughly equal to the environmental wind speed, we can speculate that cyclonic looping should follow the changes in the steering current. Some numerical models (e.g., Jones, 1987) show the development of the cyclonic loops during hurricane landfall.

The dependence on forcing frequency was not as strong. The slow modes appeared when the model was forced with frequency $\omega = \omega_{Bar}$ and $\omega = 10\omega_{Bar}$. The percentage of energy contained in the slow modes was slightly larger(20 % vs. 15 %) for $\omega = \omega_{Bar}$.

The low-frequency looping could not be observed in the weak vortex, even though the reversal of potential vorticity gradient could be observed for this vortex at about 200 km from the center. However, the reversal of potential vorticity gradient is only the necessary, but not sufficient condition for instability.

Comparison of the results for the weak and strong vortex shows the difference in the response for identical forcing. Therefore, in predicting vortex motion, the knowledge of the vortex characteristics, and not only the environmental flow, is important.

Chapter 7

SUMMARY AND CONCLUSIONS

The numerical study presented here has focused on baroclinic processes which contribute to vortex propagation. A numerical model of a moving baroclinic vortex was developed to examine these processes. The model is written in cylindrical coordinates and uses a spectral representation in the azimuthal direction. A spectral representation allowes us to reduce the computational effort needed for resolving the three dimensional structure of a cyclone by limiting the number of tangential modes. Using only a few tangential modes in the investigation of tropical cyclone motion is justified by the fact that tropical cyclones usually exhibit a structure dominated by low tangential wavenumbers. Also, the environmental features most important for evaluation of the vortex motion can be described with only a few tangential modes.

In this study we have investigated how vortex motion is affected by (1) the interaction between upper and lower potential vorticity anomalies in a tilted vortex, (2) asymmetric distribution of diabatic heating, and (3) the presence of dynamic instabilities in the cyclone outflow layer. The main results are summarized as follows:

1. It is a well known fact that vortices in barotropic models interact with each other. This interaction leads to propagation of the vortices relative to the environmental flow. We extend this idea to a tilted baroclinic vortex. In such a vortex the vertical transport of momentum causes asymmetry of the vortex circulation and subsequent propagation. We consider vortex tilting caused by the β-effect and vertically sheared environmental flow. Since advection of planetary vorticity causes anticyclones to move toward the southwest while cyclones move toward the northwest, a baroclinic vortex on a β-plane is tilted slightly toward the south. In the absence of diabatic

heating the vortices move nearly independently of each other since there is no vertical transport of momentum by secondary circulation. When diabatic heating is included the interaction between the upper and lower layers reduces the westward speed of a vortex. Increasing the vertical exchange between layers by introducing momentum diffusion further reduces the westward velocity. Track changes caused by these effects are not very large. It is interesting, however, that while in a barotropic model introducing an anticyclonic circulation at the vortex periphery reduces the poleward velocity of the vortex, an anticyclonic circulation added on the top of a cyclone leads to a decrease in the westward velocity. This suggests that intuition gained from barotropic models cannot always be easily extended to baroclinic situations.

We have also investigated the motion of a vortex on a f-plane, in a vertically sheared, environmental flow. Tilting of the vortex in this case causes a propagation relative to the steering flow comparable with the propagation caused by the β effect. The direction of propagation depends on the direction of the wind shear. In the absence of background potential vorticity gradients, vortices turn toward the north in westerly shear and toward the south in easterly shear. The speed of propagation increases with increasing vortex intensity and vertical motion.

Since the direction of motion depends on the relative position of potential vorticity anomalies, the presence of a background potential vorticity gradient changes the direction of motion caused by the interaction between the layers. As shown by Shapiro (1991), even if the environmental absolute vorticity is constant, the potential vorticity gradient can be influenced by vertical stability changes, resulting from the meridional temperature gradient associated with vertical wind shear. For some wind profiles advection of environmental potential vorticity opposes the effect of interaction between vortex layers and can even cause the vortex in a westerly shear to move toward the south.

2. Diabatic heating asymmetries at small radii (i.e., asymetries in the eye-wall convetion) do not have a major impact on vortex motion. This is due to a stabilizing

influence of the large radial shear in the mean tangential flow. Asymmetries at large radii (e.g., 500 km) create potential vorticity anomalies similar to the " beta gyres". The circulation induced by these anomalies advects the vortex. When the heating maximum is placed in the south, or southeastern quadrant of the vortex (which is justified by the presence of moist equatorial air, and can be seen in composite data) the vertical redistribution of potential vorticity caused by diabatic heating, reduces the potential vorticity anomalies caused by advection of planetary vorticity and substantially changes the β induced propagation.

3. The results of a shallow water, linear model show that dynamically unstable modes can develop in the cyclone outflow layer even in the absence of environmental forcing. Development of both barotropic and inertial instability is possible. The symmetric, inertially unstable modes have the largest growth rates. The small vertical scale at which these modes occur suggests that in the real atmosphere they can be stabilized by turbulence. For intermediate vertical scales, asymmetric ($s = 1$), inertially unstable perturbations are also possible. For larger vertical scales only barotropically unstable perturbations develop. We have to note however that unlike in the case of parallel flow, the fastest growth occurs for finite equivalent depth. Barotropically unstable modes can be resolved in a numerical model with a relatively crude vertical resolution. Since the modes with the greatest growth rates have $s = 1$ azimuthal structure, we hypothesize that development of barotropic instability can influence the vortex motion. Therefore, we examine the development of barotropically unstable modes and their influence on vortex motion using our baroclinic vortex model. The spectral analysis of a vortex velocity time series, shows that for intense vortices slow (with periods of about four days) looping motion can be observed. Since the period of this slow oscillation corresponds to the frequency of barotropically unstable modes, we attribute this type of motion to the development of barotropic intstability in the outflow layer of the baroclinic vortex. It is worth noting however that not all types of environmental forcing trigger this response.

Bibliography

Abe, S., 1987: The looping motion and the asymmetry of tropical cyclone. *J. Meteor. Soc. Japan*, **65**, 247–257.

Adem, J., 1956: A series solution for the barotropic vorticity equation and its application in the study of atmospheric vortices. *Tellus*, **8**, 364–372.

Alaka, M. A., 1962: The occurrence of dynamic instability in incipient and developing hurricanes. *Mon. Wea. Rev.*, **90**, 49–68.

Anthes, R. A., 1972: Development of asymmetries in a three-dimensional numerical model of the tropical cyclone. *Mon. Wea. Rev.*, **100**, 461–476.

Black, P. G. and R. A. Anthes, 1971: On the asymmetric structure of the tropical cyclone outflow layer. *J. Atmos. Sci.*, **28**, 1348–1366.

Carr, L. E. and R. L. Elsberry, 1990: Observational evidence of tropical cyclone propagation relative to environmental steering. *J. Atmos. Sci.*, **47**, 542–546.

Carr, L. E. and R. T. Williams, 1989: Barotropic vortex stability to perturbations from axisymmetry. *J. Atmos. Sci.*, **46**, 3177–3191.

Chan, J. C. and W. M. Gray, 1982: Tropical cyclone movement and surrounding flow relationships. *Mon. Wea. Rev.*, **11**, 1354–1374.

Chan, J. C. L., 1985: Identification of the steering flow for tropical cyclone motion from objectively analyzed fields. *Mon. Wea. Rev.*, **113**, 106–116.

Chang, S. W. and R. V. Madala, 1980: Numerical simulation of the influence of sea surface temperature on translating tropical cyclones. *J. Atmos. Sci.*, **37**, 2617–2630.

Chen, L. and W. M. Gray, 1985: *Global view of the upper level outflow patterns associated with tropical cyclone intensity change during FGGE.* Atmospheric Science Paper 392, Colorado State University, Fort Collins, Colo.

DeMaria, M., 1983: *Experiments with a spectral tropical cyclone model.* Atmospheric Science Paper 371, Colorado State University, Fort Collins, Colo.

DeMaria, M., 1987: Tropical cyclone motion in a nondivergent barotropic model. *Mon. Wea. Rev.*, **115**, 2346–2357.

Dong, K. and C. J. Neumann, 1986: The relationship between tropical cyclone motion and environmental geostrophic flows. *Mon. Wea. Rev.*, **114**, 115–122.

Emanuel, K. A., 1989: The finite-amplitude nature of tropical cyclogenesis. *J. Atmos. Sci.*, **46**, 3431–3456.

Evans, J. L., G. J. Holland, and R. L. Elsberry, 1991: Interactions between a barotropic vortex and an idealized subtropical ridge. Part i: Vortex motion. *J. Atmos. Sci.*, **48**, 301–314.

Fett, R. W. and S. Brand, 1975: Tropical cyclone movement forcasts based on observations from satellites. *J. Appl. Met.*, **14**, 452–465.

Fiorino, M. and R. L. Elsberry, 1989: Some aspects of vortex structure related to tropical cyclone motion. *J. Atmos. Sci.*, **46**, 975–990.

Fiorino, M. and R. L. Elsberry, 1989: Contributions to tropical cyclone motion by small, medium and large scales in the initial vortex. *Mon. Wea. Rev.*, **117**, 721–727.

Franklin, J. L., 1990: Dropwindsonde observations of the environmental flow of hurricane Josephine (1984): Relationships to vortex motion. *Mon. Wea. Rev.*, **118**, 2732–2744.

Gent, P. R. and J. C. McWilliams, 1986: The instability of barotropic circular vorticies. *Geophys. and Astrophys. Fluid Dynamics*, **35**, 209–233.

Ginis, I. and A. Khain, 1991: The mutual response of a moving tropical cyclone and the ocean. In *19th Conference on Hurricanes and Tropical Meteorology*, American Meteorological Society, Miami.

Gray, W. M., 1989: Summary of W. M. Gray ONR sponsored tropical motion research. (ONR report).

Gray, W. M., 1991: Tropical cyclone propagation. In *19th Conference on Hurricanes and Tropical Meteorology*, American Meteorological Society, Miami.

Hack, J. J. and W. H. Schubert, 1980: *The role of convective-scale processes in tropical cyclone development.* Atmospheric Science Paper 330, Colorado State University, Fort Collins, Colo.

Hack, J. J. and W. H. Schubert, 1981: Lateral boundary conditions for tropical cyclone models. *Mon. Wea. Rev.*, **109**, 1404–1419.

Hack, J. J. and W. H. Schubert, 1986: Nonlinear response of atmospheric vortices to heating by organized cumulus convection. *J. Atmos. Sci.*, **43**, 1559–1573.

Hallin, S. C., 1991: *Diurnal variations in tropical cyclones.* Master's thesis, Colorado State University.

Hodanish, S. J., 1991: *An observational analysis of tropical cyclone recurvature.* Atmospheric Science Paper 480, Colorado State University, Fort Collins, Colo.

Holland, G. J., 1983: Tropical cyclone motion: Environmental interaction plus a beta effect. *J. Atmos. Sci.*, **40**, 328–342.

Holland, G. J., 1984: Tropical cyclone motion: A comparison of theory and observation. *J. Atmos. Sci.*, **41**, 68–75.

Holland, G. J., 1988: General recurvature forecast problems. ONR tropical cyclone motion research initiative.

Holland, G. J., 1991: On the meandering nature of tropical cyclone tracks. In *19th Conference on Hurricanes and Tropical Meteorology*, American Meteorological Society, Miami.

Huntley, J. E. and J. W. Diercks, 1981: The occurrence of vertical tilt in tropical cyclones. *Mon. Wea. Rev.*, **109**, 1689–1700.

Jones, R. W., 1977: Vortex motion in a tropical cyclone model. *J. Atmos. Sci.*, **34**, 1528–1553.

Jones, W. R., 1987: A simulation of hurricane landfall with a numerical model featuring latent heating by resolvable scales. *Mon. Wea. Rev.*, **115**, 2279–2297.

Jordan, C. L., 1966: Surface pressure variations at coastal stations during the period of irregular motion of hurricane Carla of 1961. *Mon. Wea. Rev.*, **94**, 454–458.

Kitade, T., 1980: Numerical experiments of tropical cyclones on a plane with variable Coriolis parameter. *J. Meteor. Soc. Japan*, **58**, 471–488.

Kuo, H. L., 1969: Motions of vortices and circulating cylinder in shear flow with friction. *J. Atmos. Sci.*, **26**, 390–398.

Kurihara, Y. and M. A. Bender, 1980: Use of movable nested mesh model for tracking a small vortex. *Mon. Wea. Rev.*, **108**, 1792–1809.

Kurihara, Y., M. A. Bender, R. E. Tuleya, and R. J. Ross, 1990: Prediction experiments of hurricane Gloria (1985) using a multiply nested movable mesh model. *Mon. Wea. Rev.*, **118**, 2185–2198.

Lajoie, F. A., 1976: On the direction of movement of tropical cyclones. *Austr. Meteor. Mag.*, **24**, 95–104.

Lajoie, F. A., 1986: Effects of the upper flow asymmetry on the future direction of motion of tropical cyclones. *Mon. Wea. Rev.*, **114**, 1863–1875.

Lindzen, R. S. and K. K. Tung, 1978: Wave overreflection and shear instability. *J. Atmos. Sci.*, **35**, 1626–1632.

Madala, R. V. and S. A. Piacsek, 1975: Numerical simulation of asymmetric hurricanes on a β-plane with vertical shear. *Tellus*, **27**, 453–467.

Matsuno, T., 1966: Numerical integrations of the primitive equations by a simulated backward difference model. *J. Meteor. Soc. Japan*, **44**, 76–84.

Merill, R. T., 1985: *Environmental influences on hurricane intensification.* Atmospheric Science Paper 394, Colorado State University, Fort Collins, Colo.

Merill, R. T., 1988: Characteristics of the upper-tropospheric environmental flow around hurricanes. *J. Atmos. Sci.*, **45**, 1665–1667.

Muramatsu, T., 1986: Trochoidal motion of the eye of typhoon 8019. *J. Meteor. Soc. Japan*, **64**, 259–272.

Ooyama, K. V., 1969: Numerical simulation of the life cycle of tropical cyclones. *J. Atmos. Sci.*, **26**, 3–40.

Ooyama, K. V., 1987: Numerical experiments of steady and transient jets with a simple model of the hurricane outflow layer. In *17th Conference on Tropical Meteorology*, American Meteorological Society, Miami, Fl.

Peng, M. S. and R. T. Williams, 1990: Dynamics of vortex asymmetries and their influence on a vortex motion on a β plane. *J. Atmos. Sci.*, **47**, 1987–2003.

Ripa, P., 1983: General stability conditions for zonal flows in a one-layer model on the βplane or the sphere. *J. Fluid. Mech.*, **126**, 463–489.

Rotunno, R. and K. A. Emanuel, 1987: An air-sea interaction theory for tropical cyclones. Part II: Evolutionary study using a nonhydrostatic axisymmetric numerical model. *J. Atmos. Sci.*, **44**, 542–561.

Sawyer, J. S., 1947: Notes on the theory of tropical cyclones. *Quart. J. Roy. Met. Soc.*, **73**, 101–126.

Schubert, W. H. and B. T. Alworth, 1987: Evolution of potential vorticity in tropical cyclones. *Quart. J. Roy. Met. Soc.*, **113**, 147–162.

Schubert, W. H., P. E. Ciesielski, D. E. Stevens, and H. Kuo, 1991: Potential vorticity modeling of the ITSZ and the Hadley circulation. *J. Atmos. Sci.*, **48**, 1493–1509.

Schubert, W. H. and J. J. Hack, 1983: Transformed balanced vortex model. *J. Atmos. Sci.*, **30**, 1571–1583.

Shapiro, L. J., 1991: Hurricane vortex motion and evolution in a three-layer model. *J. Atmos. Sci.*, **48**, *in press.*

Shapiro, L. J. and K. V. Ooyama, 1990: Barotropic vortex evolution on a beta plane. *J. Atmos. Sci.*, **47**, 170–187.

Shoemaker, D. N., 1989: *Relationships between tropical cyclone deep convection and the radial extent of damaging winds.* Atmospheric Science Paper 457, Colorado State University, Fort Collins, Colo.

Smith, R., 1991: An analytic theory of tropical cyclone motion in a barotropic shear flow. *Quart. J. Roy. Met. Soc.*, **117**, *submitted for publication.*

Smith, R. K., W. Ulrich, and G. Dietachmayer, 1990: A numerical study of tropical cyclones using a barotropic model. Part I: The role of vortex asymmetries. *Quart. J. Roy. Met. Soc.*, **116**, 337–362.

Stevens, D. E., 1983: On symmetric stability and instability of zonal mean flows near the equator. *J. Atmos. Sci.*, **40**, 882–893.

Stevens, D. E. and P. Ciesielski, 1986: Inertial instability of horizontally sheared flow away from the equator. *J. Atmos. Sci.*, **43**, 2845–2856.

Tuleya, R. E. and Y. Kurihara, 1981: A numerical study on the effects of environmental flow on tropical storm genesis. *Mon. Wea. Rev.*, **109**, 2487–2505.

Ulrich, W. and R. K. Smith, 1991: A numerical study of tropical cyclone motion using a barotropic model. II:Motion in spatially-varying large-scale flows. *Quart. J. Roy. Met. Soc.*, **117**, 107–124.

Wang, B. and X. Li, 1991: A numerical study of the beta-drift of three dimensional vortices. In *19th Conference on Hurricanes and Tropical Meteorology*, American Meteorological Society, Miami.

Willoughby, H. E., 1988: Linear motion of a shallow-water, barotropic vortex. *J. Atmos. Sci.*, **45**, 1906–1928.

Willoughby, H. E., H. Jin, S. J. Lord, and J. M. Piotrowicz, 1984: Hurricane structure and evolution as simulated by an axisymmetric, nonhydrostatic numerical model. *J. Atmos. Sci.*, **41**, 1169–1186.

Wu, C. C. and K. A. Emanuel, 1991: Interaction of a baroclinic vortex with a background shear: Application to hurricane movement. In *19th Conference on Hurricanes and Tropical Meteorology*, American Meteorological Society, Miami.

Xu, J. and W. M. Gray, 1982: *Environmental circulations associated with tropical cyclones experiencing fast, slow and looping motion.* Atmospheric Science Paper 346, Colorado State University, Fort Collins, Colo.

Yanai, M., S. Esbensen, and J. Chu, 1973: Determination of bulk properties of tropical cloud clusters from large-scale heat and moisture budgets. *J. Atmos. Sci.*, **30**, 611–627.

Yeh, T. C., 1950: The motion of tropical storms under the influence of a superimposed southerly current. *J. Meteor.*, **7**, 108–113.

Appendix A

CALCULATION OF POTENTIAL VORTICITY IN σ COORDINATES

Potential vorticity is qiven by

$$P = (\boldsymbol{\zeta}_a + f\mathbf{k}) \cdot \nabla\theta\frac{1}{\rho}, \tag{A.1}$$

where $\boldsymbol{\zeta}_a$ denotes absolute vorticity. Vorticity in cylindrical coordinates (r, λ, z) can be expressed as

$$\boldsymbol{\zeta}_a = \mathbf{k}\left[\frac{1}{r}\left(\frac{\partial(rv)}{\partial r} - \frac{\partial u}{\partial\lambda}\right) + f\right] + \boldsymbol{\lambda}\left(\frac{\partial u}{\partial z}\right) + \mathbf{r}\left(-\frac{\partial v}{\partial z}\right), \tag{A.2}$$

where derivatives of vertical velocity were omitted because of the hydrostatic assumption. Using (A.2) we express potential vorticity in cylindrical coordinates as

$$P = \frac{1}{\rho}\left[f + \left(\frac{\partial rv}{\partial z} - \frac{\partial u}{\partial\lambda}\right)\right]\frac{\partial\theta}{\partial z} + \frac{1}{r\rho}\frac{\partial u}{\partial z}\frac{\partial\theta}{\partial\lambda} - \frac{1}{\rho}\frac{\partial v}{\partial z}\frac{\partial\theta}{\partial r}. \tag{A.3}$$

Transformation to σ coordinates is given by the following expressions:

$$\left(\frac{\partial x}{\partial r}\right)_z = \left(\frac{\partial x}{\partial r}\right)_\sigma + \frac{\sigma}{RT}\left(\frac{\partial\phi}{\partial r}\right)_\sigma\frac{\partial x}{\partial\sigma}$$

$$\left(\frac{\partial x}{\partial\lambda}\right)_z = \left(\frac{\partial x}{\partial r}\right)_\sigma + \frac{\sigma}{RT}\left(\frac{\partial\phi}{\partial\lambda}\right)_\sigma\frac{\partial x}{\partial\sigma} \tag{A.4}$$

$$\left(\frac{\partial x}{\partial z}\right) = -\frac{\partial x}{\partial\sigma}\frac{\rho g}{p_s}. \tag{A.5}$$

Combining (A.5) and (A.3) we obtain the expression for potental vorticity in σ coordinates (r, λ, σ):

$$P = \left\{\frac{1}{r}\left[\frac{\partial rv}{\partial r} - \frac{\partial u}{\partial\lambda} + \frac{\sigma}{RT}\left(\frac{\partial\phi}{\partial r}\frac{\partial rv}{\partial\sigma} - \frac{\partial\phi}{\partial\lambda}\frac{\partial u}{\partial\sigma}\right)\right] + f\right\}\left(-\frac{\partial\theta}{\partial\sigma}\frac{g}{p_s}\right)$$

$$- \frac{g}{rp_s}\frac{\partial u}{\partial\sigma}\left(\frac{\partial\theta}{\partial\lambda} + \frac{\sigma}{RT}\frac{\partial\phi}{\partial\lambda}\frac{\partial\theta}{\partial\sigma}\right) \tag{A.6}$$

$$+ \frac{g}{p_s}\left(\frac{\partial\theta}{\partial r} + \frac{\sigma}{RT}\frac{\partial\phi}{\partial r}\frac{\partial\theta}{\partial\sigma}\right). \tag{A.7}$$

The potential vorticity fields in this paper are presenterd using the normalized potential vorticity $P_n = P/P_{nn}$, where normalization factor P_{nn} is given by:

$$P_{nn} = -f_0 \frac{\theta(\sigma_T) - \theta(\sigma_B)}{(\sigma_T - \sigma_B)} \frac{g}{p_0}. \tag{A.8}$$